Summer 2007

Computer simulation and human experiment on the Laplacian electrocardiogram (ECG)

Ting Chen
Louisiana Tech University

COMPUTER SIMULATION AND HUMAN EXPERIMENT ON THE LAPLACIAN ELECTROCARDIOGRAM (ECG)

by

Ting Chen, BS

A Dissertation Presented in Partial Fulfillment
of the Requirement for the Degree
Doctor of Philosophy

COLLEGE OF ENGINEERING AND SCIENCE
LOUISIANA TECH UNIVERSITY

August 2007

LOUISIANA TECH UNIVERSITY

THE GRADUATE SCHOOL

05/17/2007
Date

We hereby recommend that the dissertation prepared under our supervision by Ting Chen

entitled Computer simulation and human experiment on the Laplacian electrocardiogram (ECG)

be accepted in partial fulfillment of the requirements for the Degree of PhD in Biomedical Engineering

Supervisor of Dissertation Research

Head of Department

Biomedical Engineering
Department

Recommendation concurred in:

Advisory Committee

Approved:
Director of Graduate Studies

Approved:
Dean of the Graduate School

Dean of the College

GS Form 13
(5/03)

ABSTRACT

The electrocardiogram (ECG) provides useful global temporal assessment of cardiac activity, but has limited spatial capabilities. Laplacian electrocardiogram (LECG) and body surface Laplacian mapping (BSLM), improvements over ECG provides high spatiotemporal distributed information about cardiac electrical activation.

This project was divided into two parts: computer simulation and human experiment. In the computer simulation, a comparison of the performance of the tripolar and bipolar as well as spline LECG and BSLMs for localizing and imaging the cardiac electrical activation has been investigated. A simple planar surface model and a simplified eccentric heart-torso sphere-cylinder homogeneous volume conductor model were developed. Multiple dipoles with different orientations were used to simulate the underlying cardiac electrical activities. The three estimates of LECG and BSLMs were numerically computed from the induced electrical activity in the two models. For the human experiments, we designed and developed LECG tripolar concentric ring electrode (TCE) active sensors based on the finite element algorithm "nine-point method" (NPM). The active sensors were used in an array of six by twelve (72) locations to record bipolar and tripolar LECG from the body surface over the anterolateral chest.

Results show that the TCE produce the most accurate LECG and BSLM estimation among the tripolar, bipolar and spline LECG estimators with the best performance in noise attenuation and spatial resolution. Compared to bipolar LECG, tripolar LECG showed significantly higher spatial selectivity which may be helpful in inferring information about cardiac activations detected on the body surface. The moment of activation (MOA), an indicator of a depolarization wave passing below the active sensors, was used to surmise possible timing information of the cardiac electrical activation below the active sensors recording sites. The MOA on the body surface were used to generate isochronal maps that may some day be used by clinicians to help diagnose arrhythmias and assessing the efficacy of therapies.

Keywords—Laplacian electrocardiogram (LECG); Tripolar and bipolar concentric ring electrode (TCE and BCE); Nine-point method (NPM); Spatial selectivity; Active sensor; Body surface Laplacian mapping (BSLM); Spline LECG; Heart-torso sphere-cylinder model.

APPROVAL FOR SCHOLARLY DISSEMINATION

The author grants to the Prescott Memorial Library of Louisiana Tech University the right to reproduce, by appropriate methods, upon request, any or all portions of this Dissertation. It is understood that "proper request" consists of the agreement, on the part of the requesting party, that said reproduction is for his personal use and that subsequent reproduction will not occur without written approval of the author of this Dissertation. Further, any portions of the Dissertation used in books, papers, and other works must be appropriately referenced to this Dissertation.

Finally, the author of this Dissertation reserves the right to publish freely, in the literature, at any time, any or all portions of this Dissertation.

Author Chen Ting.

Date 06/26/2007.

GS Form 14
(5/03)

TABLE OF CONTENTS

LIST OF TABLES

LIST OF FIGURES

ACKNOWLEDGEMENTS

I would like to thank my advisor Dr. Besio for considering me for this project. He has been a constant source of guidance and support. His motivation towards work has been major contribution towards my professional and personal growth. I would like to extend my thanks to Dr. Weizhong Dai, Dr. Steven Jones, Dr. Lihe Zou and Dr. Alan Chiu for being a part of my advising committee and evaluating my work.

I thank my family, my husband Eric C. Withers for being extremely patient and supportive. To my friends and other lab members who have been a surrogate family, thanks for being there for me.

CHAPTER 1

INTRODUCTION

1.1 Anatomy and Physiology of the Heart

1.1.1 Location of the Heart

The human heart is a muscular organ which provides the force necessary to circulate the blood to the whole body. The heart's size is about that of a fist, and its weight is about 250-300 g. It is located in the chest between the lungs and surrounded by the pericardium. The great vessels which include the superior and inferior vena cava, the pulmonary artery and vein, as well as the aorta are located above the heart. The aortic arch lies behind the heart. The esophagus and the spine lie further behind the heart. An overall view is given in Figure 1.1 (Williams and Warwick 1989).

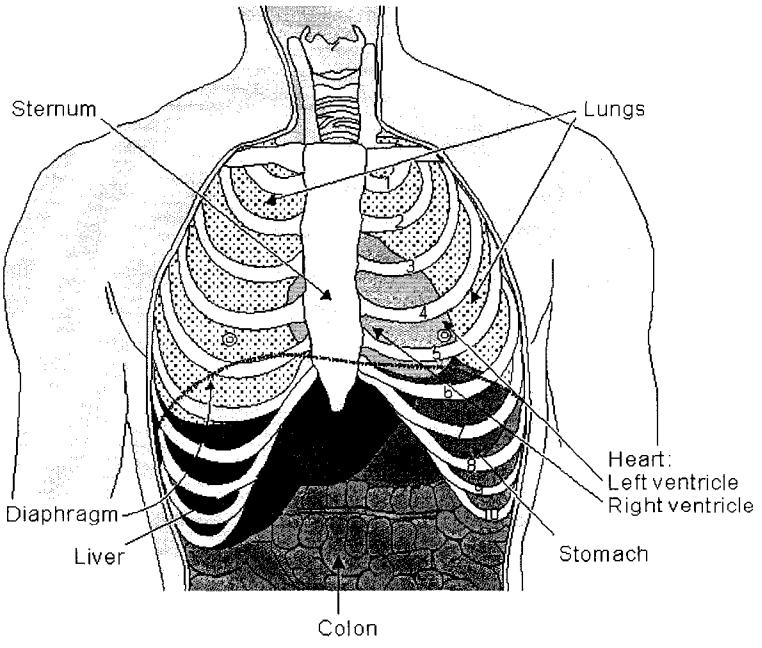

Figure 1.1. Location of the heart in the thorax. It is bounded by the diaphragm, lungs, esophagus, descending aorta, and sternum (Williams and Warwick 1989).

1.1.2 Anatomy of the Heart

The heart consists of four chambers: the right and left atria and ventricles. The heart walls have three layers. The outer layer of the heart wall is the epicardium, the middle layer is the myocardium, and the inner layer is the endocardium. The heart is oriented with the right ventricle towards the anterior chest and the left atrium towards the posterior chest (see Figure 1.2 (Malmivuo and Plonsey 1995)). According to the functions, the heart chamber walls have different thicknesses to assure the amount of force each chamber is required to generate. The two atria are thin-walled chambers that receive blood from the veins. The two ventricles are thick-walled chambers that forcefully pump blood out of the heart requiring higher pressure than receiving blood from the veins. Comparing the two ventricles, the left ventricular walls are much thicker than the right ventricular walls since the left ventricle needs higher pressure to pump

blood to the systemic circulation than the right ventricle which provides pulmonary circulation.

The heart has four valves. The tricuspid valve is at the exit of the right atrium, and the mitral valve is at the exit of the left atrium. The pulmonary valve lies between the right ventricle and the pulmonary artery, while the aortic valve lies in the outflow tract of the left ventricle. When each chamber contracts, the valve at its exit opens to allow blood to flow out. When the contracting finishes, the valve closes to prevent the backflow of blood.

Deoxygenated blood returns to the heart via the superior and inferior vena cava, enters the right atrium, goes through the tricuspid valve to the right ventricle, and from there it is ejected to the lungs. Oxygenated blood returning from the lungs enters the left atrium via the pulmonary veins, passes into the left ventricle through the mitral valve, and is then ejected to the aorta and the systemic circulation through the aortic valve.

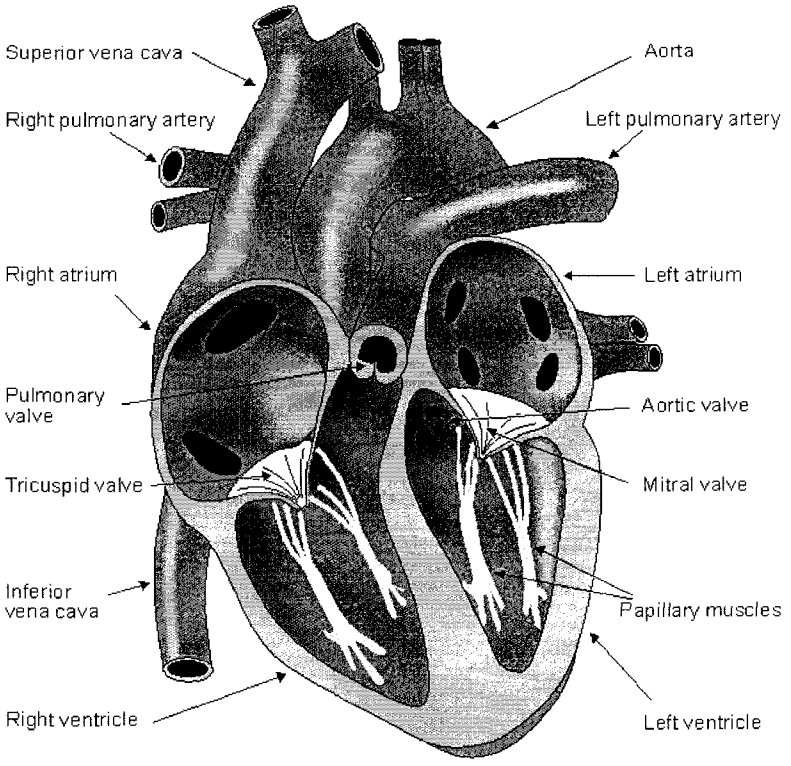

Figure 1.2. The anatomy of the heart and associated vessels (Malmivuo and Plonsey 1995).

1.1.3 Electrical Activity of the Heart

The sequence of electrical activity within the heart is displayed in Figure 1.3 (Bianco 2000) and occurs as follows:

As the natural pacemaker of the heart, the sinoatrial (SA) node (Figure 1.3 (1)), without any neural stimulation, initiates electrical impulses 70 to 80 per minute. Each electrical impulse travels through the right and left atrium causing the two upper chambers of the heart to contract together.

After the depolarization has propagated over the atrial walls, it reaches the atrio-ventricular (AV) node (Figure 1.3 (2)) which is located at the border of the left atrium and ventricle. Here, there is a natural delay which allows the right and left atrium to continue contracting and emptying their blood into the two ventricles.

Following the delay, the electrical impulse goes to the bundle of His (Figure 1.3 (3)), then it divides into the right and left bundle branches (Figure 1.3 (4)) where it rapidly spreads to the inner walls of the right and left ventricles using Purkinje fibers (Figure 1.3 (5)).

After a while the depolarization front has propagated through the wall of the two ventricles; when it first arrives at the epicardial surface of the ventricular free walls, the event is called breakthrough. Since the left ventricular wall is thicker, activation of the left ventricular free wall continues even after the large part of the right ventricle finishes depolarization. The breakthrough of the left ventricle happens later than the right ventricle. The last to depolarize are basal regions of both left and right ventricles. After each ventricular muscle region has depolarized, repolarization occurs to allow the muscle relaxing and blood filling up the heart again. Repolarization is not a propagating phenomenon, and since the duration of the action impulse is much shorter at the epicardium than at the endocardium, the termination of activity appears as if it were propagating from epicardium toward the endocardium.

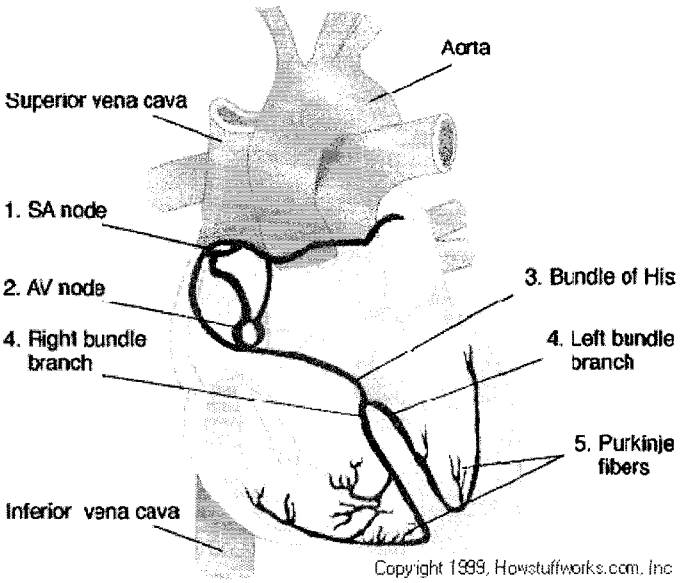

Figure 1.3. The conduction system of the heart (Bianco 2000).

Any of the electrical tissue in the heart can act as a pacemaker. However, since the SA node generates the fastest electrical impulse than other tissues, it sets the activation frequency of the whole heart. If the connection between the atria and the AV node fails, the AV node takes over and acts as a pacemaker, although at a slower rate than SA node. If the conduction system fails at the bundle of His, the ventricles will be in control with their highest intrinsic frequency. The waveforms of action impulse observed in different specialized cardiac tissue are shown in Figure 1.4 (Malmivuo and Plonsey 1995).

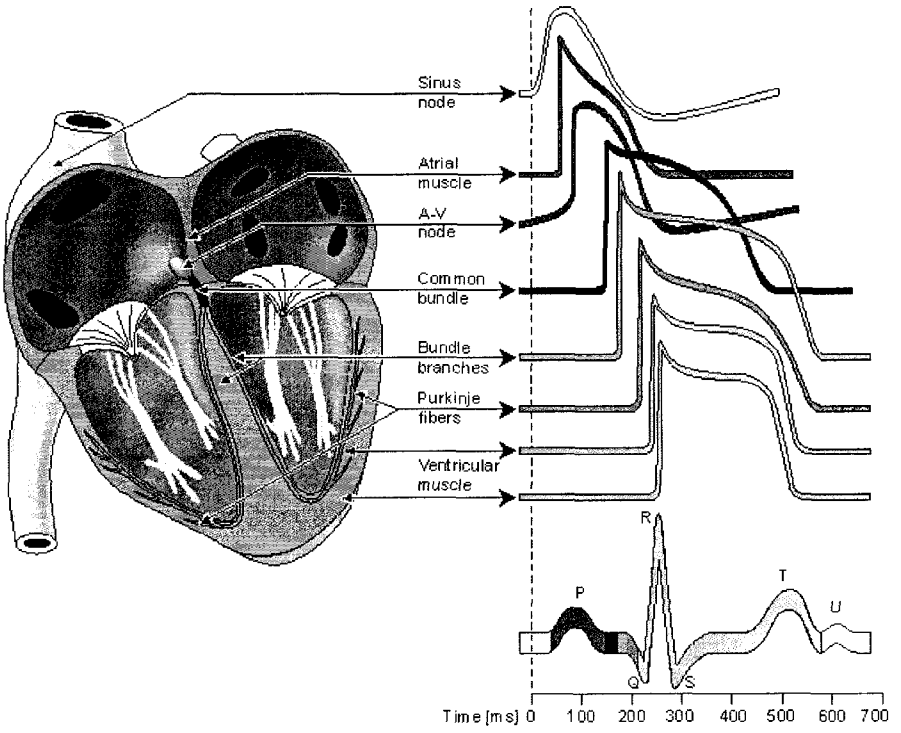

Figure 1.4. Electrophysiology of the heart. The different waveforms for each of the specialized cells found in the heart are shown (Malmivuo and Plonsey 1995).

1.1.4 Cardiac Cycle

The cardiac cycle refers to the alternating contraction and relaxation of the myocardium during one heartbeat. Systole is the contraction phase of the cardiac cycle which pumps blood out of the heart, and diastole is the relaxation phase which relaxes the heart muscle before the next heartbeat. At a normal heart rate, one cardiac cycle lasts for 800 ms.

1.2 Traditional Non-invasive ECG and Mapping

1.2.1 12-lead ECG System

The electrical activity of the heart can be recorded non-invasively at the surface of the body. The most commonly used clinical ECG system, the 12-lead ECG system, consists of the following 12 leads, I, II, III, aV_R, aV_L, aV_F, and V_1~V_6 (Figure 1.5), which

are called the limb, augmented and precordial leads. Figure 1.5 (Malmivuo and Plonsey 1995) shows the measurement points on the body surface which are used to derive and measure the 12-lead ECG.

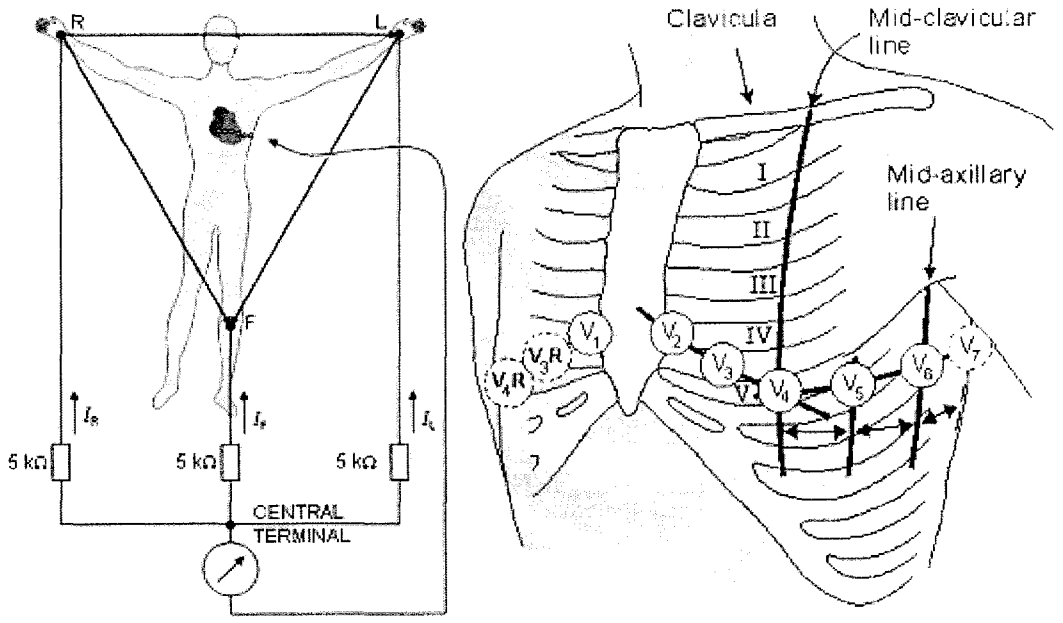

Figure 1.5. The measurement points of the 12-lead ECG system (Malmivuo and Plonsey 1995).

The ECG is composed of waves and complexes which include the P wave, PR interval, PR segment, QRS complex, ST segment, QT interval, and T wave (Figure 1.6).

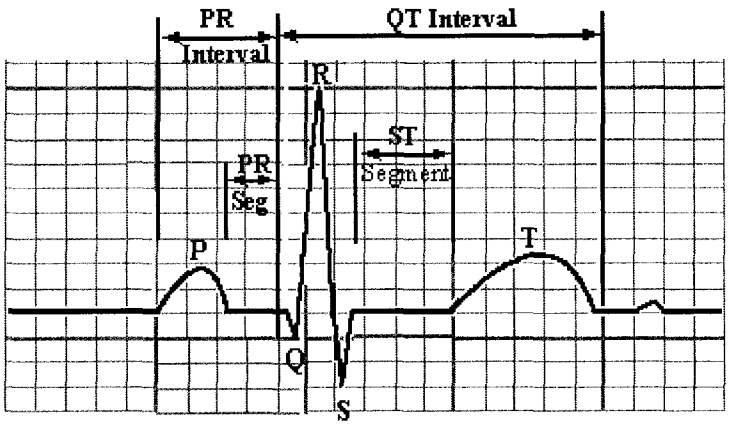

Figure 1.6. One cardiac cycle of ECG waveform.

- The P wave corresponds to atrial depolarization. It is usually smooth and positive. The P wave duration is normally less than 0.12 s.
- The PR interval indicates the ECG wave from the beginning of the P wave, which is the onset of atrial depolarization, to the beginning of the QRS complex, which is the onset of ventricular depolarization. It normally lasts for 0.12 - 0.20 s.
- The PR segment represents the interval from the end of the P wave, which is the end of atrial depolarization, to the beginning of the QRS complex, which is the onset of ventricular depolarization.
- The QRS complex corresponds to the ventricular depolarization which usually lasts from 0.04 ~ 0.12 s.
- The ST Segment represents the period from the end of the QRS complex to the beginning of the T wave. During this time, the ventricles are still contracting.
- The QT interval begins at the onset of the QRS complex and ends at the end of the T wave. It is a time period from ventricular depolarization to ventricular repolarization.
- The T wave corresponds to ventricular repolarization. Normally, it is a positive wave.

Figure 1.7 shows the normal 12-lead ECG waveforms. The 12-lead ECG is useful in providing global temporal assessment, but has limited ability in locating the sources of electric events in the patient. This is important in determining the mechanisms of arrhythmias, which constitute a major cause of death and disability.

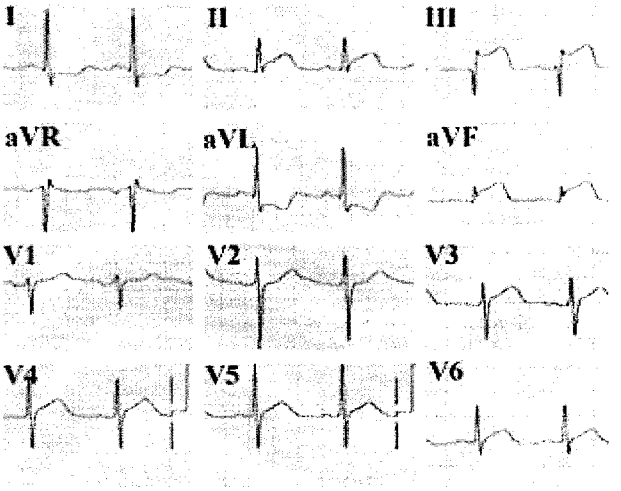

Figure 1.7. Normal 12-lead ECG waveforms.

1.2.2 Body Surface Potential Mapping (BSPM)

BSPM improved the spatial resolution by using a larger number of recording leads over the body surface (Taccardi 1963, Klug *et al.* 1995, De *et al.* 1997, Fenici *et al.* 1998, Takala *et al.* 2001, Fitz-Clarke *et al.* 2006). Figure 1.8 shows examples of the BSPM (Fitz-Clarke *et al.* 2006). From Figure 1.8 we can see the potential distribution over the body surface at different time instants. However, BSPM only reveals limited information about multiple concurrent sources due to the volume conductor between the heart and the body surface smoothes the potential distribution (Rudy and Plonsey 1979, 1980). Due to these limitations, further research has been conducted to improve the spatial resolution of body surface maps.

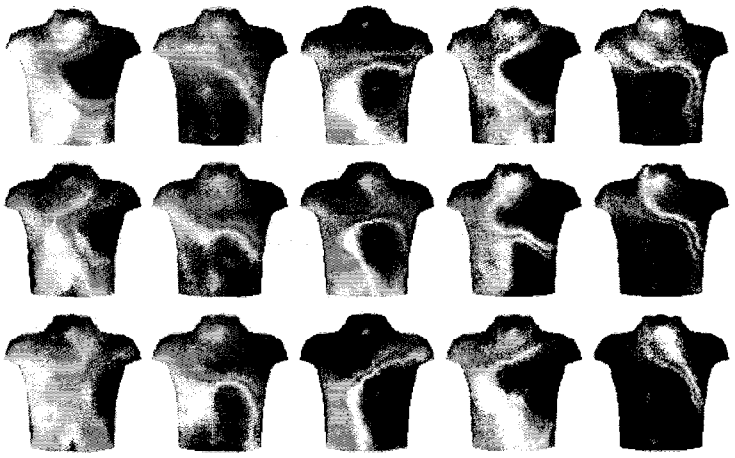

Figure 1.8. BSPMs of a patient during ventricular fibrillation (Fitz-Clarke et al. 2006).

1.3 Laplacian ECG (LECG) and Mapping

The Laplacian is the second spatial derivative of the potentials on the body surface which reduces the smoothing effect of the torso volume conduction and provides more detail in localizing and differentiating multiple concurrent dipole sources (He and Cohen 1992). The surface Laplacian (SL) can also be interpreted as an equivalent current density (He and Cohen 1992, 1995). According to the definition, LECG is the negative of the SL of the body surface potential (He 1997, He and Cohen 1995, He and Wu 1999). LECG on the body surface can be used to perform body surface Laplacian mapping (BSLM). BSLM has been shown to be an alternative to BSPM with better spatial resolution and enhanced capability of localization by using the estimated Laplacian of body surface potentials to create maps (Oostendorp and Oosterom 1996, He and Cohen 1991, 1992, 1995, He and Wu 1999, Umetani *et al.* 1998, Wu *et al.* 1998, 1999, He 1998, Ono *et al.* 1997, Lian *et al.* 2002a, 2002b, Li *et al.* 2002, 2003, He *et al.* 2002, Besio 2001, Besio *et al.* 2001, Besio and Tarjan 2002a, 2002b).

Several studies (Umetani *et al.* 1998, He and Wu 1999, Wu *et al.* 1999, He *et al.* 2002, Lian *et al.* 2002b, Li *et al.* 2003) utilized large numbers of unipolar electrodes placed on the chest surface to measure the body surface potentials, and from that data, the LECG was derived by using a finite difference algorithm, "five-point method" (FPM), or spline LECG estimator. However, there was unavoidable error estimating LECG from surface potentials. For spline LECG estimator, extra information such as the geometric parameters of the body surface need to be obtained by using CT/MRI, etc. before the spline interpolation is performed.

Fattorusso and Tilmant (1949) were the first to use bipolar concentric ring electrodes (BCE) in cardiology. He and Cohen (1991, 1992, 1995) developed a BCE to measure the body surface bipolar LECG directly and demonstrated that LECG has a better spatial resolution in resolving and imaging spatially distributed cardiac electrical activation than body surface potentials (Figure 1.9A).

Lu and Tarjan (1999) developed an active LECG sensor with a tripolar concentric ring electrode (TCE) where the outer ring and the center disc were electrically shorted. This TCE with the outer ring and the center disc shorted is referred to here as a quasi-bipolar sensor (QBS) (Figure 1.9B). Besio (2001), Besio *et al.* (2001), and Besio and Tarjan (2002a, b) demonstrated the efficacy of using this QBS for detecting atrial activation patterns by recording from 35 locations on the chest surface.

To develop a tripolar electrode with fully independent elements Besio *et al.* (2004, 2006) applied the "nine-point method" (NPM), a finite difference algorithm, to approximate the tripolar Laplacian potentials. Based on the NPM, the new active Laplacian TCE sensor does not have the outer ring and the center disc electrically shorted

(Figure 1.9C). This new sensor can record non-directional, site-specific tripolar LECG from the body surface with high spatial resolution and high local selectivity. The difference between the TCE and BCE is that there is no middle ring element in the BCE.

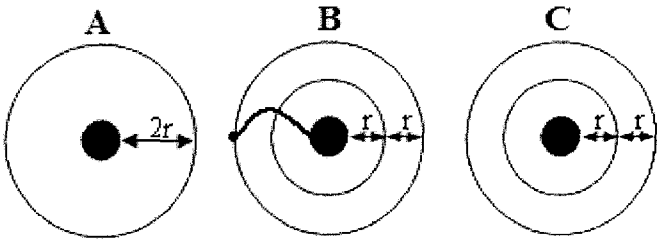

Figure 1.9. Schematics of BCE (A), QBS (B), and TCE (C).

1.4 Comparison between the LECG Estimators

Previous computer simulation and tank experiments (Besio *et al.* 2006) have demonstrated that tripolar LECG provides more detailed spatial information for the underlying source dipoles than bipolar LECG. Further computer simulation and modeling (Soundararajan and Besio 2005) showed tripolar BSLM has better spatial resolution in imaging spatially distributed cardiac electrical activity than bipolar BSLM. He *et al.* (2002) and He and Wu (1999) showed spline LECG had better performance than FPM LECG with higher correlation coefficient as compared with the analytical LECG. It is of interest to compare the tripolar, bipolar, and spline LECG with respect to the analytical LECG.

1.5 The Main Tasks of the Research Project

1.5.1 Computer Simulation

A simple planar surface model and a heart-torso sphere-cylinder model were built in this study. Four types of the concentric ring electrode arrays were modeled covering the planar and cylinder surface with equal spacing. Tripolar, bipolar, and spline LECG

were calculated due to the underlying source dipoles which simulated the cardiac electrical activity. Noise dipoles were also included to simulate the noise contamination situations. The three estimated LECG and BSLM were compared for accuracy, noise attenuation, and spatial resolution with respect to the analytical LECG and BSLM under different dipole configurations and recording electrode numbers. The computer simulation was performed using Matlab® 6.5 (MathWorks, Inc., Natick, Massachusetts).

1.5.2 Human Experiment

The new active Laplacian TCE sensor (Besio and Chen 2006, 2007) was designed to acquire signals. The new sensor array was used to record the tripolar and bipolar LECG directly from 6 healthy human subjects. The averaged cardiac activation cycle of the tripolar and bipolar LECG on the body surface, the tripolar BSLM which shows the Laplacian potential distribution at the time instant of the Lead II ECG R-wave peak, and the tripolar Laplacian moment of activation (MOA) (described further later) isochronal mapping (Besio 2001, Besio *et al.* 2001, Besio and Tarjan 2002a, b) were performed for each subject. The tripolar BSLM was used to relate the multiple earlier activation areas of the tripolar MOA map with respect to the underlying cardiac electrical activations.

CHAPTER 2

BACKGROUND

2.1 LECG

Wu *et al.* (1999) "assumed the body to be a linear, isotropic, and piece-wise homogeneous conductor. The total current density **J** in the body is given by

$$\mathbf{J} = \sigma\mathbf{E} + \mathbf{J}^i \tag{2.1}$$

where σ is the electrical conductivity, **E** is the electric field, and $\mathbf{J}^i$ is the impressed current (Plonsey 1969) actively driven by chemical precesses. $\mathbf{J}^i$ is assumed to be negligible outside the heart. The ohmic current $\sigma\mathbf{E}$ is necessary to avoid buildup of charges due to the source current.

Because the electric field **E** is quasistatic (Plonsey 1969), it can be expressed at each instant of time as the negative gradient of a scalar potential V, and Equation (2.1) may be rewritten as

$$\mathbf{J} = \mathbf{J}^i - \sigma\nabla V \tag{2.2}$$

According to the quasistatic conditions ((Plonsey 1969), the tissue capacitance and inductance are negligible. In other words, the divergence of the total current must be vanishing. Therefore, Equation (2.1) reduces to Possion's equation:

$$\Delta V = \frac{\nabla \mathbf{J}^i}{\sigma} \tag{2.3}$$

where Δ is the three-dimensional (3D) Laplacian operator. Therefore, in a region of the body outside the heart where $\mathbf{J}^i$=0, the electrical potential obeys Laplace's equation

$$\Delta V = 0 \tag{2.4}$$

Considering a local orthogonal curvilinear coordinate system (u_1, u_2, u_3) with the origin at a point on the body surface, the 3D Laplacian of the electric potential is given by (Arfken 1985)

$$\Delta V = \frac{1}{h_1 h_2 h_3}\left[\frac{\partial}{\partial u_1}\left(\frac{h_2 h_3}{h_1}\frac{\partial V}{\partial u_1}\right)+\frac{\partial}{\partial u_2}\left(\frac{h_1 h_3}{h_2}\frac{\partial V}{\partial u_2}\right)+\frac{\partial}{\partial u_3}\left(\frac{h_1 h_2}{h_3}\frac{\partial V}{\partial u_3}\right)\right] \tag{2.5}$$

where h_1, h_2, and h_3 are scale factors of this orthogonal curvilinear coordinate system. If we take u_3 to be the local normal to the body surface, then (u_1, u_2) becomes the local orthogonal surface coordinates. The LECG is defined as the negative of the SL of the body surface potential (He 1997, He and Cohen 1995, He and Wu 1999) and is thus given by

$$L = -L_{surface} \equiv -\Delta_{surface} V = -\frac{1}{h_1 h_2 h_3}\left[\frac{\partial}{\partial u_1}\left(\frac{h_2 h_3}{h_1}\frac{\partial V}{\partial u_1}\right)+\frac{\partial}{\partial u_2}\left(\frac{h_1 h_3}{h_2}\frac{\partial V}{\partial u_2}\right)\right] \tag{2.6}$$

Now assuming that the chest can be approximated by a planar surface in the vicinity of the observation point P, where the LECG is to be estimated, a reasonable approximation of the local area of the chest would be the tangential plane at the point of interest, over which a local Cartesian coordinate system (x, y, z) can be considered. If we assume z to be normal to the tangential plane, the LECG at point P becomes

$$L = -L_{surface} \approx -\left(\frac{\partial^2 V}{\partial x^2}+\frac{\partial^2 V}{\partial y^2}\right) \tag{2.7}$$

which can be interpreted as an equivalent current source as follows (He and Cohen 1995):

$$L = -L_{surface} \equiv -\Delta_{surface} V = \frac{1}{\sigma}\left(\frac{\partial J_x}{\partial x} + \frac{\partial J_y}{\partial y}\right) = -\frac{1}{\sigma}\left(\frac{\partial J_z}{\partial z}\right) \equiv -\frac{j_{eq}}{\sigma} \tag{2.8}$$

This equivalent current source j_{eq} may be interpreted as a two-dimensional (2D) projection of the 3D cardiac electrical source $\mathbf{J}^i$ onto the body surface. The LECG may also be considered as a measure of the surface-directed current density entering the skin layer."

2.2 Bipolar LECG

Bipolar LECG is approximated using BCE LECG active sensor based on FPM. It is a local-based Laplacian. "In Figure 2.1 the Laplacian at point p_0 due to the potentials v_5, v_6, v_7, v_8, and v_0 with spacing of $2r$, which forms the five-point arrangement, can be obtained using the Taylor series expansion and finite difference approximation methods as explained by Ames (1969)

$$\left(\frac{\partial^2 v}{\partial x^2} + \frac{\partial^2 v}{\partial y^2}\right)\Bigg|_{p_0} = \Delta_{surface} p_0 = \frac{1}{(2r)^2}\left(\sum_{i=5}^{8} v_i - 4v_0\right) + O((2r)^2) \tag{2.9}$$

where $O((2r)^2) = \frac{(2r)^2}{4!}\left(\frac{\partial^4 v}{\partial x^4} + \frac{\partial^4 v}{\partial y^4}\right)\Big|_{p_0} + \frac{(2r)^4}{4!}\left(\frac{\partial^6 v}{\partial x^6} + \frac{\partial^6 v}{\partial y^6}\right)\Big|_{p_0} + \cdots$ is the truncation error. The approximation to the Laplacian of potential at p_0 is then

$$\Delta_{surface} p_0 \cong \frac{4}{(2r)^2}\left(\bar{v} - v_0\right) \tag{2.10}$$

where $\bar{v} = \frac{1}{4}\sum_{i=5}^{8} v_i$ is the average of the potentials of the four points.

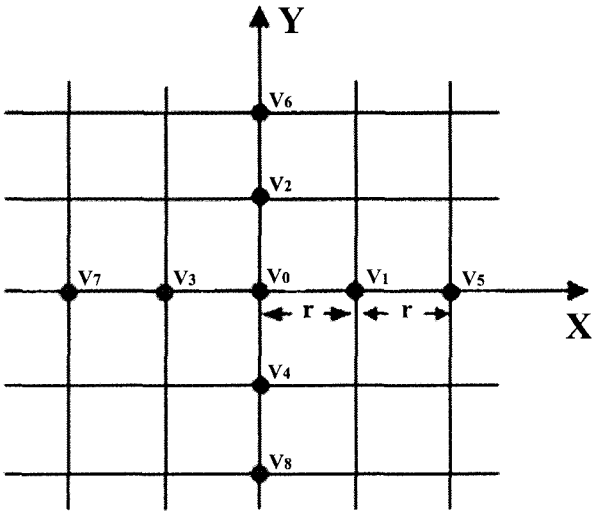

Figure 2.1. Arrangement of FPM and NPM on a regular plane square grid of size N x N. Where r is the inter-point distance, v0 to v8 are the potentials at points p0 to p8 respectively, v5,v6,v7,v8 and v0 form the FPM, and v1, v2, v3, v4, v5, v6, v7, v8 and v0 form the NPM.

According to Huiskamp (1991), the discrete Equation (2.10) can be applied to a BCE system by performing the integral along the circle of radius $2r$ around the point p_0 of the Taylor expansion and defining $X = 2r\cos(\theta)$ and $Y = 2r\sin(\theta)$, as shown in Equation (2.11).

$$\Delta_{surface} p_0 \cong \frac{4}{(2r)^2}\frac{1}{2\pi}\int_0^{2\pi}(v(2r,\theta)-v_0)d\theta \tag{2.11}$$

where $\frac{1}{2\pi}\int_0^{2\pi} v(2r,\theta)d\theta$ is the average potential on the outer ring, and $\frac{1}{2\pi}\int_0^{2\pi} v_0 d\theta$ is the average potential on the center disc." (Besio *et al.* 2004, 2006). Figure 1.9A shows the schematic of the BCE. According to the definition of LECG (He 1997, He and Cohen 1995, He and Wu 1999), LECG is the negative of the SL of the body surface potential. Therefore, the algorithm for approximating the surface bipolar LECG (He and Cohen 1992, Besio *et al.* 2004, 2006) with the BCE is simplified as

$$L_b \cong -\frac{1}{r^2}(V_{or} - V_c) \tag{2.12}$$

where V_{or} is the average potential on the outer ring and V_c is the average potential on the center disc.

2.3 Tripolar LECG

Tripolar LECG is approximated using TCE LECG active sensor based on NPM (Besio *et al.* 2004, 2006). Same as bipolar LECG, tripolar LECG measures the local-based Laplacian. Besio *et al.* (2004, 2006) found "in Figure 2.1, points p_0 to p_8 form the nine-point arrangement. The Laplacian (Lapidus and Pinder 1982) of the potential at point p_0 as a result of the potentials v_0 through v_8 at these respective points is given by

$$\left(\frac{\partial^2 v}{\partial x^2} + \frac{\partial^2 v}{\partial y^2}\right)\Bigg|_{p_0} = \Delta_{surface} p_0 = \frac{1}{12r^2}\left\{16\sum_{i=1}^{4} v_i - 60v_0 - \sum_{i=5}^{8} v_i\right\} + O(r^4) \tag{2.13}$$

where $O(r^4) = \frac{r^4}{270}\left(\frac{\partial^6 v}{\partial x^6} + \frac{\partial^6 v}{\partial y^6}\right)\Big|_{p_0} + \cdots$ is the truncation error.

Compared with Equation (2.9), it can be observed that the NPM truncation error does not have the 4th order derivative term. Therefore, the NPM is considered to be more accurate than the FPM.

The nine-point arrangement can be seen as two FPMs. By applying a similar procedure as was used for the BCE configuration, performing the integral along a circle of radius r around point p_0 of the Taylor expansion and defining $X = r \sin(\theta)$ and $Y = r \cos(\theta)$ (Huiskamp 1991) results in Equation (2.14):

$$\int_0^{2\pi} v(r,\theta)d\theta = \int_0^{2\pi} v_0 d\theta + \frac{r^2}{4} 2\pi\Delta v_0$$

$$+\frac{r^4}{24}\int_0^{2\pi}\sum_{j=0}^{4}(\sin\theta)^{4-j}(\cos\theta)^j d\theta\left(\frac{\partial^4 v}{\partial x^{4-j}\partial y^j}\right)\Bigg|_{p_0}$$

$$+\frac{(2r)^6}{6!}\int_0^{2\pi}\sum_{j=0}^{6}(\sin\theta)^{6-j}(\cos\theta)^j d\theta\left(\frac{\partial^6 v}{\partial x^{6-j}\partial y^j}\right)\Bigg|_{p_0}$$

$$+\ldots \tag{2.14}$$

Similarly, performing the integral along a circle of radius $2r$ around p_0 and defining $X = 2r\sin(\theta)$ and $Y = 2r\cos(\theta)$ (Huiskamp 1991) results in Equation (2.15):

$$\int_0^{2\pi} v(2r,\theta)d\theta = \int_0^{2\pi} v_0 d\theta + r^2 2\pi\Delta v_0$$

$$+\frac{2r^4}{3}\int_0^{2\pi}\sum_{j=0}^{4}(\sin\theta)^{4-j}(\cos\theta)^j d\theta\left(\frac{\partial^4 v}{\partial x^{4-j}\partial y^j}\right)\Bigg|_{p_0}$$

$$+\frac{(2r)^6}{6!}\int_0^{2\pi}\sum_{j=0}^{6}(\sin\theta)^{6-j}(\cos\theta)^j d\theta\left(\frac{\partial^6 v}{\partial x^{6-j}\partial y^j}\right)\Bigg|_{p_0}$$

$$+\ldots \tag{2.15}$$

Combining Equations (2.14) and (2.15) as {16*Equation (2.14) - Equation (2.15)} cancels the fourth order term. Then the approximate solution for the Laplacian at point p_0 is

$$\Delta_{surface} p_0 \cong \frac{1}{3r^2}\left\{16\left(\frac{1}{2\pi}\int_0^{2\pi} v(r,\theta)d\theta - \frac{1}{2\pi}\int_0^{2\pi} v_0 d\theta\right)\right.$$

$$\left.-\left(\frac{1}{2\pi}\int_0^{2\pi} v(2r,\theta)d\theta - \frac{1}{2\pi}\int_0^{2\pi} v_0 d\theta\right)\right\} \tag{2.16}"$$

where $\frac{1}{2\pi}\int_0^{2\pi} v(r,\theta)d\theta$ represents the average potential on the middle ring, namely V_{mr} in

this study, $\frac{1}{2\pi}\int_0^{2\pi} v(2r,\theta)d\theta$ represents the average potential on the outer ring, namely V_{or}, and $\frac{1}{2\pi}\int_0^{2\pi} v_0 d\theta$ represents the average potential on the center disc, namely V_c. Figure 1.9C shows the schematic of the TCE. Therefore, the new algorithm for approximating the surface tripolar LECG with the TCE (Besio *et al.* 2004, 2006, Besio and Chen 2006, 2007) is

$$L_t \cong -\frac{1}{3r^2}[16\times(V_{mr}-V_c)-1\times(V_{or}-V_c)] \tag{2.17}$$

where V_{or}, V_{mr}, and V_c denote the average potentials on the TCE which include outer, middle, and center electrode elements, r is the inter-element distance.

2.4 Spline LECG

Spline Laplacian is a global-based Laplacian. "Consider the nonorthogonal curvilinear coordinate system on a general surface Ω, $u=x$, $v=y$ and $z=f(u, v)$, where $f(u, v)$ is a continuous function whose second-order partial derivatives exist. If $V(u, v)$ is the potential distribution (whose second-order partial derivatives exist) on Ω, the SL of $V(u, v)$ is given by the following equation:

$$\Delta V(u,v)=\frac{1}{\sqrt{g}}\left(\frac{\partial}{\partial u}\left(\sqrt{g}\right)\left(g^{11}\frac{\partial V}{\partial u}+g^{12}\frac{\partial V}{\partial v}\right)\right.$$
$$\left.+\frac{\partial}{\partial v}\left(\sqrt{g}\right)\left(g^{21}\frac{\partial V}{\partial u}+g^{22}\frac{\partial V}{\partial v}\right)\right) \tag{2.18}$$

where the components of the metric tensor are computed as follows:

$$g=1+\left(\frac{\partial f}{\partial u}\right)^2+\left(\frac{\partial f}{\partial v}\right)^2 \quad \ldots\ldots \quad g^{11}=\frac{1+\left(\frac{\partial f}{\partial v}\right)^2}{g}$$

$$g^{12} = g^{21} = \frac{-\frac{\partial f}{\partial u}\frac{\partial f}{\partial v}}{g} \ldots\ldots g^{22} = \frac{1+\left(\frac{\partial f}{\partial u}\right)^2}{g} \tag{2.19}$$

Since in real applications, only limited numbers of potential recordings and body surface geometric coordinate samplings are available, *V(u, v)* and *f(u, v)* are interpolated using spline interpolation.

The mathematical model of the body surface geometry *z=f(x, y)* can be described by 2D thin plate spline

$$z = f(x,y) = \sum_{i=1}^{N} p_i K_{m-1} + Q_{m-1}$$

$$= \sum_{i=1}^{N} p_i d_i^{2(m-1)} \log(d_i^2 + w^2) + \sum_{d=0}^{m-1}\sum_{k=0}^{d} q_{dk} x^{d-k} y^k \tag{2.20}$$

where m (spline order) is set to two, N is the number of body surface geometric coordinate samplings, $d_i^2 = (x-x_i)^2 + (y-y_i)^2$, and w is a constant. The coefficients p_i and q_{dk} are the solutions of following matrix equation

$$\begin{pmatrix} K+\omega I & E \\ E^T & 0 \end{pmatrix} \bullet \begin{pmatrix} P \\ Q \end{pmatrix} = \begin{pmatrix} Z \\ 0 \end{pmatrix} \tag{2.21}$$

where

$$K = (k_{ij}) = K_{m-1}(x_i - x_j, y_i - y_j)$$

$$E = \begin{pmatrix} 1 & x_1 & y_1 & x_1^2 & x_1 y_1 & \cdots & x_1 y_1^{m-2} & y_1^{m-1} \\ 1 & \cdot & \cdot & \cdot & \cdot & \cdot & \cdot & \cdot \\ 1 & \cdot & \cdot & \cdot & \cdot & \cdot & \cdot & \cdot \\ 1 & \cdot & \cdot & \cdot & \cdot & \cdot & \cdot & \cdot \\ 1 & x_N & y_N & x_N^2 & x_N y_N & \cdots & x_N y_N^{m-2} & y_N^{m-1} \end{pmatrix}$$

$$Q^T = (q_{00} \quad q_{01} \quad q_{11} \quad \cdots \quad q_{m-1m-1})$$

$$P^T = (p_1 \quad p_2 \quad p_3 \quad \cdots \quad p_N)$$
$$Z^T = (z_1 \quad z_2 \quad z_3 \quad \cdots \quad z_N) \tag{2.22}$$

and I is the identity matrix, parameter ω is used to improve the numerical stability of the system.

Similarly, the body surface potential distribution over the 3D space at an arbitrary point *(x, y, z)* can be modeled by the 3D spline as

$$V(x,y,z) = \sum_{i=1}^{N} t_i H_{m-1} + R_{m-1}$$
$$= \sum_{i=1}^{N} t_i r_i^{2(2m-3)/2} + \sum_{d=0}^{m-1}\sum_{k=0}^{d}\sum_{g=0}^{k} r_{dkg} x^{d-k} y^{k-g} z^{g} \tag{2.23}$$

where *m* (spline order) is set to three, $r_i^2 = (x-x_i)^2 + (y-y_i)^2 + (z-z_i)^2$, the coefficients t_i and r_{dkg} can be determined by solving the matrix equation

$$\begin{pmatrix} H+\lambda I & F \\ F^T & 0 \end{pmatrix} \bullet \begin{pmatrix} T \\ R \end{pmatrix} = \begin{pmatrix} V \\ 0 \end{pmatrix} \tag{2.24}$$

where

$$H = (h_{ij}) = H_{m-1}(x_i - x_j, y_i - y_j, z_i - z_j)$$

$$F = \begin{pmatrix} 1 & x_1 & y_1 & z_1 & \cdots \\ \cdot & \cdot & \cdot & \cdot & \cdot \\ \cdot & \cdot & \cdot & \cdot & \cdot \\ \cdot & \cdot & \cdot & \cdot & \cdot \\ 1 & x_N & y_N & z_N & \cdots \end{pmatrix}$$

$$R^T = (r_{00} \quad r_{01} \quad r_{11} \quad \cdots \quad r_{m-1m-1})$$
$$T^T = (t_1 \quad t_2 \quad t_3 \quad \cdots \quad t_N)$$
$$V^T = (v_1 \quad v_2 \quad v_3 \quad \cdots \quad v_N) \tag{2.25}$$

and parameter λ is used to improve the numerical stability of the system." (He *et al.* 2002).

Similar to bipolar and tripolar LECG, the spline LECG is defined as the negative SL of the spline interpolated potential.

CHAPTER 3

METHODS

3.1 Computer Simulation

3.1.1 Simple Planar Surface Model

The computer simulation was performed using Matlab® 6.5. We first simulated a basic situation for the planar model. An x-y plane with the origin at the plane's center was used. One radial source dipole, which was perpendicular to the 20 by 20 cm planar surface, was located 5 cm below the center of the plane. Tripolar and bipolar concentric ring electrodes as well as disc electrodes were modeled covering the planar surface with equal spacing. The whole surface was divided into grids with a resolution of 0.05 cm. Figure 3.1 shows the planar surface model with 5×5 electrodes.

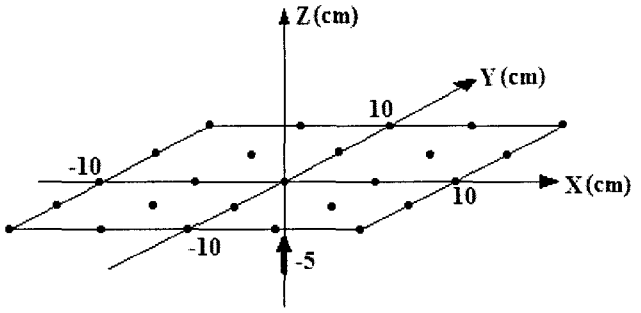

Figure 3.1. The planar surface model with 5×5 electrodes. The dots represent the electrodes on the planar surface. The arrow represents the dipole which is perpendicular to the planar surface.

3.1.2 Simplified Heart-torso Model

A simplified human heart-torso model was developed. Based on the normal human heart-torso dimensions, the heart was modeled as a sphere with a radius of 5 cm. The torso, truncated at the neck, waist and arms, was represented using a single-layer cylinder with a circumference of 100 cm (radius of 15.9 cm) and a height of 40 cm. This human heart-torso model was approximated as a homogeneous conductor with a single normalized interior conductivity of 1.0. A sphere was located inside the torso cylinder eccentrically with an eccentricity of 37% to model the heart. In the following text, all the Cartesian coordinates (x, y, z) were with respect to the heart sphere center. Therefore, the heart sphere center was set to (0, 0, 0) and the torso cylinder center was located at (3.18, -4.89, 0). Figure 3.2 shows the schematic illustration of the heart-torso sphere-cylinder model as seen from the top. The cylindrical surface of the torso was divided into a 2000 by 800 grid with a resolution of 0.05 cm.

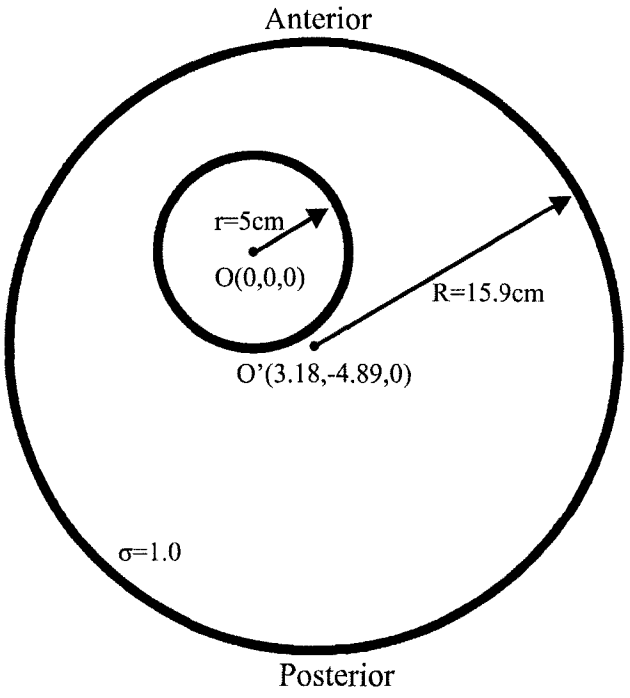

Figure 3.2. Schematic illustration of the heart-torso sphere-cylinder model. The inner and outer circles represent the epicardial and torso surface as seen from the top respectively. O and O′ refer to the centers of the heart sphere and the torso cylinder.

When calculating the spline LECG, for a torso cylinder, the body surface geometry z=f(x, y) does not need to be described using spline interpolation. Only the body surface potential needs spline interpolation. When deriving the body SL, the Cartesian coordinates *(x, y, z)* were changed to the cylindrical coordinates *(r, θ, z)* to calculalte the second spatial derivative to *θ and z* which are tangential to the cylinder surface.

3.1.3 TCE and BCE

TCE and BCE (Figure 3.3) were modeled covering the simple plane and simplified torso cylinder surface to approximate the tripolar and bipolar LECG and body surface potential. The concentric ring electrode included three elements: a center disc with a radius of 0.01 cm, a concentric middle ring with 0.06 cm thickness and an inner

radius (from the center of the center disc to the inner edge of the middle ring) of 0.855 cm, and a concentric outer ring with 0.06 cm thickness and an inner radius (from the center of the center disc to the inner edge of the outer ring) of 1.74 cm. The inter-element distance was 0.885 cm. The concentric ring electrode was assumed flexible to cover both the plane and curvilinear surface. The center disc, middle ring, and outer ring covered 1, 174, 334 nodes respectively on the planar or torso cylinder surface. The potential of each element was calculated by taking the average potential of all nodes within the inner and outer radii of each element as follows:

$$V_{element} = \frac{1}{M}\sum_{i=1}^{M} v_i \tag{3.1}$$

where $V_{element}$ represents the average potential of the center disc, middle ring or outer ring, M is the number of the nodes that make up each element, and v_i is the potential at the ith node. By activating different disc and ring elements, unipolar electrode, TCE, and BCE were achieved. When only the center disc was active, the body surface potential was calculated and used to approximate spline LECG by using equations presented in He *et al.* (2002) (Equations (2.18) ~ (2.25)). When only the center disc and outer ring were active, bipolar LECG was obtained based on Equation (2.12). When all three elements were active, tripolar LECG was obtained directly using Equation (2.17).

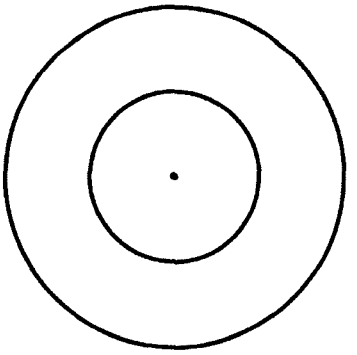

Figure 3.3. Schematic of the simulated TCE and BCE. For BCE, the middle ring is not used.

Four types of arrays $5 \times 5=25$, $9 \times 9=81$, $11 \times 11=121$, and $17 \times 17=289$ of concentric ring electrodes were employed to encompass the planar surface and the anteriolateral area of the torso cylinder surface which had the same area. The reason these four arrays were chosen is because they are symmetric in the encompassing area and there are nine recording sites common to each array. Figure 3.4 shows the four types of arrays of $5 \times 5=25$ (triangle), $9 \times 9=81$ (square), $11 \times 11=121$ (circle), and $17 \times 17=289$ (dot) concentric ring electrodes encompassing the surface. The nine dark bold dots represent the nine common recording sites to each electrode array. The spatial sampling rates of the four electrode arrays were 5 cm, 2.5 cm, 2 cm, and 1.25 cm, respectively.

Figure 3.5 shows the 3D heart-torso model with an array of $17 \times 17=289$ concentric ring electrodes which was modeled using Matlab® 6.5. The sphere represents the heart and the cylinder represents the torso. The dots on the torso cylinder surface represent the centers of the recording electrodes. The two solid arrow lines indicate the central column, namely the 9^{th} column in 17×17 electrode array. When analyzing 81, 121, and 289 electrodes, the distance between the centers of two adjacent electrodes, the spatial sampling rate, was smaller than the diameter of the modeled concentric ring

electrode (3.6 cm). In this situation the electrodes were overlapped with each other. However, this would not influence our computer simulation results since the simulation calculated the average potentials of the three elements on each concentric ring electrode separately. In a real application, this issue would be resolved by translating the electrodes (Besio and Chen 2006, 2007).

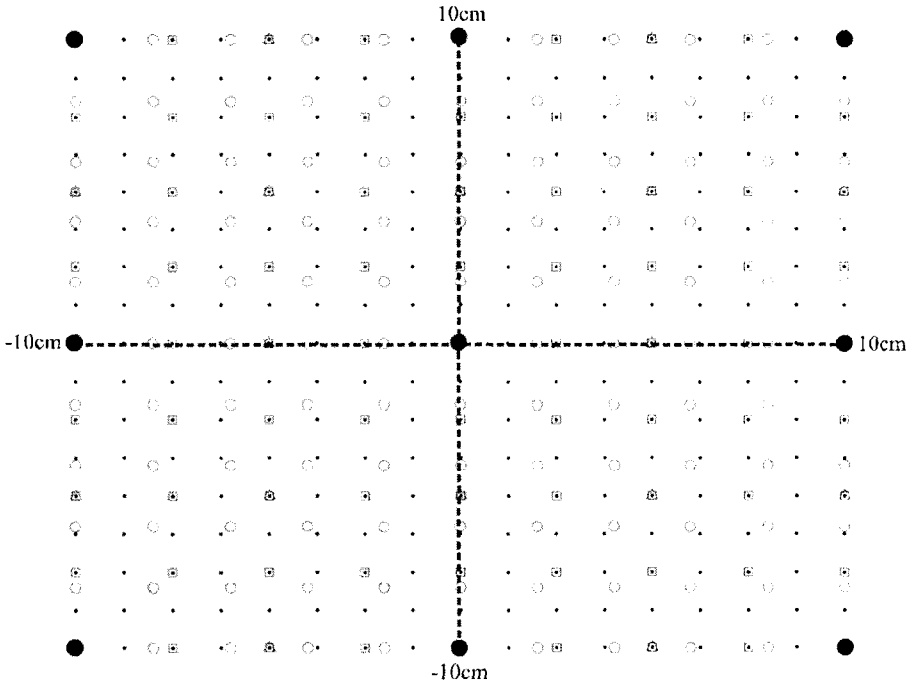

Figure 3.4. Four types of arrays of 5 × 5=25 (triangle), 9 × 9=81 (square), 11 × 11=121 (circle), and 17 × 17=289 (dot) concentric ring electrodes encompassing the planar or torso cylinder surface. The two dashed lines represent the x and y axes in the planar surface or the nipple line and sternal midline in the torso cylinder surface respectively. The nine dark bold dots represent the nine common recording sites to each electrode array.

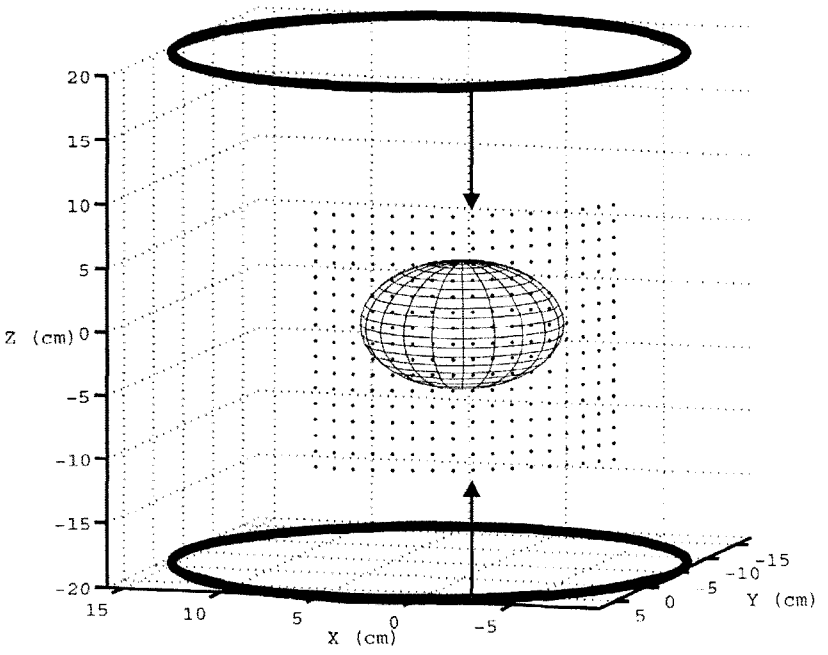

Figure 3.5. 3D heart-torso model with 17×17=289 concentric ring electrodes encompassing the anteriolateral area of the torso cylinder surface.

3.1.4 Source Dipole Models

Previous studies (He *et al.* 1997, He and Wu 1997, 1999, He and Cohen 1992, 1995) have demonstrated that dipoles can be used to simulate the underlying cardiac electrical activities. In this study two kinds of source dipole models were used: (1) radial dipoles representing localized wavefronts propagating from the endocardium to the epicardium; and (2) tangential dipoles representing ectopic myocardial activities. By changing the number and location of source dipoles, various dipole configurations were simulated, which will be presented later. The body surface potential v at one node on the plane or torso cylinder surface due to one dipole was calculated as follows:

$$v = \frac{q}{4\pi\varepsilon_0\varepsilon_r}\frac{z}{r^3} \tag{3.2}$$

where ε_0 and ε_r are permittivity of the free space and body volume, q is the dipole charge, z is the distance between the node and the surface perpendicular to the dipole

moment, and r is the distance between the dipole and the node. In our simulation, the factor $q/4\pi\varepsilon_0\varepsilon_r$ was set to 1 for all source dipoles. If there is more than one dipole located inside the heart sphere simulating the cardiac electrical activities, the potential at one node on the torso cylinder surface due to these dipoles is the summation of the potentials due to each dipole.

For a cylindrical approximation of the body surface, the 3D Laplacian of the body surface potential in a cylindrical system (r,θ,z) becomes

$$\Delta v = \frac{\partial^2 v}{\partial r^2} + \frac{1}{r}\frac{\partial v}{\partial r} + \frac{1}{r^2}\frac{\partial^2 v}{\partial \theta^2} + \frac{\partial^2 v}{\partial z^2} \tag{3.3}$$

Therefore, the analytical LECG on the torso cylinder surface is calculated as

$$L_a = -\Delta_{surface} v = -\left(\frac{1}{r^2}\frac{\partial^2 v}{\partial \theta^2} + \frac{\partial^2 v}{\partial z^2}\right)\Bigg|_{r=R} \tag{3.4}$$

where L_a designates the analytical LECG and R is the radius of the torso cylinder.

3.1.5 Potential Noise

In reality, when recording LECG on the body surface, there is always noise contaminated with the recorded signals, such as electromyogram (EMG) or the noise caused by the slight body movement. In order to test the noise attenuation of the three LECG estimators, the potential noise (PN) level of 0%, 3%, 5%, 10%, 15%, 20%, and 25% of the magnitude of the source dipoles was included by randomly activating the noise dipoles around the source dipoles. In this study, the PN level was defined as the square of the ratio between the factor $q/4\pi\varepsilon_0\varepsilon_r$ (Equation (3.2)) of the noise and source dipoles. For example, to add two noise dipoles as the PN with 25% noise level, the factor $q/4\pi\varepsilon_0\varepsilon_r$ of each noise dipole may be set to 0.5 units. All PN contamination situations were modeled using 289 electrodes which provide better mapping resolution.

3.1.6 Spatial Resolution

In order to compare the capability of the BSLM of 289 recording electrodes for separating two cardiac electrical activities, two dipoles oriented perpendicular to the torso cylinder surface, which were located at the same depth of 10 cm from the surface with separation distances of 6 cm, 7 cm, 8 cm, and 9 cm, were used to represent two anterior wavefronts propagating to the torso surface. An example diagram of the normalized plot is shown in Figure 3.6, which was along the cross-section of the torso cylinder with the plane where the centers of the two dipoles were located. The separation coefficient (SC) was used in this study to visualize and quantify the comparison. Since the dipoles were oriented to the central column of the electrode array, the LECG of the 17 electrodes in the 9^{th} column, which are indicated by the solid arrow lines on the torso cylinder surface in Figure 3.5, were used to create the plot. Here, the SC is calculated based on the following equation (Wu *et al.* 2000):

$$SC = \frac{a_1 + a_2}{b_1 + b_2} \tag{3.5}$$

where the terms a_1, a_2, b_1, and b_2 are shown in Figure 3.6. b_1+b_2 equals the distance between the two dipoles, a_1 and a_2 are the LECG magnitude with units of [mV cm^{-2}] due to these two dipoles, respectively. It should be pointed out that a deeper valley between two peaks indicates a greater SC and differentiates the two activities more efficiently.

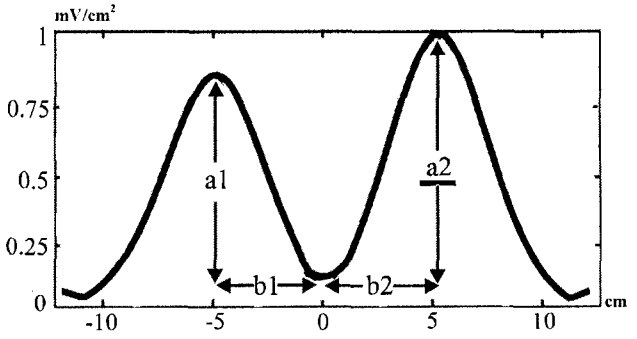

Figure 3.6. The schematic for the spatial resolution calculation, SC.

3.1.7 Comparison Parameter

The accuracy of the three LECG estimators was evaluated by computing the root-mean square error (RMSE) between the estimated and analytical LECG on the planar and simplified torso cylinder surface, respectively. Here, the RMSE is calculated based on the formula as follows:

$$RMSE = \sqrt{\frac{1}{N}\sum_{i=1}^{N}\left(L_{\varepsilon,i} - L_{a,i}\right)^2} \tag{3.6}$$

where $L_{\varepsilon,i}$ and $L_{a,i}$ denote the normalized estimated (tripolar, bipolar, or spline) and analytical LECG at each recording site, respectively. N denotes the number of the recording sites and was set to 25, 81, 121, and 289, respectively, for different recording arrays.

One way ANOVA analysis was performed with the one-tail paired two-sample t-Test for pairwise comparisons among the RMSE of the estimated LECG with different recording electrodes.

Figure 3.7 shows the diagram of the computer simulation.

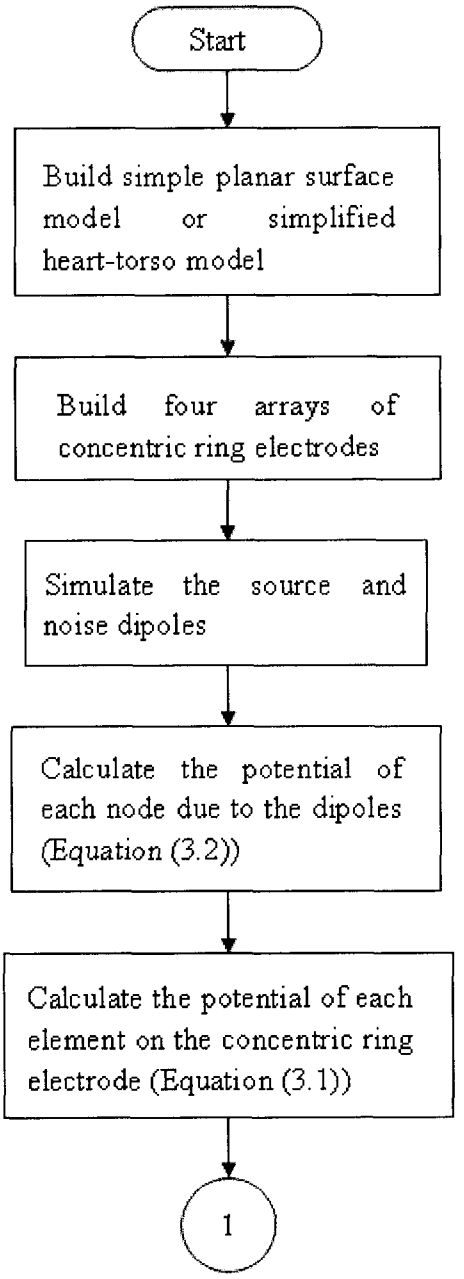

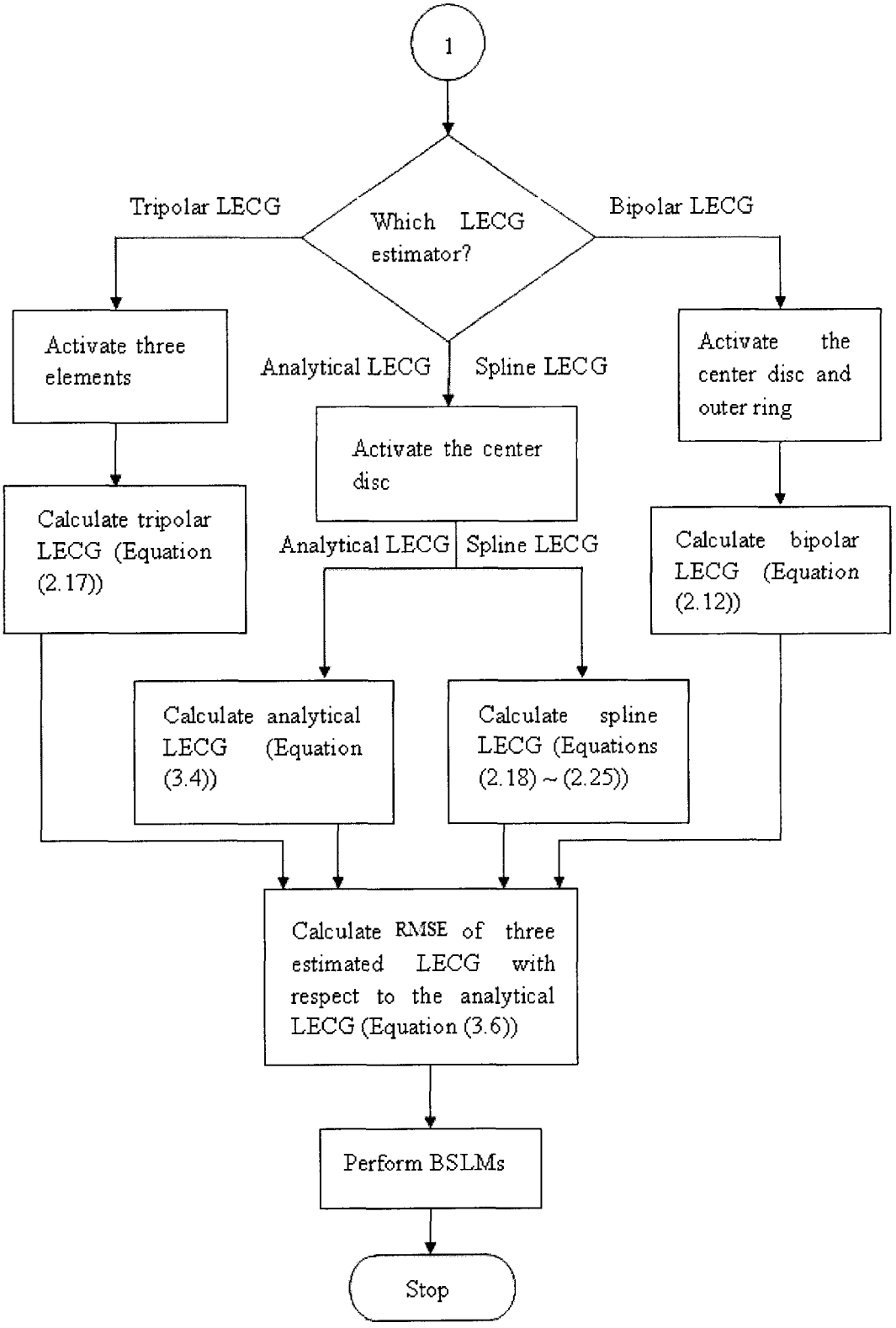

Figure 3.7. Diagram of the computer simulation.

3.2 Human Experiment

3.2.1 Design of Active LECG TCE Sensor and Signal Pre-processing

The active sensor and signal pre-processing were developed using the TCE for acquiring body surface tripolar LECG. Based on Equation (2.17) (Besio *et al.* 2004, 2006, Besio and Chen 2006, 2007), the new active LECG TCE sensor was designed as shown in Figure 3.8.

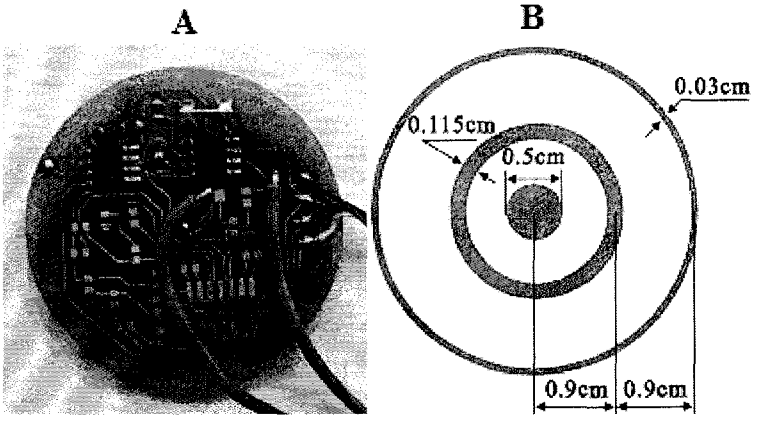

Figure 3.8. The new active LECG TCE sensor. A. The circuit side of the sensor. Two flexible shielded cables were used to connect the signals from the instrumentation amplifiers to a Grass amplifier system (Grass Telefactor, 15LT, W. Warwick, RI, USA). B. Schematic of the electrodes.

On the new active LECG TCE sensor, two ultra high input impedance and high common-mode rejection ratio (CMRR) instrumentation amplifiers (IA) were used for the first stage amplification of signals from the TCE. These two IAs performed the two potential differences between each concentric ring and the center disc. The gains of the first stage amplification were both set to 10. The output signals from these two IAs were connected to a Grass amplifier system (1 Hz to 500 Hz, gain 2,000; total gain 20,000) through two flexible shielded cables as shown in Figure 3.8A. After going through the

Grass amplifier, two potential differences between each concentric ring and the center disc, which are the outputs from the two IAs, were digitized (described later) and then pre-processed based on Equation (2.17) to estimate the tripolar LECG. In pre-processing, two potential differences were multiplied by 1 (for the difference between the outer ring and the center disc) and 16 (for the difference between the middle ring and the center disc), respectively. Then the difference between these two weighted potential differences was divided by a factor of $3r^2$ to get the tripolar LECG.

The two IAs are implemented on one side of a printed circuit board (PCB). Figure 3.8A depicts the circuit side of this new design. On the other side of the sensor board are the TCE which are gold-plated copper for good electrical conductivity. The dimensions of the TCE are shown in Figure 3.8B. The potential differences between each concentric ring and the center disc are recorded simultaneously to acquire LECG.

To determine whether the tripolar LECG provides better spatial selectivity than the bipolar LECG (He and Cohen 1992, Besio *et al.* 2006), tripolar and bipolar LECG were recorded simultaneously and compared in this study. Based on Equation (2.12), the bipolar LECG was obtained as the negative value of the outer ring to the center disc potential difference divided by a factor of r^2 (He and Cohen 1992, Besio *et al.* 2006). Therefore, in pre-processing, only one IA's output which measured the potential difference between the outer ring and the center disc was used to estimate the bipolar LECG. Thus, the tripolar and bipolar LECG were recorded simultaneously with the same conditions. Figure 3.9 shows the diagram of the signal pre-processing to calculate the tripolar and bipolar LECG. The signal pre-processing was performed using Matlab® 6.5.

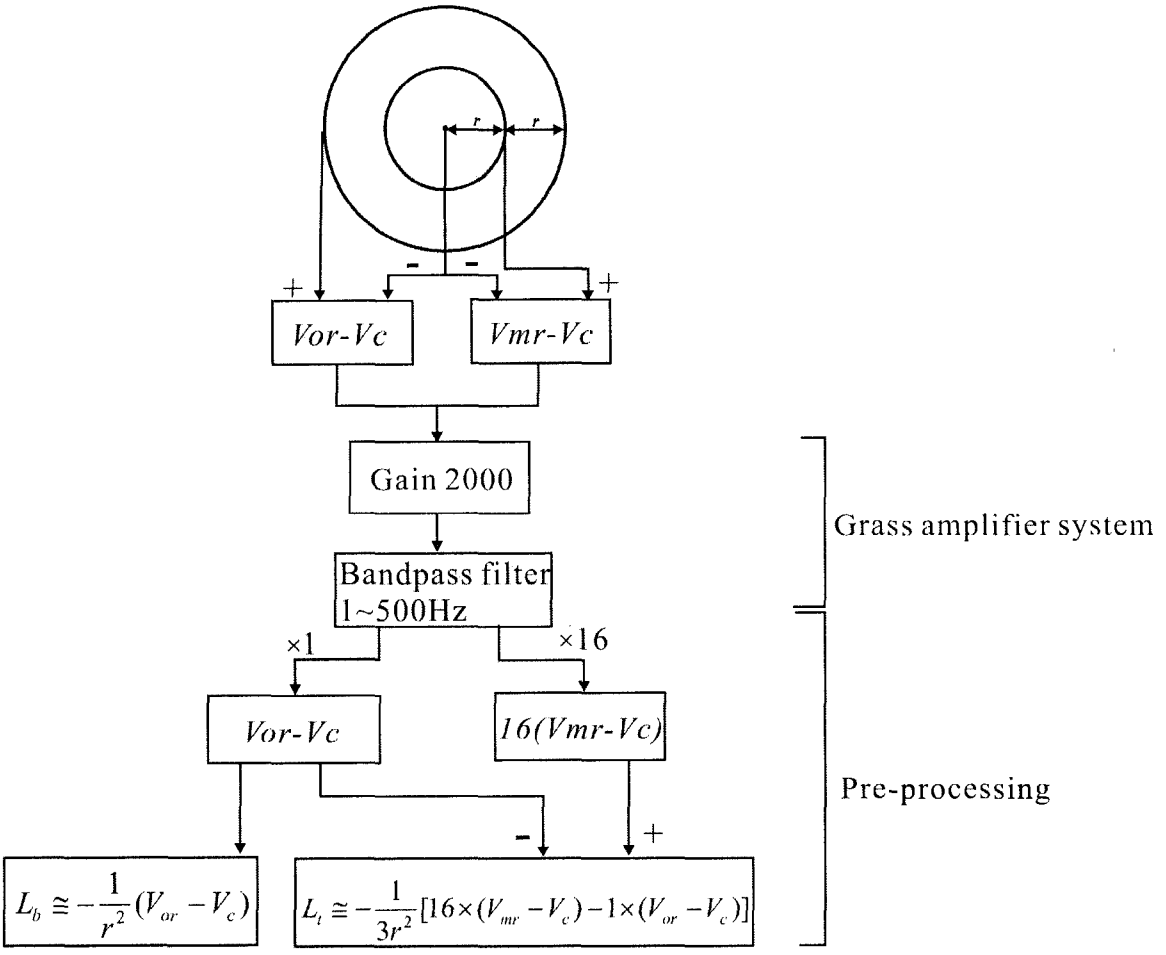

Figure 3.9. The diagram of the signal pre-processing to get the tripolar and bipolar LECG.

3.2.2 Data Acquisition System

Six active LECG TCE sensors and one Lead II ECG sensor, which served as a time reference, were used to record the cardiac body surface data. Thirteen channels of data, two for each active LECG TCE sensor, which recorded the potential differences between the two concentric ring electrodes and the center disc, and one for the Lead II ECG sensor, were recorded simultaneously to a battery-powered laptop with a 16-bit A/D converter, Dataq Instruments DI-720 Series (Akron, Ohio, USA). The analog signals from the Grass amplifier were digitized at a sampling rate of 2,000 Hz over a 30-second

episode to achieve 1/2 ms resolution. The active LECG TCE sensors were also battery-powered. Figure 3.10 shows the cardiac data acquisition system which was used in this study.

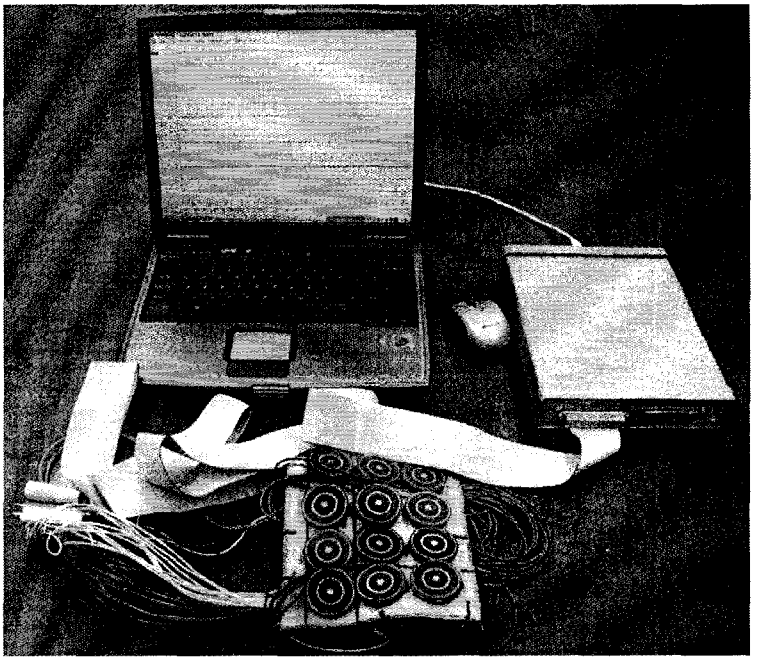

Figure 3.10. The cardiac data acquisition system.

3.2.3 LECG Acquisition from Human Subjects

All signal acquisition was performed in accordance with the Louisiana Tech University IRB approved protocol (Appendix A). Signals were recorded from six healthy male subjects 20-25 years of age. The six active LECG TCE sensors were attached inside a wide elastic strap as shown in Figure 3.11. The strap was wrapped around the body to hold the electrodes in place. Since the human body does not have a uniform shape, it usually took three or four times to wrap the body to adjust the strap to get good contact between the electrodes and body surface. A thin coat of Ten20 electrode paste (D. O. Weaver and Co, Aurora, CO, USA) was spread uniformly on the electrodes to improve

the contact between the electrodes and body surface. Figure 3.12 shows the cardiac data recording from one of our subjects.

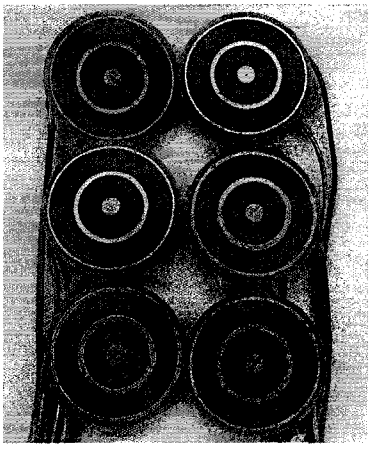

Figure 3.11. The electrode side of six active LECG TCE sensors configured in a 3 row by 2 column matrix and attached to the inside of a wide elastic strap. Three gold-plated electrode elements on each sensor's back side make contact with the body surface.

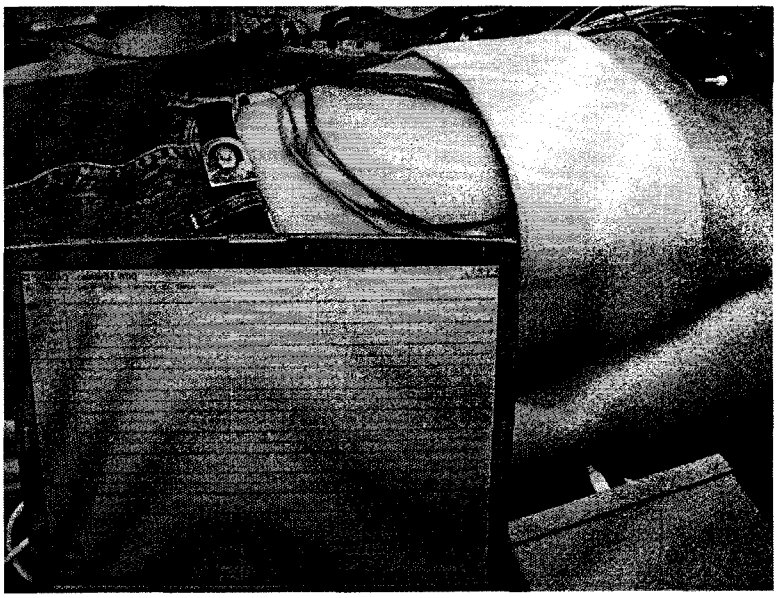

Figure 3.12. Cardiac data recording from one subject.

While recording, the subjects lay in a supine position and were asked to relax and remain stationary to avoid the influence of fluctuations of the heart position on the body

surface ECG and LECG (Macleod *et al.* 2000). The right hip was used as the recording reference for each subject. The actual recordings were repeated with the active LECG TCE sensor array moved to each of the preplanned locations with a 1.2 cm horizontal spatial sampling resolution on the chest. All the preplanned locations were marked on the chest surface before the recordings began. In the recording sensor array, the distance between two adjacent electrodes' center discs was 3.6 cm, inter-electrode spacing.

The square markers in Figure 3.13 show the first 6 locations recorded. Then the array was translated 1.2 cm horizontally to the circle markers and again to the triangular markers for a total of 18 recording sites. Eighteen more locations (3 row by 6 column) were recorded by moving the sensor array 4.8 cm horizontally to cover the next recording surface with two more translations. Then after recording the surface above the nipple line, the sensor array was moved downward to cover the surface under the nipple line with the same process repeated. The total 6 row by 12 column matrix body surface cardiac LECG signals were recorded for each subject from 72 locations as shown in Figure 3.13. For each location, 30-second recording was repeated 3 times.

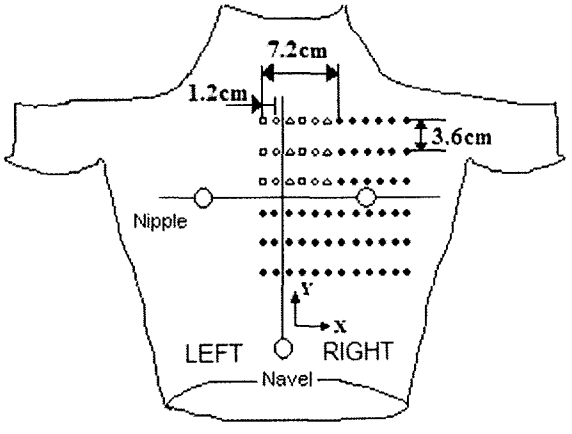

Figure 3.13. The 6 row by 12 column matrix of recording sites over the anterolateral chest, a frontal view. Each dot represents a recording site. Horizontal and vertical

distances between two recording sites are 1.2 and 3.6 cm respectively. The nipple line and sternal midline are references for the recording sites and are represented with dashed lines. The intersection of these two lines was the origin. Right and left from the reader's perspective are used to designate two sides of the sternal midline.

3.2.4 LECG Post-processing

The LECG post-processing was performed offline using Matlab® 6.5. In post-processing, each LECG signal was windowed and synchronized relative to the simultaneously recorded Lead II ECG R-wave peak after baseline-adjustment and QRS detection (Besio and Kota 2004) were performed. Wiener adaptive filtering has been reported to play a positive role in reducing the effect of noise on the LECG estimation (He and Wu 1999, He 1998) and was used in this work as well. The Wiener adaptive filter transfer function is defined in accordance with the power spectrum of the signal and noise process obtained by taking the Fourier transform of the signal and noise autocorrelation (Bertrand *et al.* 1987). Figure 3.14 shows the diagram and transfer function of the Wiener adaptive filter used in this study.

The cardiac signal is characterized by the recurrence of the QRS complex. This recurrence is approximately 800 ms in the healthy human heart. The sampling rate was 2,000 Hz for each recording channel to achieve 1/2 ms resolution. Therefore, a 1600-point window digital Wiener filter was applied to cover one 800 ms cardiac cycle. The transfer function of the Wiener adaptive filter in this study was a formula combining the averaged spectra of all cardiac cycles and the spectra of the averaged cardiac cycle. By performing the convolution between the recorded LECG and the Wiener transfer function, the filtered LECG was obtained. Then the Weiner filtered LECG were ensemble averaged, based on the 800 ms window. Figure 3.15 shows the diagram of the post-processing.

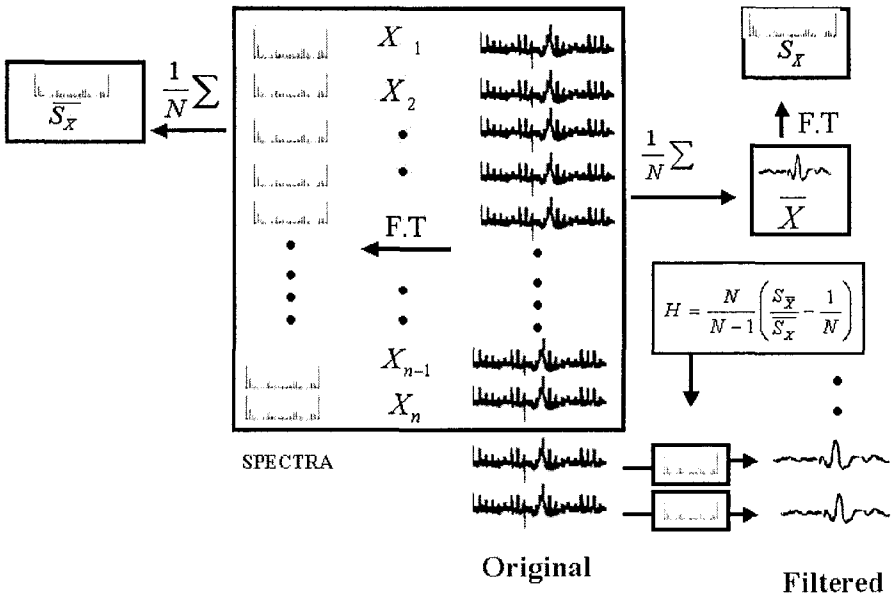

Figure 3.14. The diagram and transfer function of the Wiener adaptive filter (Bertrand et al. 1987).

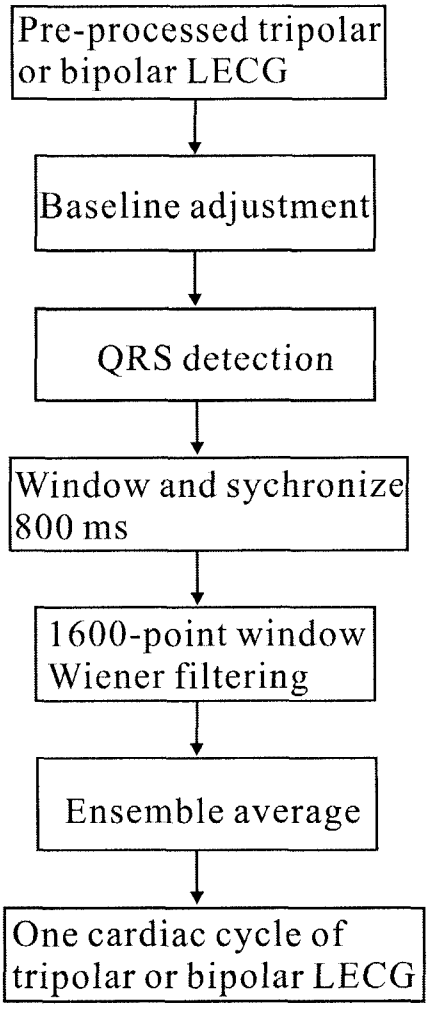

Figure 3.15. The diagram of the post-processing.

3.2.5 LECG MOA Algorithm

The MOA is defined as "the instant the dipole that represents the depolarization wavefront crosses the vector normal to the active sensor's surface" (Besio *et al.* 2001). There is a delay for the depolarization wavefront to propagate over the body surface. The MOA is determined by calculating the time when the dipoles' activation wavefront may be directly below the sensor. A new algorithm for calculating MOA was automated and it achieved greater than 99% efficiency on simulated signals with noise (Besio and Kota 2004). In the new MOA algorithm, the Lead II ECG R-wave peak was used as the time

reference to calculate the time lag. Cross correlation for pattern matching between the LECG and Lead II ECG was used to find the best fit. The time lag between these two similar waves was designated as the MOA with the units in [ms]. The MOA could be zero, which means the LECG wave happens at the same time as the Lead II ECG R-wave peak. A positive MOA, means the LECG wave happens later than the Lead II ECG R-wave peak, and a negative value means the LECG wave happens earlier than the Lead II ECG R-wave peak. Figure 3.16 shows the new MOA algorithm using the paced cardiac signals (Besio and Kota 2004). In Figure 3.16, the first, third and fifth dotted lines crossing the two panels represent the paced Lead II ECG R-wave peak which is used as the time reference. The second, fourth, and sixth dotted lines represent the matched wave peaks of the raw LECG which have the highest cross correlation coefficient with the Lead II ECG R-wave peak. The time lags between the first and second dotted lines, between the third and fourth dotted lines, and between the fifth and sixth dotted lines are designated as MOA.

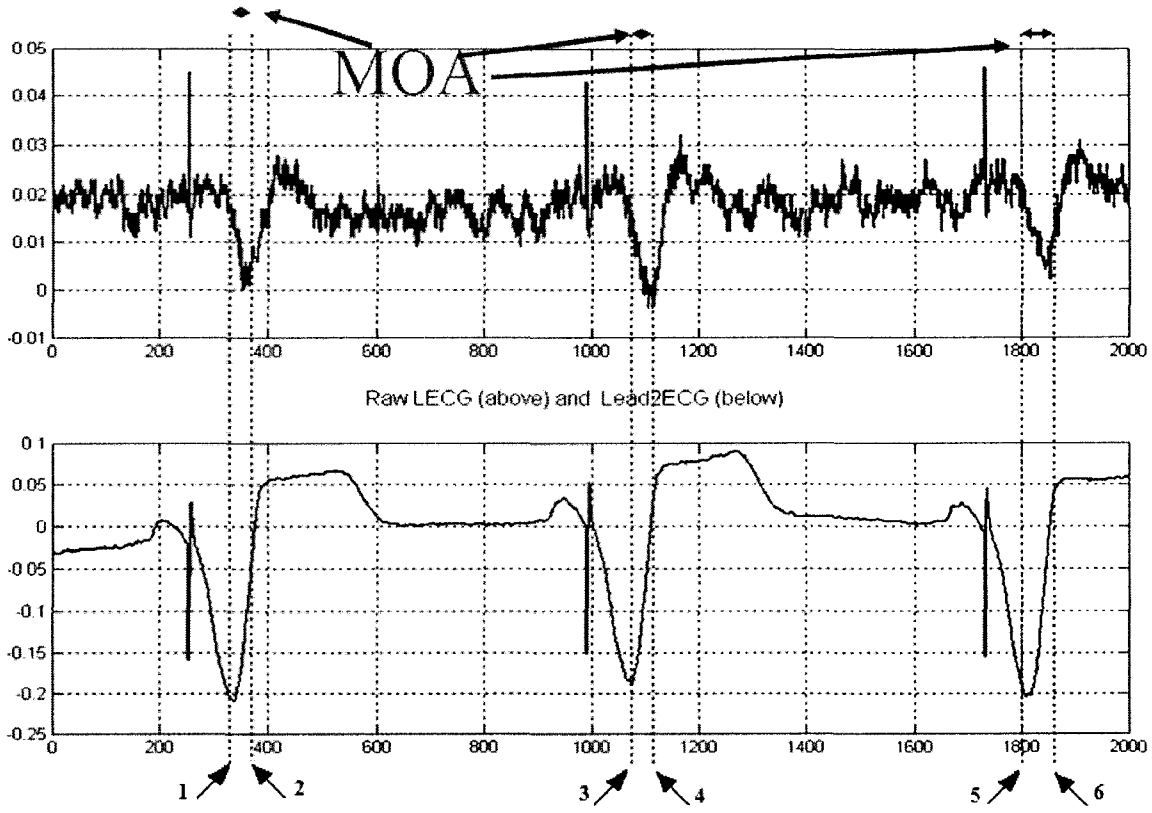

Figure 3.16. The MOA algorithm using the paced cardiac signals (Besio and Kota 2004).

3.2.6 Comparison Parameter Computation

In the present study, correlation coefficient (CC) was used to quantitatively assess the similarity between the tripolar and bipolar LECG. The measures of CC over one 800 ms cardiac cycle are defined as follows (He and Wu 1997):

$$CC = \frac{\sum_i (L_{bipolar,i} - \bar{L}_{bipolar})(L_{tripolar,i} - \bar{L}_{tripolar})}{\sqrt{\left(\sum_i (L_{bipolar,i} - \bar{L}_{bipolar})^2\right)\left(\sum_i (L_{tripolar,i} - \bar{L}_{tripolar})^2\right)}} \tag{3.7}$$

where $\vec{L}_{tripolar}$ and $\vec{L}_{bipolar}$ denote the tripolar and bipolar LECG. $\bar{L}_{tripolar}$ and $\bar{L}_{bipolar}$ denote the mean values of $\vec{L}_{tripolar}$ and $\vec{L}_{bipolar}$, respectively. The number of the recording sites from 1 to 72 is denoted by i.

To compare the spatial selectivity, the descretized Laplacian operator SSy was used. The SSy is calculated as the average of the ratios between the peak-to-peak value differences of the LECG at one recording site among its four neighboring recording sites (twelve o'clock, three o'clock, six o'clock, and nine o'clock around the non-marginal recording site) and the peak-to-peak value of the LECG at that central recording site. For consistency between subjects, the SSy was calculated on an area where the magnitude of the central signal was greater than its four immediate neighbors. For example, $SSy(x_0, y_0)$ was calculated as follows:

$$SSy(x_0,y_0)=\left(\frac{P(x_0,y_0)-P(x_{-1},y_0)}{P(x_0,y_0)}+\frac{P(x_0,y_0)-P(x_{+1},y_0)}{P(x_0,y_0)}\right.$$
$$\left.+\frac{P(x_0,y_0)-P(x_0,y_{-1})}{P(x_0,y_0)}+\frac{P(x_0,y_0)-P(x_0,y_{+1})}{P(x_0,y_0)}\right)/4 \qquad (3.8)$$

where x_0 and y_0 are the LECG coordinates in x and y direction as shown in Figure 3.13. $P(x_0, y_0)$, $P(x_{-1}, y_0)$, $P(x_{+1}, y_0)$, $P(x_0, y_{-1})$ and $P(x_0, y_{+1})$ denote the peak-to-peak values of LECG at location (x_0, y_0) and its four adjacent LECG, respectively (Figure 3.17). When calculating the SSy at (x_0, y_0) using Equation (3.8), a large SSy means there is a stronger signal at (x_0, y_0) compared to its neighboring signals. Higher SSy may improve the ability in differentiating the central signal from its neighboring signals increasing the spatial selectivity.

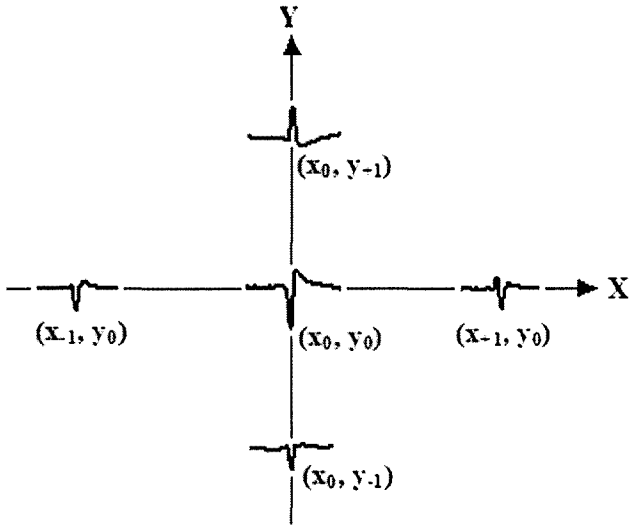

Figure 3.17. Illustration of the calculation of the SSy.

CHAPTER 4

RESULTS

4.1 Computer Simulation

4.1.1 Planar surface Model

Table 4.1 and Figure 4.1 show the RMSE of the three estimated LECG from four different recording electrode arrays. The RMSE for tripolar LECG is always less than the RMSE for the other estimates. The error for the spline LECG decreases as more electrodes are added. When electrodes are increased to 81, the spline LECG has less RMSE than the bipolar LECG. The RMSE for the tripolar and bipolar LECG have a slight variation when more electrodes are used.

Table 4.1. RMSE of the three estimated LECG.

	T[1]	B[2]	S[3]
5 × 5	9.30e-6	2.64e-4	6.10e-4
9 × 9	5.49e-6	1.51e-4	6.62e-5
11 × 11	4.50e-6	1.31e-4	5.04e-5
17 × 17	3.54e-6	1.27e-4	1.41e-5

[1]T=tripolar LECG [2]B=bipolar LECG [3]S=spline LECG

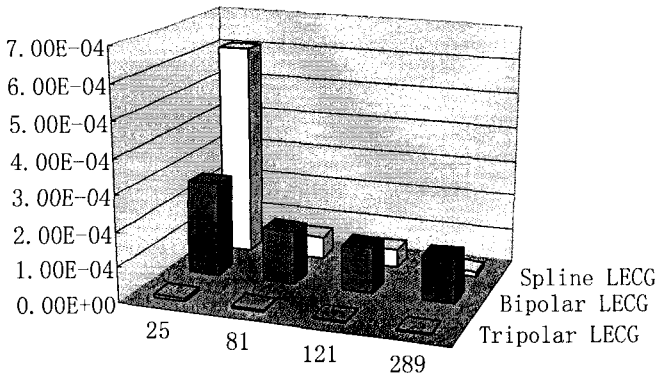

Figure 4.1. RMSE of the three estimated LECG.

In each of the four electrode arrays there were nine recording sites that were common to each (Figure 3.4). Table 4.2 and Figure 4.2 show the RMSE of those nine recording sites between the estimated and analytical LECG. As can be seen, the RMSE for the tripolar and bipolar LECG were constant even as the electrode number increased, while the RMSE for the spline LECG decreased.

Table 4.2. RMSE at the nine common recording sites.

	T	B	S
5×5	1.55e-5	4.38e-4	9.12e-4
9×9	1.55e-5	4.38e-4	1.71e-4
11×11	1.55e-5	4.38e-4	1.60e-4
17×17	1.55e-5	4.38e-4	5.88e-5

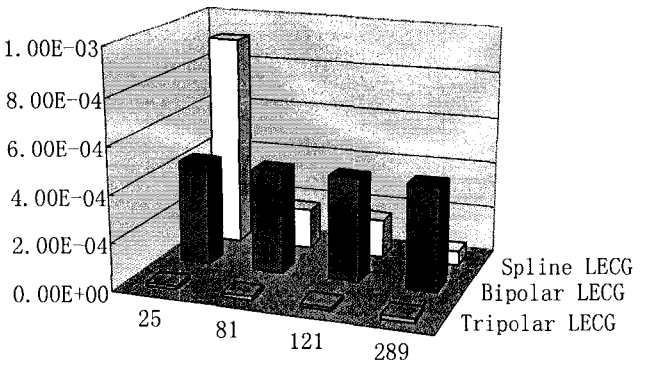

Figure 4.2. RMSE at the nine common recording sites.

4.1.2 Simplified Heart-torso Model

4.1.2.1 Effects of Number of Recording Electrodes

Table 4.3 shows the effects of the number of recording electrodes and the dipole configuration on the torso cylinder surface LECG estimation. Testing number of electrodes to see how the accuracy of the three estimated LECG is affected by the sampling rate, and, if under controlled conditions, fewer electrodes can be used to detect diseased conditions. One or multiple dipoles with varying orientations were included in the spherical heart conductor model representing cardiac electrical sources (described under Table 4.3 and in Figure 4.3). The eccentricities, such as 60%, were used to assess the effect of the source depth inside the heart sphere. For a graphical comparison, the results presented in Table 4.3 are shown in Figure 4.4, the RMSE for the three estimated LECG with each dipole configuration. From Figure 4.4 it can be seen that for each dipole configuration, the RMSE of the tripolar and bipolar LECG did not change significantly as the number of electrodes increased ($p=0.0729$ and $p=0.0702$ between 25 and 289 electrodes for tripolar and bipolar LECG respectively with all dipole configurations).

However, for the spline LECG in general, the more electrodes, the lower the RMSE ($p = 0.0067$ between 25 and 289 electrodes for spline LECG with all dipole configurations). For example, the RMSE decreased from 1.87e-3 with 25 electrodes to 1.86e-4 with 289 electrodes for dipole configuration 1 (C.1). A direct comparison among dipole configurations can not be made from Figure 4.4 since they have different scales.

Table 4.3. RMSE of the three LECG estimators.

Ele No.	25			81			121			289		
	T	B	S	T	B	S	T	B	S	T	B	S
C.1[1]	1.17e-4	5.84e-4	1.87e-3	1.02e-4	5.51e-4	7.08e-4	1.06e-4	5.02e-4	4.04e-4	1.07e-4	4.53e-4	1.86e-4
C.2[2]	1.96e-4	2.17e-3	4.62e-3	1.62e-4	1.44e-3	1.17e-3	1.60e-4	1.19e-3	6.58e-4	1.31e-4	9.60e-4	2.50e-4
C.3[3]	1.41e-4	5.83e-4	1.59e-3	1.19e-4	5.54e-4	6.53e-4	1.20e-4	5.06e-4	3.60e-4	1.23e-4	4.57e-4	1.73e-4
C.4[4]	1.14e-5	1.64e-5	1.58e-4	1.12e-5	1.44e-5	8.47e-5	1.16e-5	1.49e-5	7.20e-5	1.16e-5	1.48e-5	5.15e-5
C.5[5]	2.48e-4	1.88e-3	4.47e-3	1.81e-4	1.70e-3	1.78e-3	1.73e-4	1.40e-3	9.94e-4	1.35e-4	1.15e-3	4.21e-4
C.6[6]	3.73e-6	5.38e-6	4.05e-5	3.27e-6	3.99e-6	1.73e-5	3.31e-6	4.06e-6	1.40e-5	3.31e-6	3.93e-6	9.57e-6
C.7[7]	1.36e-4	6.00e-4	3.98e-3	1.43e-4	7.39e-4	1.43e-3	1.41e-4	6.80e-4	8.36e-4	1.45e-4	6.51e-4	4.92e-4

[1]C.1: dipole configuration 1 (Figure 4.3 C.1), one radial dipole located at an eccentricity of 60% within the heart sphere, representing one localized wavefront propagating from the endocardium to the epicardium on the anterior wall of the heart, (-1.5, 2.6, 0).

[2]C.2: dipole configuration 2 (Figure 4.3 C.2), one tangential dipole located at an eccentricity of 80% within the heart sphere, representing an ectopic myocardial activity on the anterior wall of the heart, (-0.69, 3.94, 0).

[3]C.3: dipole configuration 3 (Figure 4.3 C.3), two radial dipoles located at an eccentricity of 60% within the heart sphere with an angle of 60° between them, representing two localized wavefronts propagating from the endocardium to the epicardium on the anterior wall of the heart, (±1.5, 2.6, 0).

[4]C.4: dipole configuration 4 (Figure 4.3 C.4), two radial dipoles located at an eccentricity of 60% within the heart sphere with an angle of

60° between them, representing two localized wavefronts propagating from the endocardium to the epicardium on the posterior wall of the heart, (±1.5, -2.6, 0).

[5]C.5: dipole configuration 5 (Figure 4.3 C.5), two tangential dipoles located at an eccentricity of 80% within the heart sphere with a separating angle of 20° between them representing an ectopic myocardial activity on the anterior wall of the heart, (±0.69, 3.94, 0).

[6]C.6: dipole configuration 6 (Figure 4.3 C.6), two tangential dipoles located at an eccentricity of 60% within the heart sphere with a separating angle of 20° between them representing an ectopic myocardial activity on the posterior wall of the heart, (±0.52, -2.95, 0).

[7]C.7: dipole configuration 7 (Figure 4.3 C.7), two pairs of tangential dipoles located in the anterior wall of the heart. Each pair of the tangential dipoles are located at an eccentricity of 60% of the heart sphere with a separating angle of 10°, representing an ectopic myocardial activity on the anterior wall of the heart. The angle between the centers of the two pairs of dipoles is 45°, (±0.9, 2.86, 0) and (±1.39, 2.66, 0).

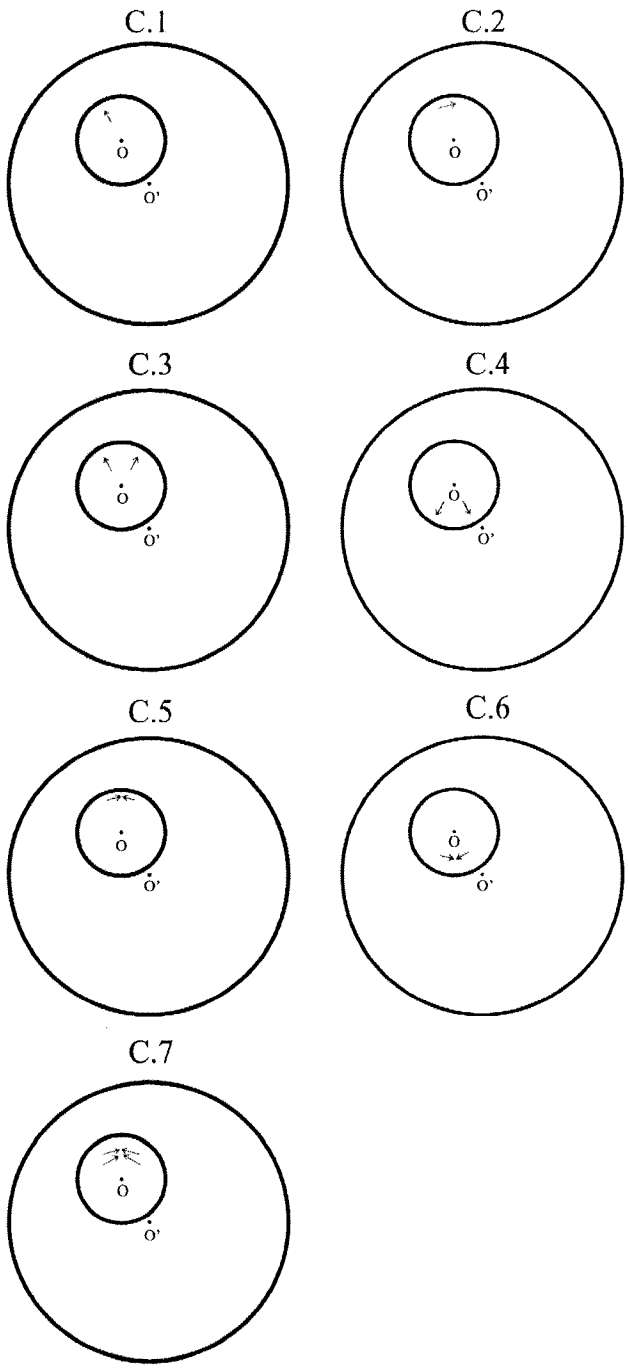

Figure 4.3. Dipole configurations 1 ~ 7 (C.1 ~ C.7) representing cardiac electrical sources.

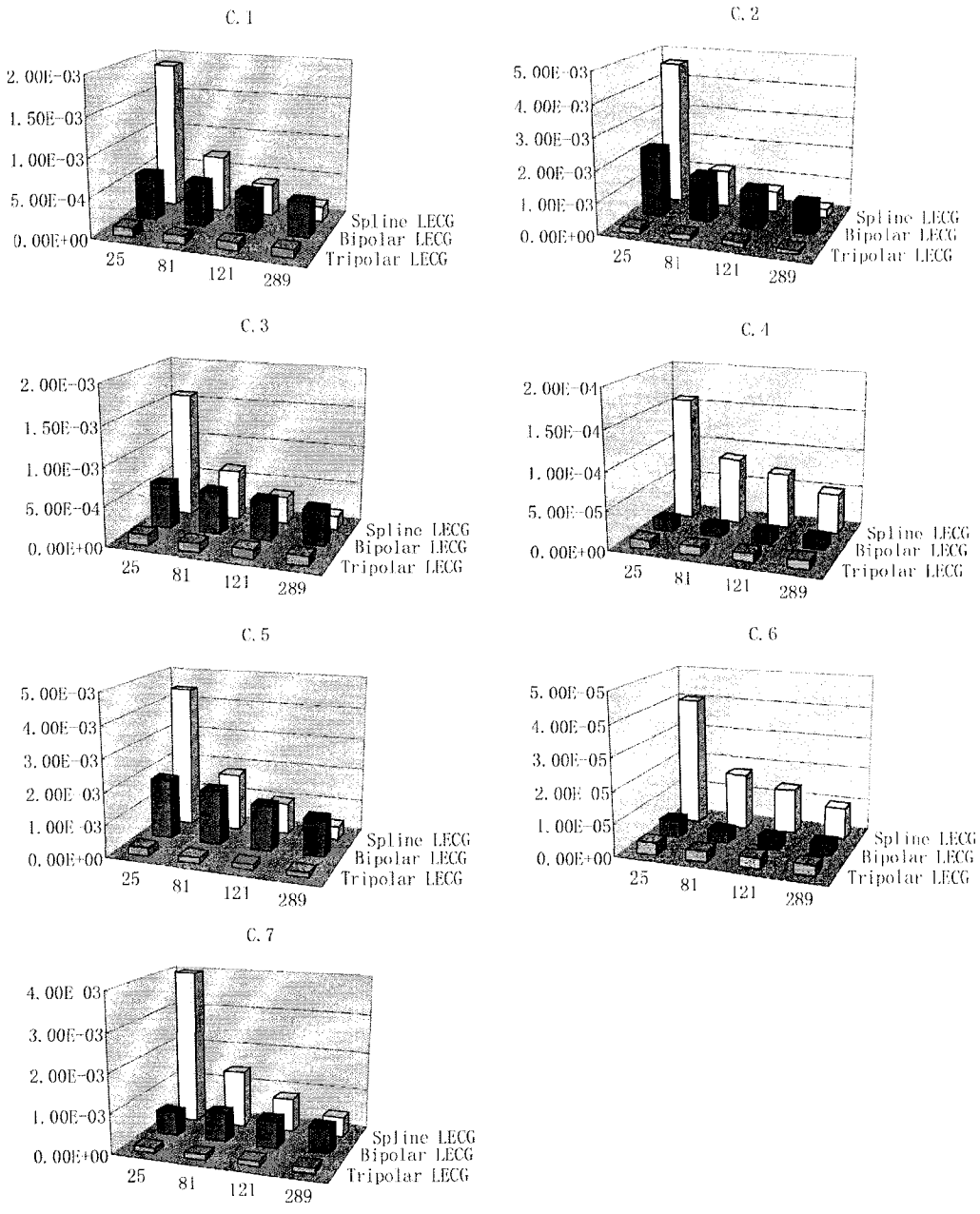

Figure 4.4. RMSE for the three estimated LECG with each dipole configuration. C.1 ~ C.7 represent dipole configures 1 ~ 7.

For all seven dipole configurations and each electrode array, the tripolar LECG always showed the lowest RMSE among the three estimated LECG. The RMSE between the tripolar LECG and the bipolar or spline LECG are significantly different (p=4.74e-6

between the tripolar and bipolar LECG, and p=5.48e-4 between the tripolar and spline LECG). The bipolar LECG had lower RMSE compared with the spline LECG when 25 or 81 electrodes were used for all dipole configurations except for dipole configuration 2 (C.2) with 81 electrodes. However, when using 121 or 289 electrodes, the spline LECG was closer to the analytical LECG than the bipolar LECG with lower RMSE for dipole configurations 1, 2, 3, and 5 (C.1, C.2, C.3 and C.5). For dipole configuration 7 (C.7), the spline LECG had better performance than the bipolar LECG only when the electrodes were increased to 289. Note that the RMSE of the tripolar LECG with 25 electrodes (Figure 4.5 and Table 4.3) is significantly lower than the RMSE of the bipolar or spline LECG with 121 or 289 electrodes for all dipole configurations (p=0.0134 and p=0.0108 for bipolar, and p=0.00912 and p=0.0331 for spline).

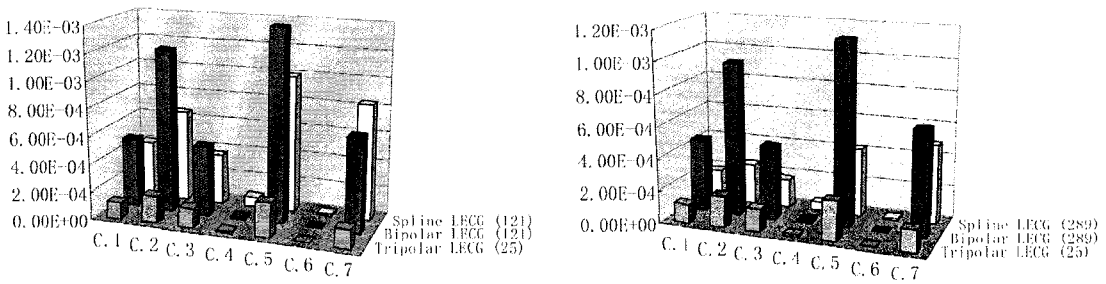

Figure 4.5. RMSE for the tripolar LECG with 25 electrodes and the bipolar and spline LECG with 121 and 289 electrodes.

4.1.2.2 Estimated and Analytical BSLM

The tripolar, bipolar, spline and analytical LECG on the torso cylinder surface were used to generate BSLMs. Figure 4.6 shows the normalized tripolar (a), bipolar (b), spline (c) and analytical (d) BSLMs on the anteriolateral torso cylinder surface corresponding to dipole configuration 1 (C.1), with 289 recording electrodes. The

abscissa and ordinate represent the columns and rows of the electrode array, respectively. The scale shows the normalized LECG magnitude in units of [mV cm^{-2}]. The shade towards white designates the positive magnitude and the shade towards black represents the negative magnitude. In Figures 4.6 through 4.15, the same settings are followed for the graphs as in Figure 4.6. Figures 4.7 to 4.12 show BSLMs corresponding to dipole configuration 2 ~ 7 (C.2 ~ C.7) and 289 recording electrodes. In Figure 4.6, the three estimated BSLM show similar sensitivity to the radial source dipole. In Figure 4.7, both poles of the tangential source dipole are evident in the three estimated BSLMs. However, the spline BSLM shows more fluctuations at the left side compared to the other two estimated BSLMs. Two radial source dipoles can not be differentiated for any estimated LECG or the analytical LECG in Figure 4.8 since they were too close to each other. In Figure 4.8, only one enhanced positive pole (white area) and one negative pole (tail) are shown in each BSLM. Due to the deeper location of the source dipoles, in Figure 4.9 there still is no differentiation of the two radial source dipoles. Only one negative pole (black area) is shown in each BSLM. There is more smearing on the boundary for spline BSLM. In Figure 4.10, the two tangential radial dipoles can not be differentiated either. Only one enhanced positive pole (white area) and one negative tail, which is mainly due to one tangential source dipole, are shown. Spline BSLM shows more smearing. Due to the deeper location of the source dipoles in Figure 4.11, the negative pole (black area) migrates to the right side of each BSLM. The extended positive pole (white tail) crosses the whole recording area. Spline BSLM shows more smearing compared to the other two estimated BSLMs. In Figure 4.12, the four source dipoles are not fully separated. Only one enhanced positive pole (white area), which is due to four tangential source dipoles

and one enhanced negative pole (black area) which is mainly due to two tangential source dipoles, are shown. Figures 4.6 to 4.12 visually indicate that, from the viewpoint of the mapping, the tripolar BSLM is very similar to the analytical BSLM. The spline BSLM shows more fluctuations at the boundaries compared to the other two estimated BSLMs.

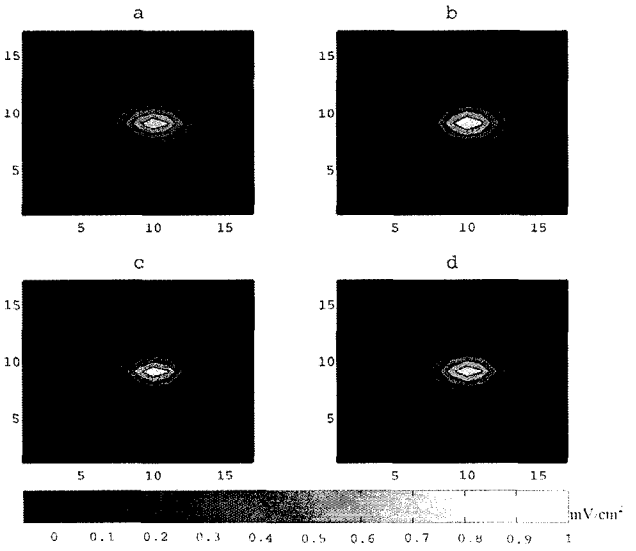

Figure 4.6. The normalized tripolar (a), bipolar (b), spline (c) and analytical (d) BSLMs on the anteriolateral torso cylinder surface corresponding to dipole configuration 1 (C.1) with 289 recording electrodes.

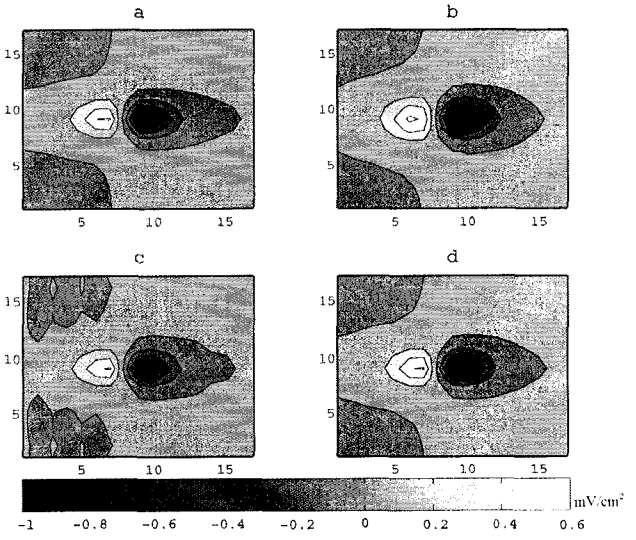

Figure 4.7. The BSLMs of 289 recording electrodes and dipole configuration 2 (C.2).

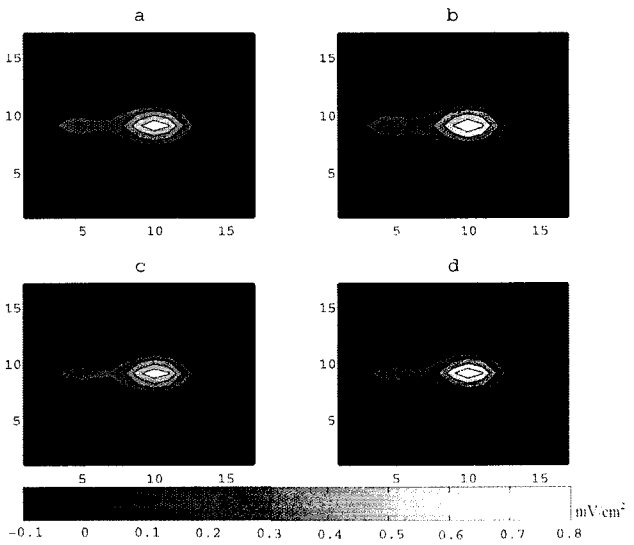

Figure 4.8. The BSLMs of 289 recording electrodes and dipole configuration 3 (C.3).

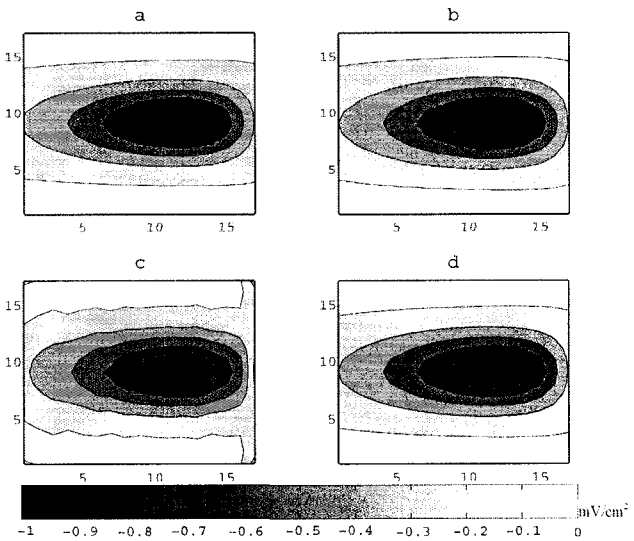

Figure 4.9. The BSLMs of 289 recording electrodes and dipole configuration 4 (C.4).

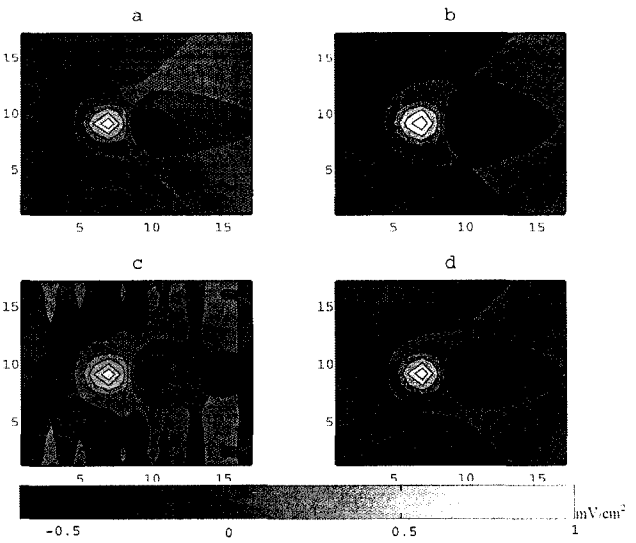

Figure 4.10. The BSLMs of 289 recording electrodes and dipole configuration 5 (C.5).

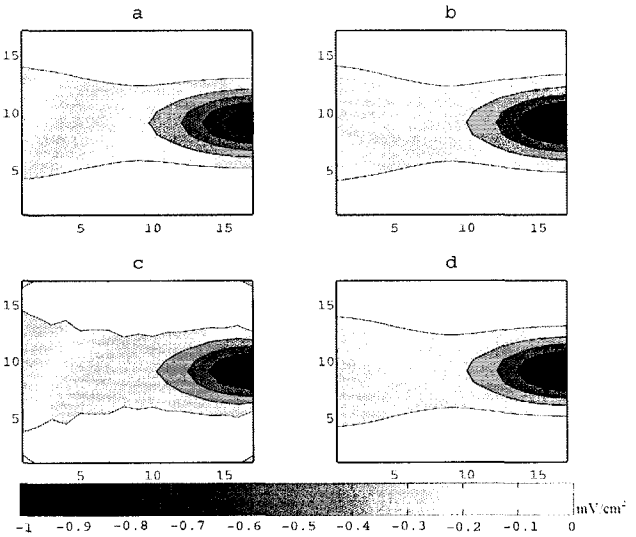

Figure 4.11. The BSLMs of 289 recording electrodes and dipole configuration 6 (C.6).

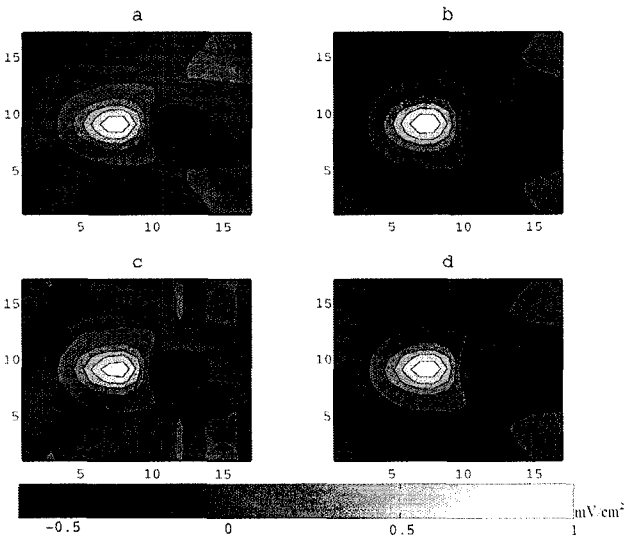

Figure 4.12. The BSLMs of 289 recording electrodes and dipole configuration 7 (C.7).

4.1.2.3 Effects of PN

Figure 4.13A shows the three normalized estimated and analytical BSLMs on the anteriolateral torso cylinder surface corresponding to dipole configuration 1 (C.1) with one randomly activated tangential noise dipole located at (2, 3, 0) as the PN, which had a 25% PN level. There were 289 electrodes used. Figure 4.13B shows the RMSE of the three estimated LECG for the same dipole configuration 1 (C.1) and one tangential PN dipole at levels from 0% to 25% and 289 electrodes. The abscissa represents the PN level from 0% to 25% which is shown from 0 to 0.25. The ordinate represents the RMSE of the three estimated LECG under different PN levels. Figure 4.14 shows the same process as used in Figure 4.13 only corresponding to dipole configuration 3 (C.3), four randomly activated noise dipoles (two radial at (2, -2, 0) and (-4, -1, 0), and two tangential at (±0.52, 1, 0)). Notice that in both cases (Figures 4.13 and 4.14) the RMSE of the tripolar LECG are less than those of the bipolar and spline LECG of all PN levels. The RMSE of the tripolar LECG with 15% (which corresponds to 0.15 on the abscissa in the figures) PN is

comparable to the RMSE of the bipolar and spline LECG under 3% and 10% (which corresponds to 0.03 and 0.10 on the abscissa in the figures) PN, respectively.

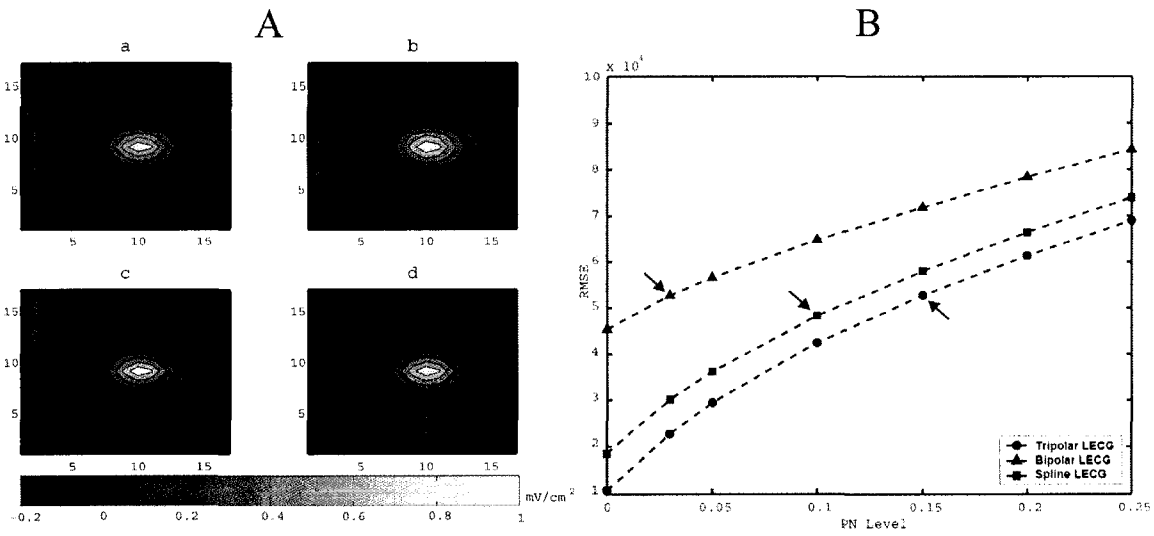

Figure 4.13. A. The tripolar (a), bipolar (b), spline (c) and analytical (d) BSLMs using 289 electrodes corresponding to the dipole configuration 1 (C.1) with one randomly activated tangential noise dipole, which has a 25% PN level. B. RMSE of the tripolar (circle), bipolar (triangle) and spline (square) LECG with PN levels from 0% to 25%.

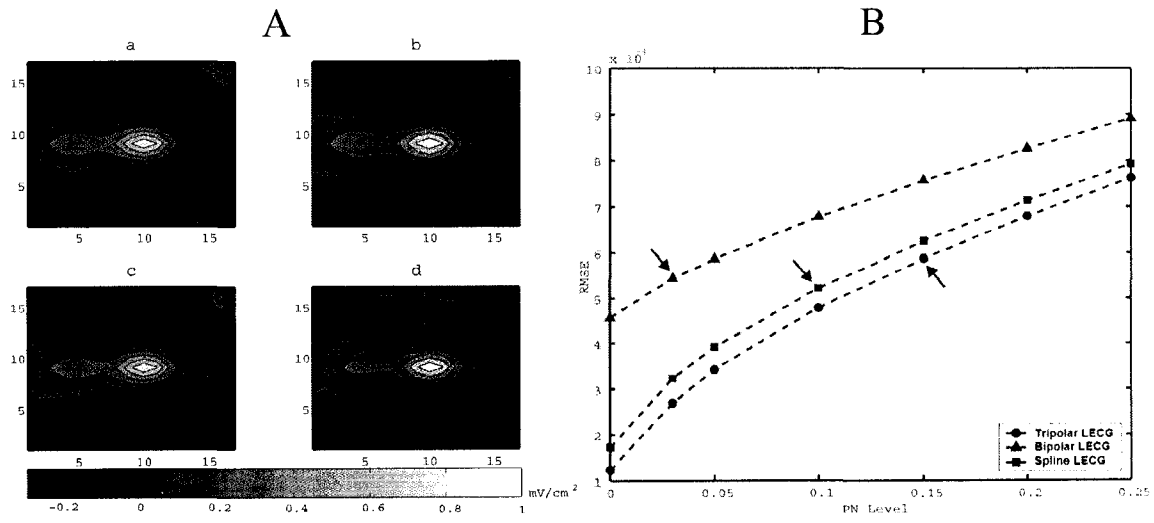

Figure 4.14. BSLMs and RMSE for dipole configuration 3 (C.3) with four randomly activated noise dipoles (two radial and two tangential).

4.1.2.4 Spatial Resolution

Figure 4.15A depicts a set of graphs used to determine the spatial resolution of the three estimated LECG using 289 electrodes on the torso surface. The plots (a), (b), (c), and (d) correspond to the varying dipoles' distance of 6, 7, 8, and 9 cm, respectively. The solid, dashed, and dotted lines in each plot represent the tripolar, bipolar, and spline LECG, respectively. The abscissa refers to the distance along a line on the torso surface overlying the dipoles in [cm]. The ordinate refers to the normalized magnitude of the estimated LECG with units of [mV cm^{-2}]. The two peaks in the plots (a), (b), (c), and (d) correspond to the two dipoles which are perpendicular to the torso cylinder surface. Figure 4.15B (a), (b), and (c) show the three normalized estimated BSLMs, and (d) shows the analytical BSLM with the distance between the two dipoles of 7 cm which corresponds to the data of Figure 4.15A (b). The dashed lines in Figure 4.15B indicate the positions where the plots of Figure 4.15A are from, namely the central column of the electrode array which is indicated by the solid arrow lines on the torso cylinder surface in Figure 3.5. The RMSE values of the tripolar, bipolar, and spline BSLMs are 8.91e-6, 1.10e-5, and 4.45e-5, respectively.

From Figure 4.15, it can be seen that while the distance between the two dipoles varied from 6 cm to 9 cm, the three estimated LECG all showed abilities in distinguishing and localizing multiple sources from the torso surface. In Figure 4.15A, the longer the separating distance between two radial dipoles, the deeper the valley between the two peaks, which represents the capability of the LECG to identify multiple sources. However, with each separating distance, the three estimated LECG do not show the same valley depth. The tripolar LECG always shows the deepest valley between the two peaks. The bipolar LECG always shows the highest valley compared to the other two estimated

LECG. This feature may also be seen visually in Figure 4.15B. The tripolar BSLM shows the two maxima corresponding to the two dipoles much more clearly compared to the bipolar BSLM. While the spline BSLM also shows the two maxima, it has more RMSE (distortion) than the tripolar and bipolar BSLM. The SC values are shown in Table 4.4 to demonstrate the difference between the three estimated LECG. The higher the SC, the better the separation.

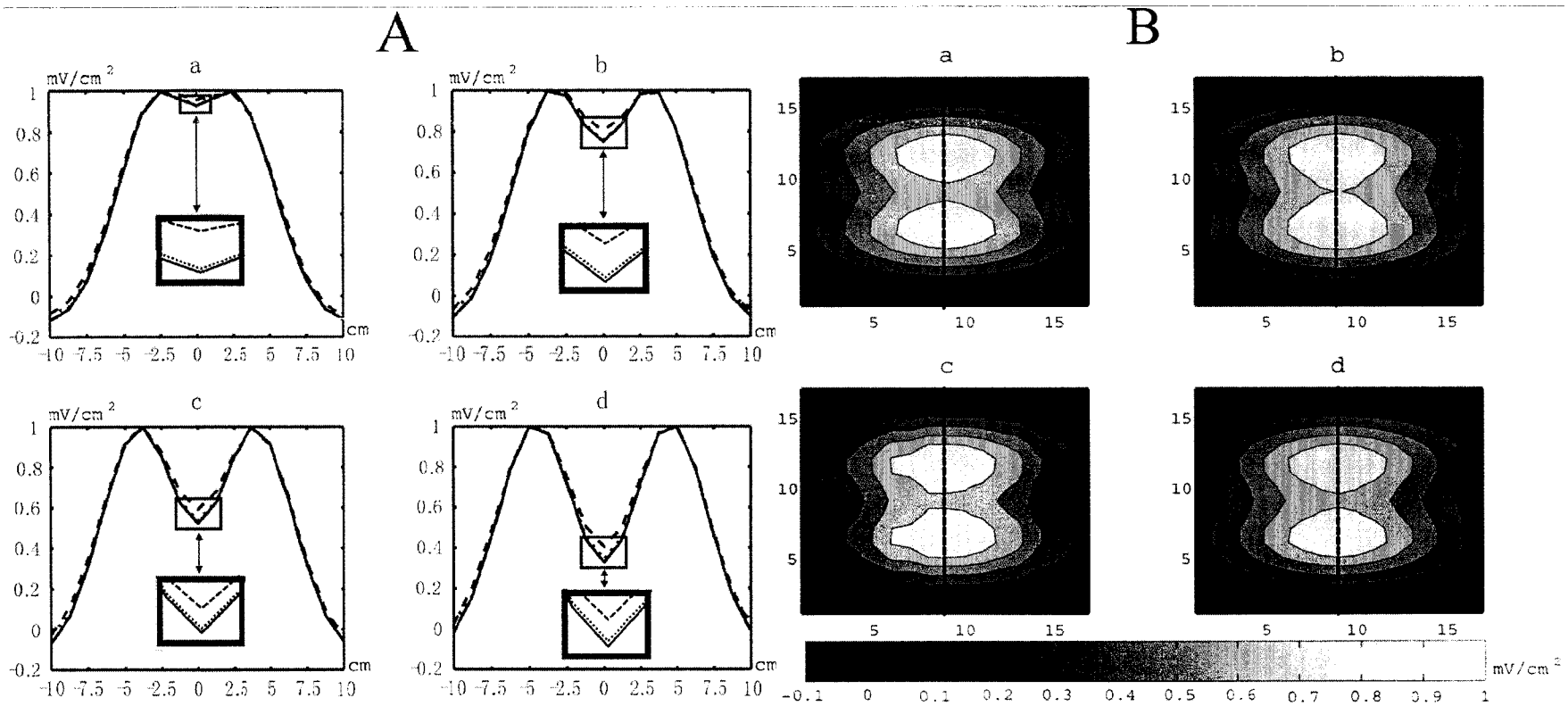

Figure 4.15. A. Normalized distributions of the three estimated LECG using 289 electrodes on the torso surface generated by two dipoles oriented perpendicular to the torso surface, which were located at the same depth of 10 cm from the surface with separation distances of 6 cm (a), 7 cm (b), 8 cm (c), and 9 cm (d). The tripolar, bipolar, and spline LECG were represented by solid, dashed, dotted lines respectively. B. Normalized estimated and analytical BSLMs when the distance between the two dipoles was 7 cm.

Table 4.4. SC of the three estimated LECG with varying dipole separation.

	6 cm	7 cm	8 cm	9 cm
Tripolar LECG	0.0294	0.0666	0.1275	0.1346
Bipolar LECG	0.0179	0.0521	0.1090	0.1192
Spline LECG	0.0284	0.0649	0.1243	0.1313

4.2 Human Experiment

4.2.1 Recorded Cardiac Signals

The 13 channels of cardiac signals were recorded simultaneously and digitally stored for all six subjects for the signal pre-processing and post-processing. Channels 1 ~ 12 recorded the bipolar potential differences between the concentric rings and center disc of the six active LECG TCE sensor array. The odd channels were the bipolar potential differences between the outer ring and center disc. The even channels were the bipolar potential differences between the inner ring and center disc. Channel 13 recorded the Lead II ECG which was used as the time reference. Figure 4.16 shows the cardiac signals recorded from one of our subjects. Channels 1 and 2, Channels 3 and 4, Channels 5 and 6, Channels 7 and 8, Channels 9 and 10, and Channels 11 and 12 recorded the bipolar potential differences at locations (-1.8, 9), (1.8, 9), (-1.8, 5.4), (1.8, 5.4), (-1.8, 1.8), and (1.8, 1.8), respectively, which correspond to the red dots in Figure 3.13. The recorded cardiac signals were pre-processed to get the tripolar and bipolar LECG based on Equations (2.12) and (2.17) and then post-processed to get one cardiac activation cycle of the tirpolar and bipolar LECG.

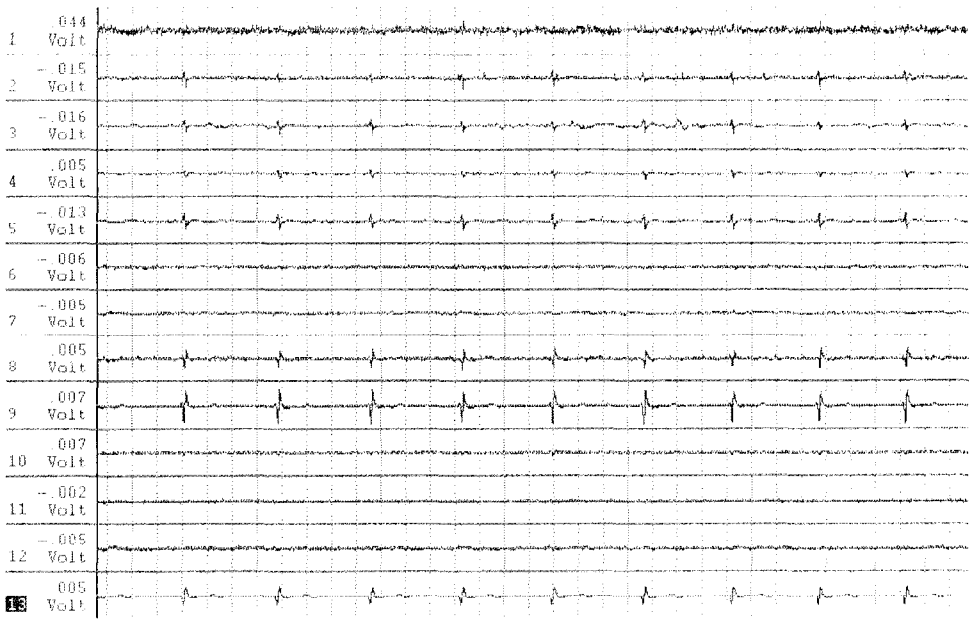

Figure 4.16. Recorded cardiac signals on the data acquisition system.

4.2.2 Tripolar LECG Waves

Figure 4.17 Panels A, B, and C show three examples of one cardiac activation cycle of post-processed tripolar LECG acquired at different recording locations from a subject (No. 4), which were the typical waveforms in all six subjects. Panel D is the relative Lead II ECG. The LECG in Panel A is a monophasic negative wave that has a strong downward pulse and a weak upward pulse. Similarly, the LECG in Panel B is a monophasic positive wave that has a strong upward pulse and a weak downward pulse. The LECG in Panel C is a biphasic (doublet) wave that has a strong positive/negative pulse followed by a strong negative/positive pulse.

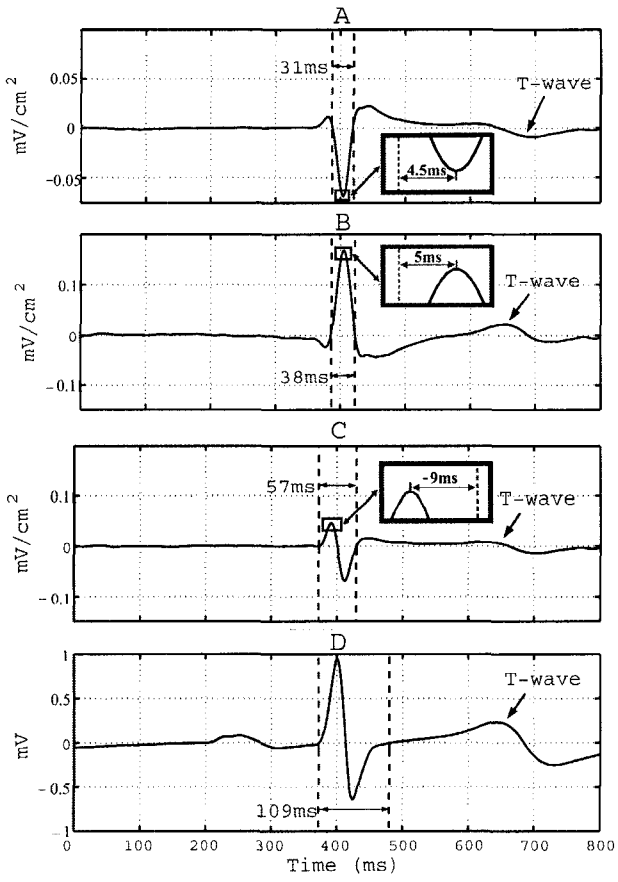

Figure 4.17. Tripolar LECG: Panel A (monophasic negative), B (monophasic positive) and C (biphasic / doublet), Panel D is the relative Lead II ECG recorded simultaneously. The abscissa designates the time in 100 ms increments. The ordinate designates the magnitude of the waveform with the units in [mV cm^{-2}] for LECG and [mV] for Lead II ECG. T-waves are marked in the figure.

In Figure 4.17, the durations of the QRS waves are indicated between two dashed lines in each panel. For consistency, the first zero crossing before and after the peak determined the start and end of each QRS wave. It can be seen that the duration of the LECG QRS waves were shorter than that of the Lead II ECG. Panels A, B and C show the duration of the LECG QRS wave as 31 ms, 38 ms and 57 ms, respectively. The duration of the Lead II ECG QRS wave was 109 ms. For all six subjects, the ranges of the duration of the LECG QRS waves were: monophasic negative 24 ms to 43 ms (35 ± 6.90 ms), monophasic positive 22 ms to 46 ms (36.17 ± 8.26 ms), and biphasic 47 ms to 65 ms

(57 ± 6.48 ms). For the Lead II ECG QRS waves, the range of duration was between 97 ms and 117 ms (108.67 ± 6.83 ms). Panels A, B, and C reflect that the T-wave which represents ventricular repolarization can be seen clearly with different polarities in the LECG.

In Figure 4.17, the MOA are also shown for the LECG in Panels A, B, and C. As a reference for calculating MOA, the R-wave peak of Lead II ECG was set to the position corresponding to 400 ms. The MOA algorithm performed the pattern matching by using the cross correlation to find the highest correlated LECG wave corresponding to the Lead II ECG R-wave peak. Then the MOA was designated as the time difference between the position of the highest correlated LECG wave and 400 ms. In Figure 4.17, the MOA was 4.5 ms, 5.0 ms, and -9.0 ms for LECG in Panels A, B, and C, respectively. Notice that in Panels A and B the MOA are positive values which mean the LECG reached the body surface recording sites later than the time reference, namely the Lead II ECG R-wave peak. While the MOA in Panel C is a negative value which means the LECG reached the body surface recording site earlier than the time reference.

4.2.3 Comparison of Tripolar and Bipolar LECG

Both tripolar and bipolar LECG were recorded simultaneously. Figure 4.18 shows one averaged cardiac activation cycle of the LECG recorded from the anterolateral chest surface of the same subject's (No. 4) signals. Panel A and Panel B represent tripolar and bipolar LECG, respectively. The LECG waveforms are shown in a 6 row by 12 column topology with respect to the recording sites of Figure 3.13.

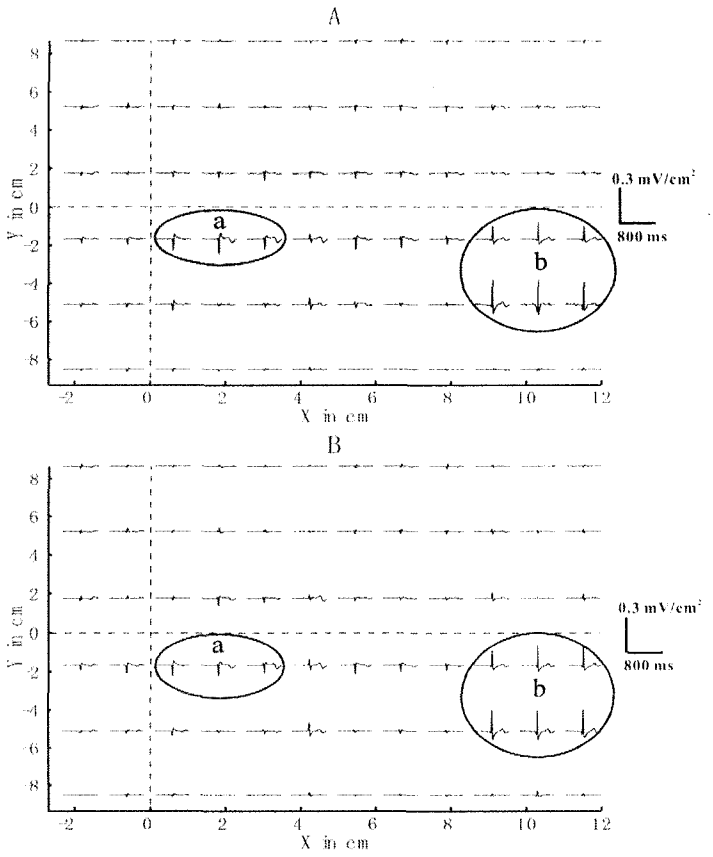

Figure 4.18. One averaged cardiac activation cycle of LECG in a 6 row by 12 column topology recorded from the anterolateral chest of subject No. 4. Panel A and Panel B represent tripolar and bipolar LECG respectively. The abscissa and ordinate designate the recording location over the chest measured in [cm]. The two dashed lines correspond to the nipple line and sternal midline.

The LECG presented in Figure 4.17, Panels A, B, and C are represented in Figure 4.18 at locations (3, 1.8), (11.4, -1.8), and (7.8, -1.8), respectively. Note that the LECG obtained from the tripolar (Figure 4.18 Panel A) and the bipolar (Figure 4.18 Panel B) electrodes exhibited similar morphology, polarity, and magnitude sequence over the whole area of the chest. Table 4.5 shows the CC between the tripolar and bipolar LECG for all six subjects as a measure of similarity. Observing Figure 4.18, strong negative waves (area "a") were shown in both tripolar and bipolar presentations, mainly around the center right side of the sternal midline, namely the subject's left 3rd and 4th rib area.

Strong positive waves (area "b") were discovered in the lower right area, which is actually the subject's left lateral false rib area.

Table 4.5. CC[a] between tripolar and bipolar LECG.

Subject No.	Age	Mean	SD[b]	Min	Max
1	20	0.930	0.098	0.607	1.000
2	25	0.920	0.082	0.638	0.999
3	21	0.899	0.094	0.655	0.999
4	23	0.910	0.099	0.656	0.998
5	23	0.899	0.095	0.660	0.998
6	24	0.916	0.078	0.616	0.999
Mean	22.67	0.912	0.091	0.639	0.999

[a]CC=correlation coefficient. [b]SD=standard deviation.

Table 4.6 presents the SSy of the tripolar and bipolar LECG compared over the central signal in area "a" in all six subjects. Due to anatomic variations, for each subject the area "a" which showed strong negative waves over the central chest was located at slightly different positions. Therefore, Table 4.6 does not show the SSy at the same location in all six subjects. For example, for subject No. 4 (Figure 4.18), SSy(1.8, -1.8) of the tripolar and bipolar LECG were shown in Table 4.6. However, SSy(1.8, 1.8) was described for subject No. 3 since that location is where the strong negative signals were seen. A one-tail paired two-sample t-Test showed the SSy for tripolar to be significantly better than for bipolar LECG ($p=0.0009$).

Table 4.6. SSy of the tripolar and bipolar LECG over the area "a" in all six subjects.

Subject No.	SSy(x_0, y_0)	Tripolar	Bipolar
1	SSy(3, 1.8)	0.573	0.344
2	SSy(1.8, 1.8)	0.782	0.491
3	SSy(1.8, 1.8)	0.615	0.539
4	SSy(1.8, -1.8)	0.542	0.362
5	SSy(1.8, 1.8)	0.813	0.511
6	SSy(3, 1.8)	0.720	0.547

Consistent LECG morphology was discovered in all subjects with a few variations in location and magnitude of the waveforms. For example, area "a" and area "b" were both present in all 6 subjects. Figure 4.19 presents tripolar and bipolar LECG from subject No. 3. Similar as in Figure 4.18, in Figure 4.19 there were strong negative waves (area "a") around the center right side of the sternal midline in both tripolar and bipolar presentations. Strong positive waves (area "b") were shown in the lower right area. In comparing Figures 4.18 and 4.19, there were slight differences in the location and peak-to-peak value of area "a" and "b". For example, area "a" was just below the nipple line in Figure 4.18. However, in Figure 4.19, it appears to have moved vertically one row upward, which was just above the nipple line. For area "b", the signals in the 4^{th} row of Figure 4.19 were much larger than the signals in the 5^{th} row. In Figure 4.18, the same two rows had nearly the same peak-to-peak values.

Another set of trioplar and bipolar LECG from subject No. 1 are presented in Figure 4.20. For subject No. 1, area "a" moved even further compared to subject No. 4 (Figure 4.18). Area "a" in Figure 4.20 was located at the same row as the one in Figure

4.19 (subject No. 3) but one column closer to the left lateral chest compared to subject No. 3. Area "b" in Figure 4.20 had similar performance with the one in Figure 4.19. All these minor alterations could result from the effects of the variations in the heart position and conductivities in each subject (Macleod *et al.* 2000).

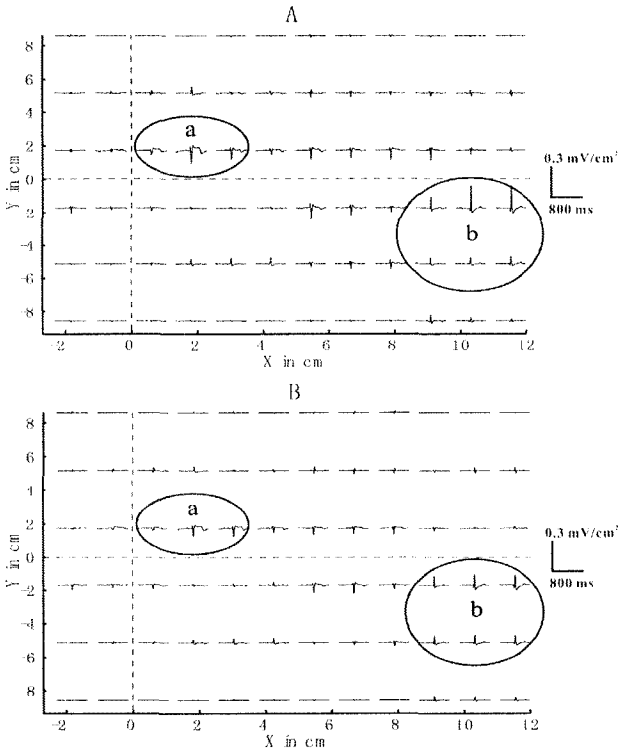

Figure 4.19. One averaged cardiac activation cycle of LECG as in Figure 4.18 only for subject No. 3: tripolar (Panel A) and bipolar (Panel B) LECG.

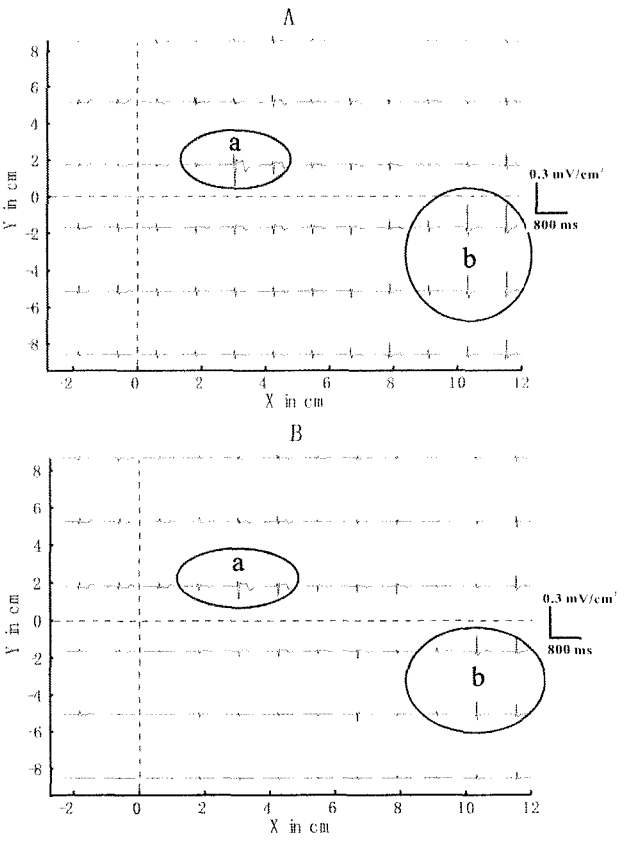

Figure 4.20. One averaged cardiac activation cycle of LECG as in Figure 4.18 only for subject No. 1: tripolar (Panel A) and bipolar (Panel B) LECG.

4.2.4 BSLM

Tripolar BSLM was performed for each subject at the time instant of the Lead II ECG R-wave peak using Matlab® 6.5. Multiple localized positive and negative activities were revealed for all 6 subjects. Figure 4.21 shows the tripolar BSLM from subject No. 4. The physical unit of the scale in the BSLM is in [mV cm^{-2}]. In this map there are three positive activities denoted by P1, P2, and P3 and two negative activities denoted by N1 and N2.

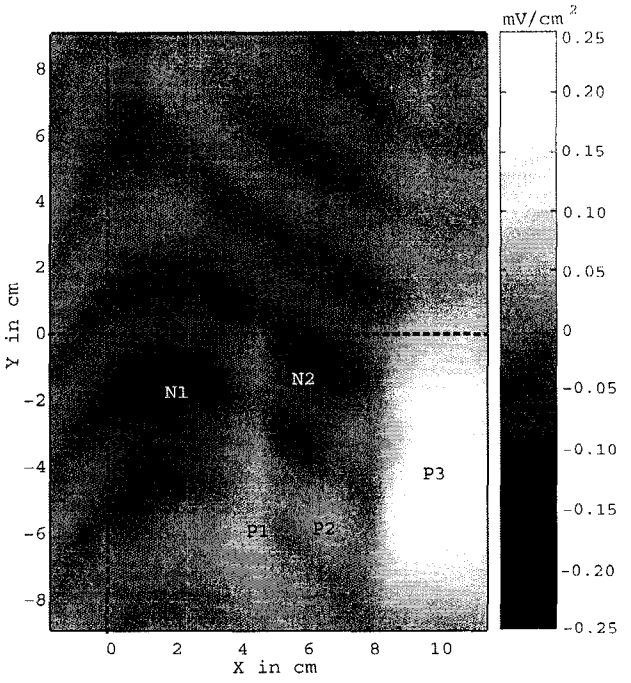

Figure 4.21. Tripolar BSLM from subject No. 4. P1, P2, and P3 denote three positive activities. N1 and N2 denote two negative activities. The abscissa and ordinate (x, y) in [cm] designate the position of the BSLM over the chest. The two dashed lines correspond to the nipple line and sternal midline. The scale on the right side denotes the magnitude of the LECG with the units in [mV cm^{-2}].

Figure 4.22 shows the tripolar BSLM from subject No. 3. Similar to Figure 4.21, N1, N2 and P3 were all present in Figure 4.22 but with slight variance in location and encompassing area. In Figure 4.21, N1 and N2 were just below the nipple line. However, in Figure 4.22, N1 and N2 were just above the nipple line. N2 encompassed more area for subject No. 3 than for subject No. 4. The deeper shade of these three activities compared to the ones in Figure 4.21 indicates that the peak-to-peak magnitudes of these three activities were higher for subject No. 3 than for subject No. 4. For subject No. 3 only P1 was shown around the left central inferior chest with larger encompassing area compared to subject No. 4. P2 was not present in Figure 4.22.

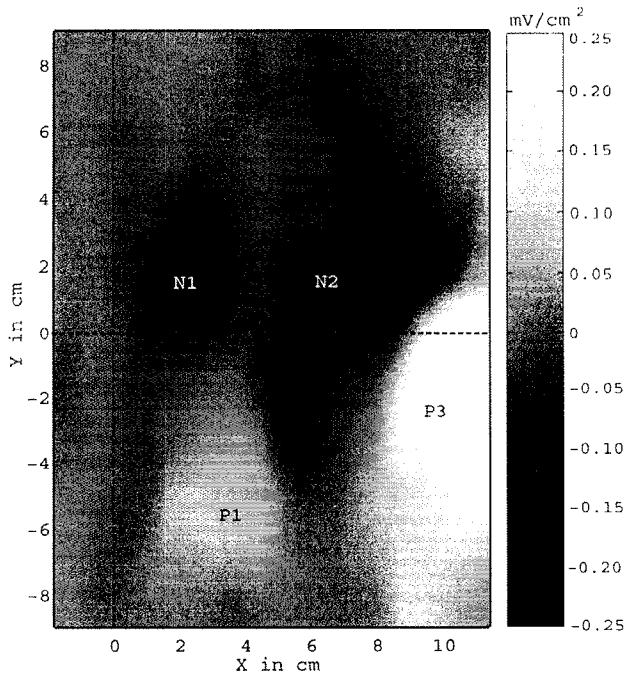

Figure 4.22. Tripolar BSLM from subject No. 3.

Another example of the tripolar BSLM is shown for subject No. 1 in Figure 4.23. Similar to subjects No. 4 and 3, subject No. 1 showed N1, N2 and P3 simultaneously in the tripolar BSLM. Compared to subject No. 3, N1 and N2 were located at the same height but more to the left. Instead of showing P1 for subject No. 3, only P2, which was close to P3, was indicated in the tripolar BSLM for subject No. 1.

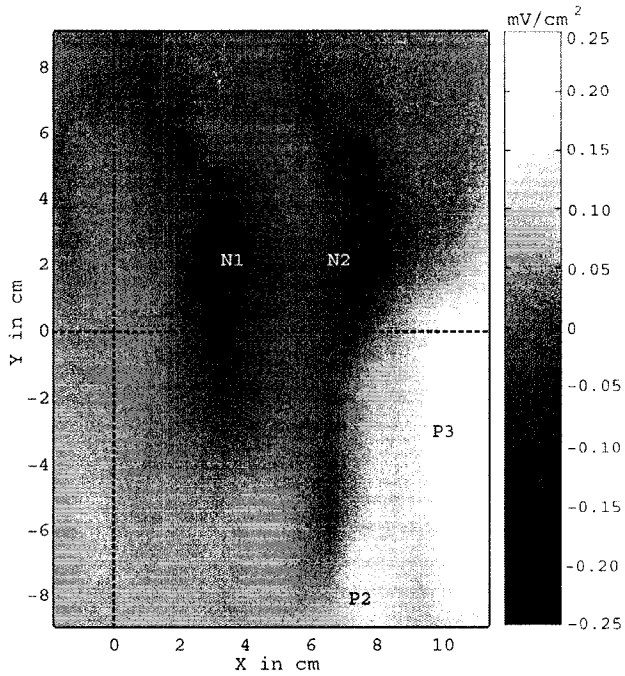

Figure 4.23. Tripolar BSLM from subject No. 1.

In summary, the pattern characteristics of the BSLM at the instant of the R-wave peak are consistent among all subjects with certain minor variations in the number of the activities and their locations. The positive activities all occurred in the left inferior chest area and the negative activities appeared over the right anterior central chest. N1 and N2 were present in all 6 subjects over the central or left central chest with slightly different locations. P3 was seen at nearly the same location in all subjects over the left lateral inferior chest but encompassed slightly different areas. Compared to one averaged cardiac activation cycle of the tripolar LECG, which were shown in Figures 4.18, 4.19 and 4.20, it can be seen that N1 can be related to area "a" and P3 can be related to area "b". P1 and P2 were both observed in 3 subjects (No. 2, 4, and 5) with minor location differences. For some subjects whose tripolar BSLM did not exhibit simultaneous P1 and P2 activities, at least one of the activities still occurred, that is, either P1 (subject No. 3)

or P2 (subjects No. 1 and 6). For subjects No. 2 and 6, there is a third negative area shown around the left inferior chest.

4.2.5 MOA Isochronal Mapping

The MOA were used to produce isochronal maps of the tripolar LECG on the body surface using Matlab® 6.5. The isochrones represent timing of cardiac electrical activation as it reaches the body surface below the active LECG TCE sensors. Figure 4.24 shows the MOA isochronal map from subject No. 4. The propagation time sequence of the cardiac activation as seen on the chest surface with respect to the Lead II ECG R-wave peak is shown using isochrones with the MOA denoted in units of [ms]. The range of the MOA was restricted to -40 to 40 ms with isochrones of 5 ms increments shown by bold black lines.

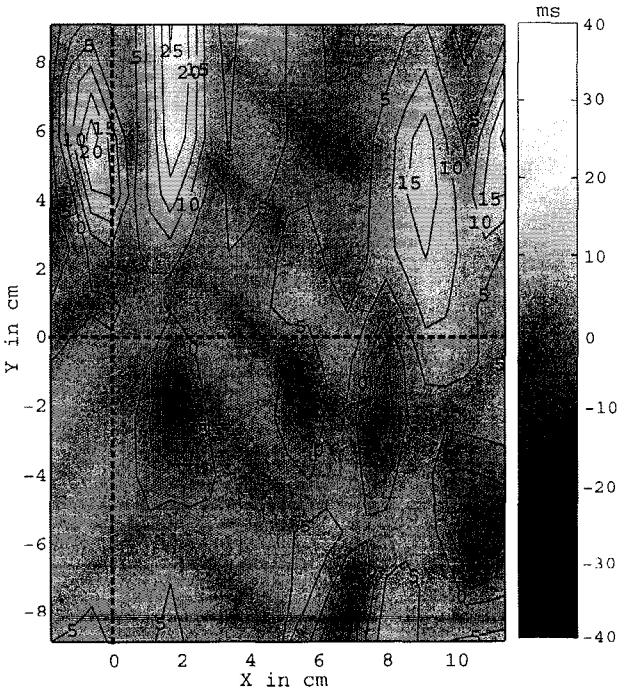

Figure 4.24. MOA isochronal map showing the timing of the cardiac electrical activation as seen on the chest surface relative to the Lead II ECG R-wave peak for subject No. 4. The abscissa and ordinate (x, y) in [cm] designate the position of the MOA map over the chest. The two dashed lines correspond to the nipple line and sternal

midline. The shade toward black designates earlier activation with respect to the Lead II ECG R-wave, and the shade toward white designates later activation.

Notice that the isochrones of the MOA map of Figure 4.24 had diverse geometric patterns. Regions of sparse (e.g. area with center located at (2, -2)) and crowded (e.g. area with center located at (0, 6)) isochrones, indicating spatial nonuniformities of cardiac activation spread, were discovered on the MOA map. The range of MOA in Figure 4.24 is -14.5 ms to 25.5 ms. Multiple localized earlier activation areas were observed. The areas with centers located at (2, -2) and (10, -6) had early MOA isochrones of -10 ms. Other earlier activation time sequences with centers located at (-1.8, 3), (6, -2), (8, -2), and (7, -8) had early MOA isochrones of -5 ms. Positive time sequences showing later activation are viewed over a broad area which is mainly on the top and right side of the map.

Figure 4.25 shows the MOA isochronal map from subject No. 3. The range of MOA in Figure 4.25 is -14 ms to 23 ms. Similar as subject No. 4, multiple localized earlier activation areas were observed in Figure 4.25. The areas with centers located at (2, 1.5) and (-1, -8) had early MOA isochrones of -10 ms. Other earlier activation time sequences with centers located at (3, -6), (6.5, 2), and (10, -4) had early MOA isochrones of -5 ms. Positive time sequences were located at the right superior central chest area.

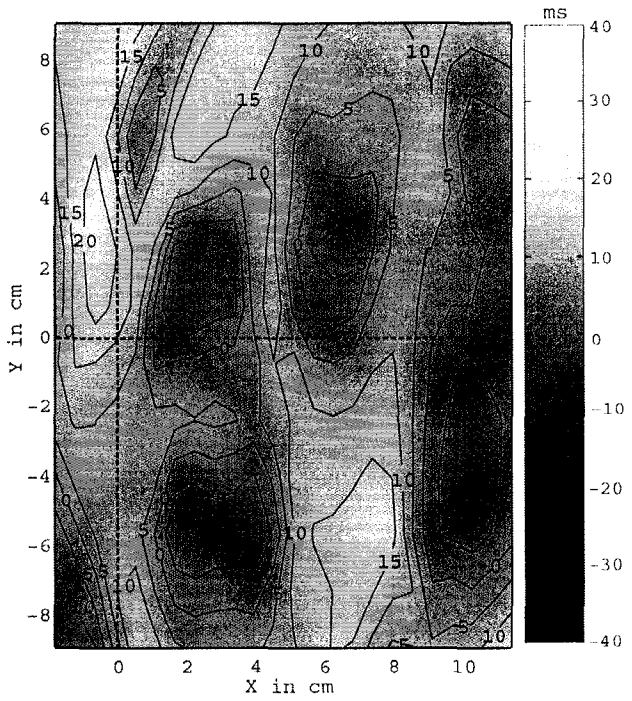

Figure 4.25. MOA isochronal map for subject No. 3.

The MOA isochronal map from subject No. 1 is shown in Figure 4.26. The range of MOA in Figure 4.26 is -17.5 ms to 29 ms. Multiple localized earlier activation areas were also observed for subject No. 1. The area with center located at (11, -3) had early MOA isochrones of -15 ms. Other earlier activation time sequences with centers located at (4, 2), (7, 2), and (8, -6) had early MOA isochrones of -5 ms. Positive time sequences were located at the superior chest area.

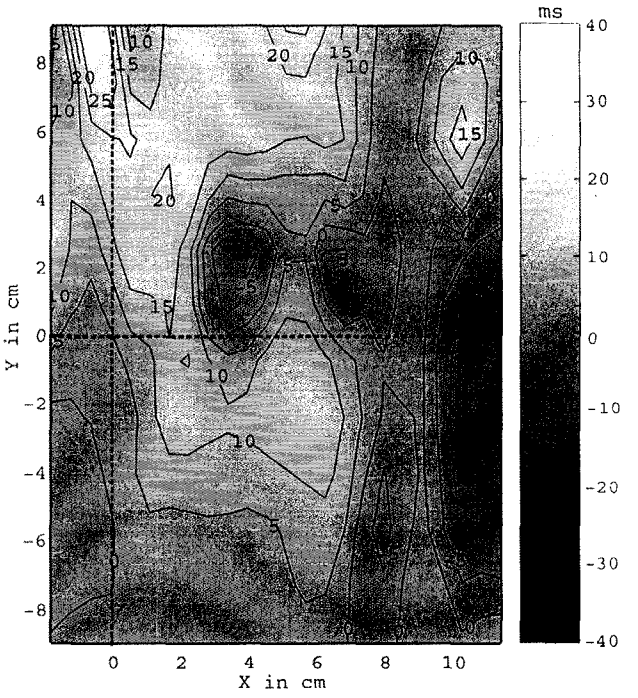

Figure 4.26. MOA isochronal map for subject No. 1.

In summary, for all 6 subjects the range of MOA is -25 ms to 31 ms. As the cardiac activation projects to the chest, the earlier activation area over the central or left central chest (e.g. the area located at (2, -2) in Figure 4.24, the area located at (2, 1.5) in Figure 4.25, and the area located at (4, 2) in Figure 4.26) is viewed in all 6 subjects with slightly different locations and occurrence times. The deviation for this earlier area is within a range of 2.5~3.6 cm in X or Y.

The variation in the early occurrence time is within 10 ms. This earlier activation area can be related to area "a" in the figures which show one averaged cardiac activation cycle of the tripolar LECG (Figures 4.18, 4.19 and 4.20) and N1 activity in the tripolar BSLM (Figures 4.21, 4.22 and 4.23). For the two earlier activation areas over the left chest (e.g. located at (6, -2) and (8, -2) in Figure 4.24), they were observed simultaneously from 2 subjects (No. 4 and 6) with slight variation in locations. However,

for subjects No. 1, 2, and 3, only one such earlier area appeared around the left chest. This earlier area might be related to N2 activity in the tripolar BSLM. For subject No. 5, there is no such earlier area shown. The earlier activation area over the left lateral inferior chest (e.g. the area located at (10, -6) in Figure 4.24, the area located at (10, -4) in Figure 4.25, and the area located at (11, -3) in Figure 4.26) was observed from all subjects with minor variations in locations and early MOA isochrones. This earlier activation area might be related to P3 activity in the tripolar BSLM.

All subjects showed at least one earlier activation area around the inferior chest area (e.g. the area located at (7, -8) in Figure 4.24, the area located at (3, -6) in Figure 4.25, and the area located at (8, -6) in Figure 4.26) which might be related to P1 or P2 activity in the tripolar BSLM. For the other earlier activation areas among subjects, such as the ones located at (-1.8, 3) in Figure 4.18 and located at (-1, -8) in Figure 4.25, there were very large variations which we cannot explain in this study. Most positive timing sequences were observed on the top area of the MOA maps in all 6 subjects, showing delayed activation after the R-wave peak.

CHAPTER 5

DISCUSSION

5.1 Computer Simulation

The LECG, as demonstrated by many investigators, enjoys enhanced spatial resolution and sensitivity to the cardiac electrical activity located beneath the surface recording electrodes. Three LECG (tripolar, bipolar, and spline) estimators have been mainly used to approximate the body surface LECG and perform the BSLM. The local-based tripolar and bipolar LECG are obtained directly from the body surface by approximating a planar surface at the recording site of the concentric ring electrodes. The global-based spline LECG is derived from the body surface potentials using the body surface geometric parameters which require further detail such as CT or MRI. The process of the interpolation may also introduce some error since the spline uses curves to interpolate between points which are evident at the boundaries in the spline BSLMs in Figures 4.7, 4.9, 4.10, and 4.11. The present study, for the first time, compared the three LECG estimators by building a simple planar model and a simplified heart-torso sphere-cylinder model and simulating the cardiac electrical activities with radial or tangential dipoles.

In this study it was assumed that the heart-torso model was a homogeneous conductor with a single normalized interior conductivity of 1.0. The heart and torso were

approximated as a sphere and a cylinder, respectively. This is a simplified condition which makes the simulation easier to be performed. In a real case, the heart-torso includes several inhomogeneities. For example, the lungs and muscles have different conductivities from the heart. The shapes of the heart and torso are not spherical and cylindrical. These facts have a considerable effect (Wei 2001, Li *et al.* 2003, He *et al.* 2002) on the directions and magnitudes of the cardiac electrical signals. However, in this study the real LECG and BSLM on the body surface were not the focus. The comparison between the three estimated LECG and BSLMs was the main goal. As long as the three estimated LECG and BSLMs were simulated under the same conditions, the relative results can be compared.

When modeling the TCE and BCE, the center disc, middle ring, and outer ring covered different numbers of nodes. The number of nodes in each element depends on the dimensions of the element and the resolution of the planar or torso cylinder surface. Since the potential of each element was calculated using Equation (3.1) averaging potentials of all nodes within each element, the number of nodes in each element should not influence the outcome. However, if the nodes are asymmetrically distributed in the electrode elements, this could bias the average potential.

When comparing over all recording sites as shown in Table 4.3 and Figure 4.4, the RMSE of the tripolar and bipolar LECG do not change significantly when the number of electrodes increased ($p=0.0729$ and $p=0.0702$ between 25 and 289 electrodes for tripolar and bipolar LECG respectively with all dipole configurations). Since tripolar and bipolar LECG estimates the local Laplacian of the surface potential using the TCE and BCE which only depends on the three or two elements (the center disc and two

concentric rings) of the electrode, the error of the tripolar and bipolar LECG, with respect to the relative analytical LECG at the same recording sites, should not change with the variation of the number of recording electrodes. Namely, the tripolar and bipolar LECG are not influenced by the spatial sampling rate. This feature can be seen by observing Table 4.2 and Figure 4.2 in which the tripolar and bipolar LECG have the same RMSE over the nine recording sites that were common to each electrode array.

The slight variation of RMSE in Tables 4.1 and 4.3 and Figures 4.1 and 4.4 for tripolar and bipolar may be related to the four recording arrays have different numbers of electrodes and different recording sites (Figure 3.4). The error at each recording site is dependent on where the electrode is located. Therefore, when calculating the RMSE of the four recording arrays, there will be slight variations. In commertially available applications, there are more sophisticated methods of calculating the potentials of electrodes. By using those methods, the variations due to the asymmetry of the nodes when calculating the average potential of the elements on the electode used in this study (Equation (3.1)) would be lessened for the tripolar and bipolar LECG.

According to the spline LECG algorithm, the spline interpolation depends on the number of recording sites, namely, the spatial sampling rate. When recording body surface potentials at more sites in the same area, more accurate potentials will be calculated at the interpolated sites. A more accurate potential function will be derived for this area, therefore improving the Laplacian from spline LECG. In summary, the higher the spatial sampling rate (the shorter the distance between recording sites), the more the recording sites, then the more accurate the spline LECG is compared with the analytical LECG at each recording site. In Tables 4.1, 4.2, and 4.3 and Figures 4.1, 4.2,and 4.4, the

spline LECG shows significantly decreased RMSE with increased recording electrodes (p= 0.0067 between 25 and 289 electrodes for spline LECG with all dipole configurations). For example, in Table 4.3 and Figure 4.4 dipole configuration 3 (C.3), the spline LECG is more accurate than the bipolar LECG when using 121 or 289 electrodes. The variation in RMSE due to increasing recording electrodes was much greater for spline LECG than tripolar or bipolar LECG.

The simulation results demonstrate that for different dipole configurations and numbers of recording electrodes studied, the tripolar LECG has significantly better RMSE than the bipolar (p=4.74e-6) and spline (p=5.48e-4) LECG. With only a few recording sites on the body surface (such as 25), the tripolar LECG still has significantly better performance than the bipolar and spline LECG with many more recording sites (such as 121 or 289) for all dipole configurations studied (Figure 4.5). For example, the RMSE is significantly less for the tripolar LECG with 25 electrodes than the spline LECG with 289 electrodes (p=0.0331). Also noteworthy is that there are an infinite number of possibilities of source dipoles. Although an extensive number of configurations were analyzed for this research, there may be some dipole configurations where the spline LECG may have less RMSE than tripolar LECG.

Notice that in Table 4.3 for dipole configurations 4 and 6 (C.4 and C.6), the RMSE of the three estimated LECG is much smaller than that for other dipole configurations. This may be due to dipole configurations 4 and 6 (C.4 and C.6) in which the source dipoles located at the posterior wall of the heart which were farther away from the recording sites on the body surface. Therefore, the estimated and analytical LECG for dipole configurations 4 and 6 (C.4 and C.6) were much smaller than that for other dipole

configurations. According to Equation (3.6), RMSE should be smaller for dipole configurations 4 and 6 (C.4 and C.6).

From Figures 4.13 and 4.14, two findings are obvious. First, for all three LECG estimators, the higher the PN level, the higher the RMSE. Second, for all cases studied, the tripolar LECG always shows the least RMSE among the three estimated LECG for a given PN level. This reflects the powerful background noise attenuation ability of the tripolar LECG. This improvement is not only shown at the same PN level, but the tripolar LECG shows a better or comparable performance at higher noise levels when compared to the bipolar and spline LECG at lower noise levels. This can be observed from the RMSE curves in Figures 4.13 and 4.14. For example, in Figure 4.13B, the tripolar LECG with 15% PN has lower RMSE than the bipolar LECG with 3% PN and comparable RMSE with the spline LECG with 10% PN. This is due to the common-mode rejection properties of the closely spaced tripolar electrode elements. The inter-element distance was set to 0.885 cm for TCE which is much smaller than that of BCE (1.77 cm). Therefore, the common potential (noise) on each element of TCE is closer to each other than BCE. According to Equations (2.17) and (2.12), when calculating the bipolar potential differences between the concentric rings and center disc, the noise would be cancelled out more for TCE than for BCE. For spline LECG, the electrode spatial resolution was 1.25 cm which is between the inter-element distances of the TCE and BCE. The spline LECG algorithm uses the potential at each recording site which is contaminated with noise.

From Figure 4.15, it can be seen that the abilities of identifying the multiple sources are different for the three estimated LECG. The tripolar BSLM shows the best

spatial resolution with the highest SC (Table 4.4). The spline BSLM has comparable performance with the tripolar BSLM but greater distortion when compared to the analytical BSLM (Figure 4.15B). The bipolar BSLM provides the worst spatial resolution. The two maxima for bipolar which correspond to the two dipoles almost connect to each other which makes it hard to differentiate the two sources on the BSLM. The Lower SC of the bipolar LECG also demonstrates this further.

5.2 Human Experiment

Previous studies (He and Cohen 1991, 1992, 1995, He and Wu 1999, Umetani *et al.* 1998, Wu *et al.* 1998, 1999, He 1998, Ono *et al.* 1997, Lian *et al.* 2002a, 2002b, Li *et al.* 2002, 2003, He *et al.* 2002, Besio 2001, Besio *et al.* 2001, Besio and Tarjan 2002a, 2002b, Lu and Tarjan 1999) applied unipolar, bipolar, and quasi-bipolar electrodes to record and estimate the LECG. For unipolar electrodes, the FPM and spline surface Laplacian estimators were used to derive the LECG from the potential ECG. As a result, the FPM and spline LECG may be sensitive to measurement noise. For the FPM Laplacian estimation, the 5 discs were shown to be directionally dependent (Geselowitz and Ferrara 1999). Lian *et al.* (2001) reported that the directional dependence reported may not be valid. Our new active LECG TCE sensor has a circular symmetrical design, which overcomes the stated directionality problem. Further, with the new active LECG TCE sensor the LECG can be obtained directly from the body surface. This positive aspect could be beneficial when CT and MRI are not available to obtain the body surface geometric parameters that are necessary for spline LECG estimation (He *et al.* 2002, Lian *et al.* 2002b, Li *et al.* 2003).

Since the skin surface generally conforms to the planar surface of the sensor (Lian *et al.* 2001), we can appropriately perform an estimate of the local Laplacian with the new designed active LECG TCE sensor. The dimensions of the electrode elements on the new active LECG TCE sensor were chosen based on the following three reasons: (a) previous research (Besio 2001, Besio *et al.* 2001) used the same electrode element dimensions; (b) the distance between the heart wall and the sensor, which is roughly 3~5 cm, was shown to be the optimal diameter for the outer ring of the concentric ring electrode sensor (Kaufer 1992); (c) the smaller the spacing between the elements, the closer approximation of the "true" Laplacian, but the weaker the signal. The dimensions chosen assure sufficient amplitude for a reasonable signal-to-noise ratio.

In computer simulation the dimension of the TCE was slightly different from the newly designed active LECG TCE sensor. The area of the three electrode elements of the TCE model (center disc=3.14e-4 cm^2, middle ring=3.33e-1 cm^2, outer ring=6.67e-1 cm^2) was different from the active LECG TCE sensor (center disc=1.96e-1 cm^2, middle ring=2.07e-1 cm^2, outer ring=1.08e-1 cm^2). However, it will not influence the comparison between the TCE model and the active LECG TCE sensor since the three electrode elements' potentials will be minimally affected by the different area. The only difference between the TCE model and active LECG TCE sensor is that the TCE model could have more spatial resolution since the inter-element distance is smaller for the TCE model (0.885 cm) than for the active LECG TCE sensor (0.9 cm).

This paper reports on the experimental investigation of a new active LECG TCE sensor used on a group of six healthy human male subjects. Since the recordings were conducted at 1.2 cm and 3.6 cm intervals in horizontal and vertical directions,

respectively, the LECG acquired had higher spatial resolution compared with the other previous LECG recordings (Besio *et al.* 2001), 72 vs. 35 locations over the same chest area. Another positive attribute is that the inter-element spacing on the new sensor is less than 1.0 cm (Figure 3.8B) providing even greater spatial resolution. In this pilot study, the vertical spatial resolution was less than the horizontal resolution. However, in the BSLM and MOA algorithm, vertical and horizontal directions were interpolated to have the same spatial resolution.

The cardiac body surface data was bandpass filtered by the Grass amplifier system with a bandwidth of 1 ~ 500 Hz. According to the Nyquist–Shannon sampling theorem, which states that exact reconstruction of a continuous-time baseband signal from its samples is possible if the signal is bandlimited and the sampling frequency is greater than twice the signal bandwidth, the sampling rate should be at least 1000 Hz. In this study, the analog signals were digitized from the Grass amplifier system at a sampling rate of 2000 Hz to achieve enough time resolution.

In Figure 4.17, the duration of the LECG QRS waves are shorter than that of the Lead II ECG which is consistent with the previous simulation results (He and Cohen 1992) that the LECG has a sharper and narrower shape compared to the ECG. This is why the LECG has higher spatial resolution than potential ECG.

Note that tripolar and bipolar LECG recorded simultaneously using these active LECG TCE sensors show similar activation patterns (Figures 4.18, 4.19, and 4.20 Panels A and B). This similarity was also shown in Table 4.5 with high CC (0.912 ± 0.091) between tripolar and bipolar LECG. From both panels in Figures 4.18, 4.19, and 4.20, we can see the LECG's polarity changes while the cardiac electrical activation is spreading

over the whole chest. If the wavefronts are represented by moving dipoles, the dipoles move forward and gyrate as well. The conventional V-leads capture this activity. As the depolarization moves from right to left ventricle and downward in the septum and upward in the free wall, the signals go from monophasic negative to monophasic positive and somewhere between the two metamorphose as shown by the biphasic template. The swings may be interpreted as the wavefront moving toward the active LECG TCE sensor exhibiting one direction of polarization while the departure of the wavefront displays the opposite polarization.

In Figures 4.18, 4.19, and 4.20, the LECG showed strong signals at a few electrodes around area "a", whereas most other electrodes far away from area "a" showed relatively weak signals. Area "b" also showed strong signals. The signal strength on the body surface depends on many factors including source strength, source orientation, and volume conduction properties. For example, the cardiac signals are attenuated due to the low conductivity of the lungs. From the figures, it appears that area "a" overlaps with the heart base, whereas area "b" may be near the heart apex. As can be seen, there were variations in location and signal magnitude for area "a" and area "b", which may due to the effects of the variations in the heart position and conductivities in each subject (Macleod *et al.* 2000).

The SSy, which was calculated at the center of area "a", was used in this study to directly compare the local sensitivity between tripolar and bipolar LECG. The SSy for tripolar LECG in all six subjects is greater than for bipolar LECG (Table 4.6). This increased SSy may result in tripolar LECG more accurately locating the cardiac activation origins over bipolar LECG. We must clarify that we have not performed

invasive experiments to verify where the source is located under our electrode array, but have reported on similar characteristics previously (Besio *et al.* 2006).

MOA denotes the activation time on the body surface of the LECG at each recording site and can be used to make isochronal maps. As mentioned previously, the zero-crossing of the LECG (Lu and Tarjan 1999, Kaufer 1992) has been used as a time reference as long as the trajectory of the depolarization wavefront is simple. In such a case, zero-crossing occurs when the vector passes the axis of the sensor (Kaufer 1992). This appears to be an inappropriate model in the present study for at least two reasons: (i) the LECG are not always biphasic waveform (doublet); and (ii) the dipoles move along complicated paths. A new approach with high noise immunity was found when the Lead II ECG was used as a reference and correlated with the LECG (Besio 2001, Besio *et al.* 2001, Besio and Kota 2004). The correlation results in leading or lagging times as MOA of the LECG.

Comparing our tripolar BSLM with the previous studies of the FPM and spline BSLM (Wu *et al.* 1999 and Li *et al.* 2003), the detailed spatial patterns are similar (e.g., N1 in the tripolar BSLM corresponds to N2 reported by Li *et al..,* N2 in the tripolar BSLM corresponds to N3 reported by Li *et al..,* P1, P2, and P3 in the tripolar BSLM correspond to P2 activity and its subcomponents reported by Wu *et al.*). Previous study (Li *et al.* 2003) linked the multiple activation areas in the BSLM to the underlying cardiac electrical activations. In the MOA isochronal map, we can also see multiple earlier activation areas. Therefore, by relating the multiple activation areas in the tripolar BSLM and MOA isochronal map, we might be able to interpret the MOA isochronal map with respect to the underlying cardiac electrical activations.

For subject No. 4, in Figure 4.24 the earlier activation area which is located at (2, -2) (also area "a" in Figure 4.18) coincides with the negative activity N1 in Figure 4.21. The same relation can also be found for subjects No. 3 and 1. For subject No. 3, in Figure 4.25 the earlier activation area which is located at (2, 1.5) (also area "a" in Figure 4.19) coincides with the negative activity N1 in Figure 4.22. For subject No. 1, in Figure 4.26 the earlier activation area which is located at (4, 2) (also area "a" in Figure 4.20) coincides with the negative activity N1 in Figure 4.23. This earlier activation area may reflect the earliest epicardial breakthrough of the right ventricle during ventricular depolarization (Wyndham *et al.* 1979, Li *et al.* 2003). N2 activity appeared at almost the same location as the earlier activation area located at (6, -2) for subject No. 4, (6.5, 2) for subject No. 3, and (7, 2) for subject No. 1. According to Wyndham *et al.* (1979), this earlier activation area may be related to the subsequent breakthrough occurring in the left ventricular site anteriorly adjacent to the mid-portion of the septum. P2 activity may be related to the earlier activation area located at (7, -8) for subject No. 4 and (8, -6) for subject No. 1 with a larger variance in location. This earlier activation area may reflect the initial depolarization of the left ventricle (Li *et al.* 2003). P1 activity for subject No. 4 cannot be related to any earlier activation area in Figure 4.24. For subject No. 3, the earlier activation area located at (3, -6) in Figure 4.25 can be related to P1 activity in Figure 4.22. This earlier activation area may reflect the initial depolarization of the right ventricle (Li *et al.* 2003). The earlier activation area center at (10, -6) for subject No. 4, (10, -4) for subject No. 3, and (11, -3) for subject No. 1 appears to correspond to P3 activity (Figures 4.21, 4.22 and 4.23). It may also reflect the initial depolarization of the left ventricle (Li *et al.* 2003).

For the other earlier activation areas located at (8, -2) and (-1.8, 3) in Figure 4.24 and (-1, -8) in Figure 4.25, we cannot find the corresponding positive or negative activities in the tripolar BSLM. This may result from the following two reasons. First, the MOA isochronal map may provide more spatiotemporal details than the BSLM. For example, the earlier activation area at (8, -2) in Figure 4.24 may be related to another epicardial breakthrough occurring in the left ventricle. Second, the propagation of the wavefront (or dipole) is very complex. It is affected by the anatomical location or orientation of the heart. And the movement of our sensors on the body surface relative to the heart due to respiration may also cause some distortions of the time sequence. This may also explain why P1 activity cannot be related to any earlier activation area in Figure 4.24.

There were slight variations in the number of the activities, activation times and locations in the tripolar BSLM and MOA maps among subjects. This may be due to differences in body conductivity and variation in heart orientation/position within the chest caused by the body position (Macleod *et al.* 2000). However, within each subject, the patterns of the multiple activations in the tripolar BSLM and MOA map can be related such that the MOA map can be interpreted with respect to the underlying cardiac electrical activations. For example, for every subject, N1 activity can always be related to the corresponding earlier activation area over the central or left central chest of the MOA map. P3 activity can be related to the earlier activation area over the left lateral inferior chest for five subjects (except subject No. 2). N2 activity can be related to the earlier activation area around the left chest for five subjects (except subject No. 5) with minor location differences.

In some cases, the automated procedure for calculating MOA (Besio and Kota 2004) chose an incorrect value. The Lead II ECG QRS wave is about 100 ms in healthy subjects. During that time the ventricles must be depolarized everywhere in a normal heart. The reference point (R-wave peak) is the middle of the QRS peak. Some of the ventricular depolarization must happen prior to the R-wave peak and some ventricular depolarization must happen after the R-wave peak. Therefore, if some sites are leading the R-wave peak and some lag behind, it is attributable to the normal propagation sequence of cardiac depolarization. In healthy subjects, the MOA should range from approximately -50 ms to 50 ms. In this study, the normal range of the MOA was chosen between -40 ms and 40 ms. If the MOA exceeded this range, it was considered incorrect. This may happen when the LECG, which was recorded at a location far away from the heart was of weak magnitude and below the noise, produced the wrong activation time offset. In these situations, when making MOA isochronal maps, the incorrect MOA was discarded manually and its neighbor's MOA were used to interpolate the new MOA for this recording site. In this study, there were on average three incorrect MOA values corrected out of 72 for each subject. The incorrect MOA were in the range of -82 ms to 112 ms in all six subjects. For example, for subject No. 4, the three incorrect MOA values were 87 ms, 104 ms and -79 ms.

In this pilot study, the MOA was derived from the LECG which was recorded on the body surface. Therefore, MOA isochronal mapping only provides an approximation of the underlying cardiac activation. The MOA isochronal map was explained with respect to the underlying cardiac electrical events by comparing and relating to the BSLM and previous studies (Wyndham *et al.* 1979 and Li *et al.* 2003). The explanation

has not been verified with invasive measurements or other localizing modalities. Since only 6 subjects have been recorded, no statistical conclusion on the MOA time sequence patterns is available and it is difficult to draw any definitive conclusions on the merits of the TCE-based MOA mapping.

CHAPTER 6

CONCLUSION/SUMMATION

While a simplified volume conductor model (eccentric sphere-cylinder model) is used in the computer simulation, the present results do provide reasonable comparisons between the three estimated LECG. The spline LECG estimation worsens significantly ($p=0.00984$ between 289 and 25 electrodes) when fewer electrodes are used since spline interpolation depends on the spatial sampling rate. For the tripolar and bipolar LECG, there is no significant change while electrodes increased from 25 to 289 ($p=0.0729$ and $p=0.0702$ between 25 and 289 electrodes for tripolar and bipolar LECG, respectively).

The tripolar LECG provides the most accurate LECG estimation among the three LECG estimators using fewer TCE (such as 25 or 81) without the knowledge of the body surface geometric parameters, unlike the spline LECG. The spline LECG may achieve similar accuracy when using more electrodes (such as 289). However, this will cost much more computation resources. In clinical applications, using so many recording electrodes is not appropriate.

The high performance in noise attenuation and spatial resolution make the tripolar BSLM appropriate for differentiating and locating multiple concurrent cardiac activities.

The same results should still hold for a more realistic volume conductor model with pacing sites. The tripolar LECG and BSLM may enhance our capability and efficiency to image cardiac bioelectrical sources on the body surface.

The human experiment in the present study is a pilot study investigating the spatiotemporal patterns of the tripolar BSLM and Laplacian MOA isochronal maps from healthy male subjects using the newly designed active LECG TCE sensor. The long term goal is to provide a practical noninvasive tool for clinicians diagnosing arrhythmias and assessing the efficacy of therapy. We demonstrated that the active LECG TCE sensor provides enhanced spatial information than the bipolar concentric ring electrode which other authors have shown provides increased spatial frequencies over conventional disc electrodes (He and Cohen 1992). The tripolar BSLM showed similar attributes as the spline BSLM (Li *et al.* 2003) but without constructing the surface geometry function. By comparing with the BSLM, the Laplacian MOA isochronal maps may be related to the underlying cardiac activations. The results presented for the six healthy subjects studied are promising considering biological variability.

In a future study, a more realistic inhomogeneous volume conductor model with pacing sites will be simulated. For human experiments, much data of cardiovascular diseased patients is necessary to validate any clinical utility. More locations need to be recorded to achieve higher resolution of the progression of cardiac activation. It was shown that LECG and BSLM could differentiate atrial activation patterns (Besio and Tarjan 2002a, b, Soundararajan and Besio 2005). Further work is also necessary to differentiate the atrial and ventricular activation by MOA mapping. A pathological database will be finally built for identifying certain pathologies from MOA maps.

APPENDIX A

IRB PROTOCOL

STUDY/PROJECT INFORMATION FOR HUMAN SUBJECTS COMMITTEE

TITLE: A Unique Non-invasive Laplacian Electrocardiogram (ECG) System

PROJECT DIRECTOR(S):

Walter G. Besio, Ph.D.

DEPARTMENT(S): Biomedical Engineering

PURPOSE OF STUDY/PROJECT: We want to build a non-invasive cardiac diagnosis and monitoring instrument that produces reliable information about atrial activation patterns that are critical in the diagnosis and subsequent treatment of heart disease. Our final goal is to develop a high spatial resolution Laplacian ECG mapping system that is capable of non-invasively detecting not only ventricle activity but also atrial activation patterns. This system will reduce the time invested by the cardiologist, cost to medical facilities for diagnosis and therapy and, most of all, trauma to the patient. ECG signals will be acquired and stored for analysis to determine trends in alertness.

SUBJECTS: Louisiana Tech University students, faculty, and staff, healthy people

PROCEDURE: Several subjects will be tested in the following manner:

ECG electrodes will be positioned over the chest and back, and a reference electrode at some nonmoving part of the body to form a Lead II ECG configuration.

Active ECG electrodes will be placed on the subject's torso and attached with an elastic strap to hold them firmly in place.

The subject will lie down on a table and relax while the ECG signals are recorded and sent to a laptop for data storage.

The active ECG electrodes will be moved from the subject's chest to back every 6mm. The ECG recordings will be simultaneously monitored and stored.

The ECG signals will be processed offline.

INSTRUMENTS AND MEASURES TO INSURE PROTECTION OF CONFIDENTIALITY, ANONYMITY: **Names of subjects will not be released. All reporting of data will refer to subjects in a general manner.**

RISKS/ALTERNATIVE TREATMENTS: **There are no risks associated with this study, neither are there alternative treatments.**

BENEFITS/COMPENSATION: **The subjects will have a measure of their ECG recordings, which eventually will help us, develop a new non-invasive Laplacian electrocardiogram (ECG) system. There is no form of compensation.**

SAFEGUARDS OF PHYSICAL AND EMOTIONAL WELL-BEING:

Subjects will be electrically isolated from wall power during the recording of ECG signals. This is due to the ECG amplifiers being powered by nine-volt radio batteries. These amplifiers have been

commonly utilized by Dr. Besio for recording physiological signals from humans and animal subjects for several years. The input impedance of the amplifiers is greater than 100 meg ohm. The input bias current for the amplifier is 10 nano amps. This is an imperceptible amount of current that you will not be able to feel or be harmed by. Due to the added skin to electrode impedance, this current will be further reduced. The reference ECG will be recorded with the standard Lead II configuration.

A laptop computer will be used for acquiring the data. It will be powered via its battery. A data acquisition instrument (DI-720 Series) digitizes the analog signals from the ECG electrodes. The analog input impedance of DI-720 is 1 Mohms. An interface is designed to connect the DI-720 and active ECG electrodes by using the phone jacks. The DI-720 will also be powered by batteries isolating the subject further from the AC mains.

No subject names will be used in the reporting of data. The subjects will be treated cordially.

2/2002-GS-BD

HUMAN SUBJECTS CONSENT FORM

The following is a brief summary of the project in which you are asked to participate. Please read this information before signing the statement below.

TITLE: A Unique Non-invasive Laplacian Electrocardiogram (ECG) System

PURPOSE OF STUDY/PROJECT: We want to build a non-invasive cardiac diagnosis and monitoring instrument that produces reliable information about atrial activation patterns that are critical in the diagnosis and subsequent treatment of heart disease. Our final goal is to develop a high spatial resolution Laplacian ECG mapping system that is capable of non-invasively detecting not only ventricle activity but also atrial activation patterns. This system will reduce the time invested by the cardiologist, cost to medical facilities for diagnosis and therapy and, most of all, trauma to the patient. ECG signals will be acquired and stored for analysis to determine trends in alertness.

PROCEDURE: Several subjects will be tested in the following manner:

ECG electrodes will be positioned over the chest and back, and a reference electrode at some nonmoving part of the body to form a Lead II ECG configuration.

Active ECG electrodes will be placed on the subject's torso and attached with an elastic strap to hold them firmly in place.

The subject will lie down on a table and relax while the ECG signals are recorded and sent to a laptop for data storage.

The active ECG electrodes will be moved from the subject's chest to back every 6mm. The ECG recordings will be simultaneously monitored and stored.

The ECG signals will be processed offline.

INSTRUMENTS: Instruments used to collect data include ECG filters and amplifiers, an isolated laptop computer with a data acquisition instrument DI-720 Series and software controlling the acquisition, and interface used to connect the DI-720 and ECG electrodes.

RISKS/ALTERNATIVE TREATMENTS: There are no risks associated with this study, neither are there alternative treatments.

BENEFITS/COMPENSATION: The subjects will have a measure of their ECG recordings, which eventually will help us, develop a new non-invasive Laplacian electrocardiogram (ECG) system. There is no form of compensation.

I, _____, attest with my signature that I have read and understood the following description of the study, "A Unique Non-invasive Laplacian Electrocardiogram (ECG) System," and its purposes and methods. I understand that my participation in this research is strictly voluntary and my participation or refusal to participate in this study will not affect my relationship with Louisiana Tech University or my grades in any way. Further, I understand that I may withdraw at any time or refuse to answer any questions without penalty. Upon completion of the study, I understand that the results will be freely available to me upon request. I understand that the results of my testing will be anonymous and confidential, accessible only to the principal investigators, myself, or a legally appointed representative. I have not been requested to waive nor do I waive any of my rights related to

participating in this study.

_____ _____

Signature of Participant or Guardian Date

CONTACT INFORMATION: The principal experimenters listed below may be reached to answer questions about the research, subjects' rights, or related matters.

Dr. Walter Besio (257-4562)

Members of the Human Use Committee of Louisiana Tech University may also be contacted if a problem cannot be discussed with the experimenters:

Dr. Terry McConathy (257-2924)
Dr. Mary M. Livingston (257-2292)
Mrs. Deby Hamm (257-2924)

2/2002-GS-BD

APPENDIX B

ABBREVIATION TABLE

atrio-ventricular node	AV node
bipolar concentric ring electrode	BCE
body surface Laplacian mapping	BSLM
body surface potential mapping	BSPM
correlation coefficient	CC
common-mode rejection ratio	CMRR
electrocardiogram	ECG
electromyogram	EMG
five-point method	FPM
instrumentation amplifier	IA
Laplacian ECG	LECG
moment of activation	MOA
nine-point method	NPM
printed circuit board	PCB
potential noise	PN
quasi-bipolar sensor	QBS
root-mean square error	RMSE
sinoatrial node	SA node
separation coefficient	SC
surface Laplacian	SL
tripolar concentric ring electrode	TCE
three-dimensional	3D
two-dimensional	2D

REFERENCES

Ames W F., 1969 Numerical methods for partial differential equations *New York: Barnes & Noble, Inc.* 15-9

Arfken G 1985 Mathematical methods for physicists 3rd ed. New York: Academic

Bertrand O, Garcia-Larrea L, Artru F, Mauguiere F and Pernier J 1987 Brain-stem monitoring I. A system for high-rate sequential BAEP recording and feature extraction *EEG and Clin. Neurophysiology* **68** 433-45

Besio W, Lu C and Tarjan P 2001 A feasibility study for body surface cardiac propagation maps of humans from Laplacian moments of activation *Electromagnetics* **21** 621-32

Besio W 2001 A study of Laplacian surface maps from moments of activation to detect cardiovascular disease Ph.D. Dissertation U. of Miami

Besio W and Tarjan P 2002a Atrial activation pattern from surface Laplacian electrocardiograms of humans *IJBEM* **4** 95-6

Besio W and Tarjan P 2002b Filtering of surface Laplacian electrocardiograms from humans to produce atrial activation patterns *Proceedings IEEE EMBC 2002 and BMES Annual Meeting* 1379-80

Besio W, Aakula R and Dai W 2004 Comparison of bipolar vs. tripolar concentric ring electrode Laplacian estimates *Proceedings IEEE. EMBC 2004* **1(3)** 2255-8

Besio W, Aakula R, Koka K and Dai W 2006 Development of a tri-polar concentric ring electrode for acquiring accurate Laplacian body surface potentials *Annals of BME* **34(3)** 426-35

Besio W and Kota A 2004 Laplacian ECG moment of activation detection algorithm during pacing *Proceeding IEEE EMBC* **1(2)** 948-51

Besio W and Chen T 2006 Non-invasive Laplacian electrocardiography and moment of activation mapping *Proceedings 28th Annual International Conference IEEE EMBS*

Bianco C 2000 How your heart works http://health.howstuffworks.com/heart.htm (May 07, 2007)

De A, Aim E, Ceriotti C, Rovida M and Negroni S 1997 Mapping of ventricular repolarization potentials in patients with arrhythmogenic right ventricular dysplasia: Principal component analysis of the ST-T waves *Circulation* **96** 4314-8

Fattorusso V and Tilmant J 1949 Exploration du champ electrique precordial a l'aide de deux electrodes circulaires, concentriques et rapprochees *Arch. Mal du Coeur* **42** 452-5 in French

Fenici R, Pesola K, Makijarvi M, Nenonen J, Teener U, Fenici P and Katila T 1998 Nonfluoroscopic localization of an amagnetic catheter in a realistic torso phantom by magnetocardiographic and body surface potential mapping *Pacing Clin Electrophysiol.* **21** 2485-91

Fitz-Clarke JR, Sapp JL, Warren JW, Clements JC, Horácek BM 2006 Body surface potential mapping and computer simulation of human ventricular fibrillation *Computers in Cardiology* **33** 397–400

Geselowitz D B and Ferrara J E 1999 Is accurate recording of the ECG surface Laplacian feasible *IEEE TBM* **46(4)** 377-81

He B 1997 Principles and applications of the Laplacian electrocardiogram *IEEE Eng. Med. Biol. Mag.* **16** 133-8

He B 1998 Theory and applications of body surface Laplacian ECG mapping *Proceeding IEEE EMBC* **17** 102-9

He B, Bansal S, Tsai A and Saul JP 1997 A comparison of volume conductor effects on body surface Laplacian and potential ECGs: A model study *Comput Biol Med.* 27(2) 117-27

He B and Cohen R 1991 Body surface Laplacian mapping in man *Proceeding IEEE EMBC* **13(2)** 784-6

He B and Cohen R 1992 Body surface Laplacian ECG mapping *IEEE Trans. on BME* **39(11)** 1179-91

He B and Cohen R 1995 Body surface Laplacian electrocardiographic mapping-A review *Critical Reviews in BME* **23(5-6)** 475-510

He B and Wu D 1997 A bioelectric inverse imaging technique based on surface Laplacians *IEEE TBME* **44(7)** 529-38

He B and Wu D 1999 Laplacian electrocardiography *Critical Reviews in BME* **27(3-5)** 285-338

He B, Li G and Lian J 2002 A spline Laplacian ECG estimator in a realistic geometry volume conductor *IEEE Trans. on BME* **49** 110-7

Huiskamp G 1991 Difference formulas for the surface Laplacian on a triangulated surface *J. Comput. Phys.* **95(2)** 477–96

Klug D, Ferracci A, Molin F, Dubuc M, Savard P, Kus T, Hlie F, Cardinal R and Nadeau R 1995 Body surface potential distributions during idiopathic ventricular tachycardia *Circulation* **91** 2002-9

Kaufer M 1992 Multi-ring sensing electrodes for arrhythmia detection and classification MS thesis University of Miami

Lapidus L and Pinder G F 1982 Numerical solution of partial differential equations in science and engineering *New York: John Wiley & Sons, Inc.* 371-2

Lian J, Srinivasan S, Tsai H and He B 2001 Comments on "Is accurate recording of the ECG surface Laplacian feasible?" *IEEE TBME* **48(5)** 610-3

Lian J, Srinivasan S, Tsai H, Wu D, Avitall B and He B 2002a On the estimation of noise level and signal to noise ratio of Laplacian ECG during ventricular depolarization and repolarization *Pacing and Clinical Electrophysiology* **25(10)** 1474-87

Lian J, Li G, Cheng J, Avitall B and He B 2002b Body surface Laplacian ECG mapping of atrial activation in normal subjects *Medical & Biological Engineering & Computing* **40(6)** 650-9

Li G, Lian J and He B 2002 On the spatial resolution of body surface potential and Laplacian pace mapping *Pacing and Clinical Electrophysiology* **25** 420-9

Li G, Lian J, Salla P, Cheng J, Shah P, Ramachandra I, Avitall B and He B 2003 Body surface Laplacian ECG mapping of ventricular depolarization in normal subjects *J. Cardiovascular Electrophysiology* **14(1)** 6-27

Lu C and Tarjan P 1999 An ultra-high Common-Mode Rejection Ratio(CMRR) AC instrumentation amplifier for Laplacian electrocardiographic measurement *Biomedical instrumentation & technology* **33** 76-83

Macleod R, Ni Q, Punske B, Ershler P, Yilmaz B and Taccardi B 2000 Effects of heart position on the body surface ECG *Internaional Society for Computerized Electrocardiography Conference Yosemite, CA*

Malmivuo J and Plonsey R 1995 Bioelectromagnetism: Principles and applications of bioelectric and biomagnetic fields *Oxford University Press* New York Oxford

Ono K, Hosaka H and He B 1997 A comparison of body surface Laplacian and potential maps during paced ventricular activation *Methods Info Med.* **36** 336-8

Oostendorp T F and Oosterom A V 1996 The surface Laplacian of the potential: theory and application *IEEE TBME* **43(4)** 394-405

Plonsey P 1969 Bioelectric phenomena New York: McGrawHill

Rudy Y and Plonsey R 1979 The effects of variations in conductivity and geometrical parameters on the electrocardiogram, using an eccentric sphere model *Circ Res.* **44** 104-11

Rudy Y and Plonsey R 1980 A comparison of volume conductor and source geometry effects on body surface and epicardial potentials *Circ Res.* **46** 283-93

Soundararajan V and Besio W 2005 Simulated comparison of disc and concentric electrode maps during atrial arrhythmias *IJBEM* **7(1)** 217-20

Taccardi B 1963 Distribution of heart potentials on the thoracic surface of normal human subjects *Circulation* **12** 341-52

Takala P, Hanninen H, Montone J, Makijarvi M, Nenonen J, Oikarinen L, Simeliu K, Toivonen L and Katil T 2001 Magnetocardiographic and electrocardiographic exercise mapping in healthy subjects *Ann Biomed Eng.* **29** 501-9

Umetani K, Okamoto Y, Mashima S, Ono K, Hosaka H and He B 1998 Body surface Laplacian mapping in patients with left or right ventricular bundle branch block *Pacing Clin Electrophysiol.* **21** 2043-54

Wei D 2001 Laplacian electrocardiograms simulated using reslistically shaped heart-torso model during normal and abnormal ventricular depolarization *Electromagnetics* 21 593-605

Williams PL and Warwick R 1989 Gray's Anatomy *Churchill Livingstone Edinburgh* 37th ed. 1598.

Wyndham CR, Meeran MK, Smith T, Saxena A, Engelman RM, Levitsky S and Rosen KM 1979 Epicardial activation of the intact human heart without conduction defect *Circulation* **59** 161-8

Wu D, Ono K, Hosaka H and He B 2000 Simulation of body surface Laplacian maps during ventricular pacing in a 3D inhomogeneous heart-torso model *Methods Inf Med.* **39** 196-9.

Wu D, Schablowski M, Hosaka H and He B 1998 A simulation study of Laplacian ECG in a realistically shaped torso volume conductor: Myocardial infarction *Bioelectrochem Bioenerget.* **47** 231-5

Wu D, Tsai H and He B 1999 On the estimation of the Laplacian electrocardiogram during ventricular activation *Annals of BME* **27** 731-45